

# NLO PREDICTIONS FOR NEW PHYSICS AT THE LHC

Dorival Gonçalves Netto

Dissertation  
Fakultät für Physik und Astronomie  
Universität Heidelberg  
2012



Inaugural-Dissertation zur  
Erlangung der Doktorwürde der  
Naturwissenschaftlich-Mathematischen Gesamtfakultät der  
Ruprecht-Karls-Universität Heidelberg

vorgelegt von  
Master-Phys. Dorival Gonçalves Netto  
aus Cuiabá

Tag der mündlichen Prüfung: 07.01.2013



# NLO PREDICTIONS FOR NEW PHYSICS AT THE LHC

Gutachter: Prof. Dr. Tilman Plehn  
Prof. Dr. Jan Martin Pawłowski



## NLO Vorhersagen für neue Physik am LHC

Die Suche nach neuer Physik ist eine der Hauptziele des CERN Large Hadron Collider. In den meisten Fällen beinhaltet dies die Untersuchung von im Vergleich zum Hintergrund kleinen Signalen. Daher sind theoretisch präzise Vorhersagen von Collider-Observablen essentiell für die Analyse jeder möglichen Signatur neuer Physik. Eine maßgebliche Verbesserung dieses Vorhabens kann durch die Berechnung der NLO QCD Korrekturen für den betrachteten Prozess erreicht werden. Daher liegt der Fokus dieser Arbeit auf dem quantitativen und qualitativen Einfluss der NLO Effekte auf einige wichtige Signaturen neuer Physik. Dafür haben wir das neue, vollautomatische MadGolem package verwendet, zu dem diese Arbeit entscheidende Beiträge geleistet hat. Folgende wichtige LHC Prozesse werden hiermit untersucht: i) skalare Farboktett Paarproduktion; ii) assoziierte Squark-Neutralino-Produktion; und iii) die Paarproduktion von Squarks und Gluinos. In jedem dieser Fälle beobachten wir wichtige QCD Effekte, die zu beträchtlichen Quantenkorrekturen führen ( $K \sim 1.3 - 2$ ), sowie stark unterdrückte theoretische Unsicherheiten, die von  $\mathcal{O}(100\%)$  in erster Ordnung auf  $\mathcal{O}(30\%)$  in NLO absinken. Darüberhinaus erhalten wir eine sehr gute Übereinstimmung der NLO Verteilungen mit denen aus Multi-Jet Merging. Zuletzt haben wir eine umfangreiche Studie über die Auswirkungen typischer vereinfachender Annahmen in der Literatur und gängigen Tools, zum Beispiel der Squarkmassendegeneration, durchgeführt.

## NLO Predictions for New Physics at the LHC

New physics searches are one of the main aims of the CERN Large Hadron Collider. In most cases this entails the study of small expected signals versus huge backgrounds. Therefore, theoretically precise predictions for collider observables are crucial for the analysis of any possible new physics signature. A major improvement in this enterprise can be achieved through the calculation of the Next-to-leading order (NLO) QCD corrections for the process under scrutiny. Thus, in this thesis we focus on the quantitative and qualitative impact of the NLO effects on some important new physics signatures. To do so we have resorted to the new, fully automatized package MADGOLEM, to which this thesis has made major contributions. The following important LHC search channels are examined herewith: *i*) scalar color-octet pair production; *ii*) associated squark-neutralino production; and *iii*) the pair production of squarks and gluinos. In all these cases we observe important QCD effects which lead to sizable quantum corrections ( $K \sim 1.3 - 2$ ) and strongly suppressed theoretical uncertainties, which deplete from  $\mathcal{O}(100\%)$  at leading-order down to  $\mathcal{O}(30\%)$  at NLO. Moreover, we have shown the NLO distributions to be in good agreement with those obtained via multi-jet merging. Finally, we have carried out a comprehensive study on the implications of the usual simplifying assumptions taken in the literature and in current tools, e.g. squark mass degeneracy.



# Acknowledgements

First of all, I would like to thank my supervisor Tilman Plehn for his support and encouragement. In Heidelberg he created an amazing environment for doing physics, establishing a very motivated Pheno group and attracting the best physicists in the field.

During my PhD productive collaborations with great researchers were established, namely Christoph Englert, David Lopez-Val, Kentarou Mawatari, Michael Spannowsky and Ioan Wigmore. With them I had numerous discussions, Skype conferences, productive coffee breaks, and overall a great time. They taught me a lot about physics.

I am especially thankful to David for without him the MADGOLEM project would not have succeeded and poles would still be flying around. Our constant discussions encouraged me and led to great results, and his meticulous proof-reading of my thesis was invaluable.

In the Theoretical Physics Institute of Heidelberg I have met, worked and had a lot of fun with wonderful people. Thank you all!



# Contents

<b>1</b>	<b>Introduction</b>	<b>1</b>
<b>2</b>	<b>Foundations</b>	<b>5</b>
2.1	Quantum Chromodynamics . . . . .	5
2.2	Hard scattering formalism and QCD factorization theorem . . . . .	9
2.3	General structure of fixed order Perturbative QCD . . . . .	11
2.4	Catani-Seymour dipole subtraction . . . . .	13
2.5	On Shell Subtraction Method . . . . .	15
2.6	Scale dependence . . . . .	19
2.7	MADGOLEM: Automizing NLO predictions for new physics . . . . .	20
2.8	Numerical tests . . . . .	22
<b>3</b>	<b>Sgluon pair production</b>	<b>25</b>
3.1	Theoretical setup . . . . .	25
3.2	Production rates at NLO . . . . .	27
3.3	Scale dependence . . . . .	28
3.4	Real and virtual corrections . . . . .	29
3.5	Distributions: fixed order versus multi-jet merging . . . . .	32
3.6	Status of the current searches . . . . .	34
<b>4</b>	<b>SUSY monojet signatures</b>	<b>37</b>
4.1	Leading order production . . . . .	37
4.2	Real and virtual corrections . . . . .	39
4.3	Scale dependence . . . . .	42
4.4	MSSM parameter space . . . . .	44
4.5	Distributions: fixed order versus multi-jet merging . . . . .	45
4.6	Squark-gaugino channels . . . . .	46
<b>5</b>	<b>Squark and gluino pair production to Next-to-Leading Order</b>	<b>47</b>
5.1	Rates . . . . .	48

5.1.1	Parameter space . . . . .	49
5.1.2	Squark pair production . . . . .	51
5.1.3	Squark–gluino production . . . . .	56
5.1.4	Gluino pair production . . . . .	57
5.2	Distributions . . . . .	59
5.2.1	Fixed order versus multi-jet merging . . . . .	59
5.2.2	Scale uncertainties . . . . .	61
5.3	Degenerate versus non-degenerate squarks . . . . .	63
5.3.1	Rates . . . . .	63
5.3.2	Distributions . . . . .	64
<b>6</b>	<b>Conclusions</b>	<b>67</b>
<b>A</b>	<b>Catani-Seymour SUSY and sgluon dipoles</b>	<b>71</b>
A.1	General aspects . . . . .	71
A.2	Final-final dipoles . . . . .	73
A.3	Final-initial dipoles . . . . .	75
<b>B</b>	<b>Renormalization</b>	<b>77</b>
B.1	Sgluons . . . . .	77
B.2	Supersymmetric QCD . . . . .	79
	<b>Bibliography</b>	<b>83</b>

# Chapter 1

## Introduction

On the 4th July 2012 the two main experiments of the Large Hadron Collider (LHC) at CERN reported independently the discovery of a new particle with mass  $\sim 125$  GeV, whose properties strikingly hint at Standard Model (SM) Higgs boson. If this particle is finally confirmed to be the SM Higgs, this would entail another major add-on to the history of success of this paradigm, which passed through the discovery of neutral currents in the 70's decade, the direct production of  $W^\pm$  and  $Z$  bosons in the 80's and the observation of top quarks in the 90's. Now an intense scrutiny aiming at the measure of the spin and couplings of this particle is being performed. So far all these analyses advocate for a SM interpretation.

In spite of its history of success the SM is not a complete theory, since it describes only three of the four fundamental forces, namely the electromagnetic, the weak, and the strong force. Therefore it lacks the inclusion of the gravitational force. Beyond this, further unsettled puzzles such as the experimental evidence for dark matter, dark energy and neutrino oscillation (implying that their mass is non-zero) also motivate further extensions of this model. Most of the new physics models entertain expansions of the SM structures which are correlated to the electroweak scale. This means that the LHC might well be sensitive to them, either by identifying small deviations from the SM parameters or by producing and detecting some new heavy states predicted by these extensions.

The bottom line is that, for LHC searches, precise theoretical calculations are crucial in order to have predictions for the signal and background events within the same accuracy as the experimental results. However, the state-of-the-art of quantum field theory calculations evinces the large gap in difficulty between the Leading Order (LO) and Next to Leading Order (NLO) calculations in the QCD perturbation series. For LO we are provided with a great set of fully automatized tools which allows the automated analysis of collider signatures for processes with up to 8-10 partons in the final state. On the other hand, despite the already well-established theoretical basis for the NLO corrections, no such automatized tools are yet available to perform equivalent analyses. The reason for this discrepancy in the degree of development is the growth in complexity for the NLO case, which stems from the increase in the number of terms to be computed, many subtle issues related to numerical accuracy and stability, and most significantly the presence of divergences of different nature, which require

a dedicated implementation of the renormalization and subtraction procedures. In spite of such difficulties there is no doubt that the upgrade of the automated tools to NLO should be achieved, because for most of the relevant processes these NLO corrections are of critical importance to provide an accurate theoretical prediction. Among the improvements that the NLO predictions represent we should highlight:

- A smaller sensitivity with respect to the unphysical renormalization and factorization scales.
- An accurate calculation of the normalization of the distributions.
- A more accurate description of the shape of distributions.
- A consistent account for the leading QCD quantum effects, *e.g.* interchange of virtual gluons and jet radiation.

In view of this scenario a tool which bridges this gap between LO and NLO turn out to be fundamental. The MADGOLEM tool is intended to give a major contribution on these lines. It is a fully automatized tool which performs NLO QCD studies for generic  $2 \rightarrow 2$  processes in the SM and beyond. Its main target concerns new physics signals, providing their rates and distributions at NLO level. The tool is build upon a fully flexible framework, so that it can be applied to generic new physics scenarios.

The subject of this thesis is the study of trademark new physics signatures for relevant LHC discovery channels at NLO QCD. These calculations have been carried out in the MADGOLEM framework, to which the work presented herewith has made instrumental contributions.

We open the thesis in chapter 2, in which we concisely summarize the main aspects concerning the structure of a generic fixed order Perturbative QCD calculation. We present the general structure of the Catani-Seymour dipole subtraction to deal with infrared divergences, which we further extend in the appendix A. We carefully describe the theoretically well-defined method to address the double-counting arising from on shell heavy particle production, namely the On Shell Subtraction method. Finally, we close this chapter by describing the MADGOLEM program, in whose development this thesis has substantially contributed, and show some of the numerical tests by which we have proved the stability of the tool and its robust performance.

In chapter 3 we turn our attention into the application of our tool to Beyond Standard Model (BSM) LHC phenomenology. We first perform a complete NLO calculation for the production of a color-octet scalar pair at the LHC. We analyze the qualitative features and quantitative impact of the QCD quantum effects in terms of rates and distributions. The LHC current search status is also presented.

Chapter 4 describes a supersymmetric process, namely squark–neutralino production  $pp \rightarrow \tilde{q}\tilde{\chi}_1^0$ , which can lead to the trademark phenomenological signature of one hard jet

---

with missing energy. For this process *i*) we present the structure of the NLO corrections; *ii*) perform a scan in the Minimal Supersymmetric Standard Model (MSSM) parameter space; *iii*) Analyze several distributions at NLO level.

In Chapter 5 we perform a comprehensive study of the main discovery channels for supersymmetry at the LHC, these are the pair-wise and associated production of the strongly-interacting SUSY particles  $pp \rightarrow \tilde{q}\tilde{q}; \tilde{q}\tilde{q}^*; \tilde{q}\tilde{g}; \tilde{g}\tilde{g}$ . Even if these processes have already been analyzed in the literature, the MADGOLEM framework presents significant improvements, such as not requiring any assumptions on the supersymmetric mass spectra and allowing a systematic study at the distribution level. Therefore we make use of these improved features to undertake a comprehensive exam of the structure of the NLO corrections by means of *i*) a scan in the MSSM parameter space, identifying the trends that are common to these different channels; *ii*) a comprehensive comparison between fixed order distributions and jet merged ones; *iii*) Lastly, the numerical implications, both for total rates and distributions, of the usual simplifying assumptions mentioned above, e.g. squark mass degeneracy.

Final conclusions are drawn in Chapter 6.

An exhaustive analytical account of the Catani-Seymour dipoles required for SUSY-QCD calculations is presented in Appendix A. These are provided for the first time in the literature with the FKS-like phase-space restriction  $\alpha$ , which we support in MADGOLEM. The details concerning the renormalization procedure implemented in MADGOLEM are documented in Appendix B. There we provide the relevant expressions for the renormalization of the scalar color-octet model (which is relevant for Chapter 3) and for the supersymmetric QCD searches of the MSSM (which is applicable in Chapters 4 and Chapter 5).



# Chapter 2

## Foundations

### 2.1 Quantum Chromodynamics

Quantum Chromodynamics (QCD) is the theory which describes one of the four fundamental forces in nature, namely the strong nuclear force. It is a Yang-Mills gauge theory based on an unbroken  $SU(3)$  symmetry. It has been very well tested in numerous experiments mainly over the second half of the twentieth century in collider experiments. At the Large Hadron Collider (LHC) it will play a fundamental role in the analysis of its results. In particular, in some searches with overwhelming backgrounds, precise QCD predictions become crucial to distinguish possible new physics signatures from a mere SM dynamics.

#### The QCD Lagrangian

The QCD Lagrangian  $\mathcal{L}_{\text{QCD}}$  can be divided into three parts: the classical density  $\mathcal{L}_{\text{classical}}$ , the gauge fixing term  $\mathcal{L}_{\text{gauge-fixing}}$  and the ghost contribution  $\mathcal{L}_{\text{ghost}}$

$$\mathcal{L}_{\text{QCD}} = \mathcal{L}_{\text{classical}} + \mathcal{L}_{\text{gauge-fixing}} + \mathcal{L}_{\text{ghost}}. \quad (2.1)$$

Following Ref. [1], the classical Lagrangian describes a non-abelian gauge theory coupled to fermionic matter

$$\mathcal{L}_{\text{classical}} = \sum_{\text{flavor}} \bar{q}_a (i\not{D}_{ab} - m_{q_a} \delta_{ab}) q_b - \frac{1}{4} F_{\mu\nu}^A F_A^{\mu\nu}, \quad (2.2)$$

where the fermionic field  $q_a$  represents the quark field summed in flavor,  $q_a \in (u, d, c, s, t, b)$ , and  $m_{q_a}$  denotes the respective mass. We follow the particle physics metric convention  $g^{\alpha\beta} = \text{diag}(1, -1, -1, -1)$  and work with natural units  $\hbar = c = 1$ . The Dirac gamma matrices satisfy the anticommutation relations

$$\{\gamma^\mu, \gamma^\nu\} = 2g^{\mu\nu}. \quad (2.3)$$

$F_{\mu\nu}^A$  is the field strength tensor for the gluonic field<sup>1</sup>  $A_\mu^A$  and is given by

$$F_{\mu\nu}^A = \partial_\mu A_\nu^A - \partial_\nu A_\mu^A - g_s f^{ABC} A_\mu^B A_\nu^C. \quad (2.4)$$

Here  $g_s$  is the QCD coupling strength and  $f^{ABC}$  stands for the structure constant of the  $SU(3)$  gauge group. The indices in the triplet representation are denoted by lower case Latin letters ( $a=1,2,3$ ) and in the adjoint representation by capital Latin letters ( $A=1,\dots,8$ ). The covariant derivative  $D$  in the fundamental representation reads

$$D_{ab}^\mu = \partial^\mu \delta_{ab} + i g_s A^\mu{}^C t_{ab}^C \quad (2.5)$$

and in the adjoint

$$D_{AB}^\mu = \partial^\mu \delta_{AB} + i g_s A^\mu{}^C T_{AB}^C, \quad (2.6)$$

where  $t_{ab}^A$  ( $T_{ab}^A$ ) are the generators in the fundamental (adjoint) representations of the gauge group.

The gauge fixing term  $\mathcal{L}_{\text{gauge-fixing}}$  is added to the Lagrangian density in order to be able to define the gluonic propagator. A particular class named as covariant gauge reads

$$\mathcal{L}_{\text{gauge-fixing}} = -\frac{1}{2\lambda} (\partial^\mu A_\mu^A)^2, \quad (2.7)$$

where  $\lambda$  is an arbitrary parameter. The most popular choices for this parameter are  $\lambda = 1$  (Feynman gauge) and  $\lambda \rightarrow 0$  (Landau gauge).

The last term, which is the ghost contribution

$$\mathcal{L}_{\text{ghost}} = (\partial^\mu \eta^A)^\dagger (D_{AB}^\mu \eta^B), \quad (2.8)$$

is required for non-abelian gauge theories to cancel unphysical longitudinal degrees of freedom of the gluonic field which should not propagate. The extra field  $\eta^A$  is a complex scalar, but satisfies the Fermi statistics.

Another popular class of gauge fixing terms are the physical gauges

$$\mathcal{L}_{\text{gauge-fixing}} = -\frac{1}{2\lambda} (n^\mu A_\mu^A)^2; \quad (2.9)$$

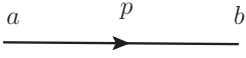
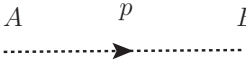
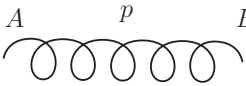
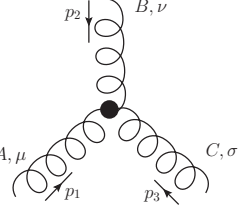
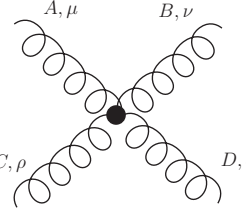
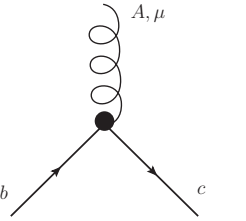
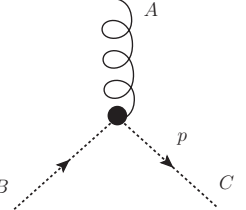
here  $n^\mu$  is an arbitrary four-vector. Within this class of gauges only the two physical polarizations propagate, and no ghost term is required. However, it leads to a more complicated gluon propagator. Therefore in most of the calculations, in particular beyond the LO, it is preferable to use Eq. 2.7 which will lead to a simpler structure.

Thereafter we will be interested in calculating cross sections and perform perturbation theory. To that aim we shall translate the QCD Lagrangian into Feynman rules as shown in Table 2.1.

---

<sup>1</sup>Throughout this thesis we use the conventional label  $A_\mu^A$  for the gluon field, which allows for a better distinction with the sgluon field  $G$  introduced in Chapter 3. However, when discussing about MSSM processes, in particular when describing their SUSY-QCD counter terms in Sec. B.2, we resort to the traditional conventions in the old MSSM literature, where the gluon field is denoted by  $G$ .

---

	$\delta_{ab} \frac{i}{\not{p} - m + i\epsilon}$
	$\delta^{AB} \frac{i}{p^2 + i\epsilon}$
	$\delta^{AB} \frac{i}{p^2 + i\epsilon} \left( -g^{\mu\nu} + (1 - \lambda) \frac{p^\mu p^\nu}{p^2 + i\epsilon} \right)$
	$g_s f^{ABC} [g^{\mu\nu} (p_1 - p_2)^\sigma + g^{\nu\sigma} (p_2 - p_3)^\mu + g^{\mu\sigma} (p_3 - p_1)^\nu]$
	$-i g_s^2 [f^{ABE} f^{CDE} (g^{\mu\rho} g^{\nu\sigma} - g^{\mu\sigma} g^{\nu\rho}) \\ + f^{ACE} f^{BDE} (g^{\mu\nu} g^{\rho\sigma} - g^{\mu\sigma} g^{\nu\rho}) \\ + f^{ADE} f^{BCE} (g^{\mu\nu} g^{\rho\sigma} - g^{\mu\rho} g^{\nu\sigma})]$
	$i g_s t_{cb}^A \gamma^\mu$
	$-g_s f^{ABC} p^\mu$

---

Table 2.1: QCD Feynman rules in the covariant gauge. Fermions are denoted as straight lines, gluons as curly and ghost as dashed.

## Running Coupling Constant and Asymptotic Freedom

When performing a calculation of an observable as a perturbation series in the coupling  $\alpha_s = g_s^2/4\pi$  it is necessary to introduce an unphysical mass scale  $\mu_R$ . This new mass scale results from the renormalization procedure entitled to remove the ultraviolet (UV) divergences. As an example, consider that we have a dimensionless observable  $R$  which is a function of only one physical scale  $Q^2$ . Thus, after renormalization  $R$  will depend on  $Q^2$ ,  $\mu_R^2$ ,  $\alpha_s(\mu_R^2)$ . Moreover, dimension analysis dictates the general form  $R = R(Q^2/\mu_R^2, \alpha_s)$ . Since the dependence on the parameter  $\mu_R$  is unphysical, the following relation must hold

$$\mu_R^2 \frac{d}{d\mu_R^2} R(Q^2/\mu_R^2, \alpha_s) = \left( \mu_R^2 \frac{\partial}{\partial \mu_R^2} + \mu_R^2 \frac{\partial \alpha_s}{\partial \mu_R^2} \frac{\partial}{\partial \alpha_s} \right) R(Q^2/\mu_R^2, \alpha_s) = 0 \quad (2.10)$$

Here the coefficient of the second term is the so-called  $\beta$ -function

$$\beta(\alpha_s) \equiv \mu_R^2 \frac{\partial \alpha_s}{\partial \mu_R^2}, \quad (2.11)$$

which implicitly means that the coupling constant is scale dependent. Using perturbation theory for sufficiently large  $Q$ , *i.e.* in the asymptotic regime where the confinement effects are not influencing, the  $\beta$ -function reads

$$\beta(\alpha_s) = -\alpha_s^2(\beta_0 + \beta_1 \alpha_s + \mathcal{O}(\alpha_s^2)) \quad (2.12)$$

with

$$\beta_0 = \frac{33 - 2n_f}{12\pi}, \quad \beta_1 = \frac{153 - 19n_f}{2\pi(33 - 2n_f)}, \quad (2.13)$$

where  $n_f$  is the number of quark flavors with masses lower than the energy scale  $\mu_R$ . From Eqs. 2.11, 2.12 and if we neglect all terms higher than  $\beta_0$  in the  $\beta$ -function expansion we can establish the following relation between  $\alpha_s(Q^2)$  and  $\alpha_s(\mu_R^2)$

$$\alpha_s(Q^2) = \frac{\alpha_s(\mu_R^2)}{1 + \alpha_s(\mu_R^2)\beta_0 \ln(Q^2/\mu_R^2)}. \quad (2.14)$$

Notice, that from Eq. 2.13, and if  $n_f < 33/2$ , the coupling  $\alpha_s(Q^2)$  decreases for a growing  $Q$ . This fact is known as *asymptotic freedom* [2, 3]. In this case the coupling is small, therefore it is safe to use perturbation theory.

On the other hand, for small momentum transfer the coupling value  $\alpha_s(Q^2)$  increases. This is known as *confinement* and is the reason why it is not possible to see free quarks and gluons in Nature. The scale at which Eq.2.14 diverges is called the Landau pole  $Q = \Lambda_{QCD}$

$$\Lambda_{QCD}^2 = \mu_R^2 \exp \left[ \frac{-12\pi}{(33 - 2n_f)\alpha_s(\mu_R^2)} \right]. \quad (2.15)$$

If we set  $\mu_R$  to the Z boson mass ( $m_Z$ ),  $n_f = 5$  and use the value of  $\alpha_s(m_Z)$  from Eq. 2.15 that  $\Lambda_{QCD} \approx 91$  MeV. More precise estimations of the Landau pole lead to  $\Lambda_{QCD} \approx 200$  MeV. We discuss in the following section the treatment of these two regimes at colliders, namely the asymptotic and confinement regimes.

## 2.2 Hard scattering formalism and QCD factorization theorem

Scattering processes at Hadron colliders in general involve both hard and soft scales. However, in each regime the underlying theory which describes these processes, the Quantum Chromodynamics, has different power of predictability. In the high energy limit, in which the momentum transfer is high, the running coupling constant  $\alpha_s(Q^2)$  becomes small, as presented in the last section. Therefore, we can perform a perturbative expansion in the coupling constant. However, in the low energy regime  $\alpha_s(Q^2)$  increases and QCD becomes non-perturbative, thus the QCD effects are less well understood in this region and one has to rely on data and/or simulations of the corresponding non-perturbative behavior.

As in Hadron Colliders the soft and hard processes take place together, it is important to be able to factorize these two regimes in such a way that one can apply the perturbation theory in the hard regime, while in the low energy regime one is forced to make use of experimental inputs to overcome our ignorance.

The separation in these two regimes is formalized by the *factorization theorem* [4]. First formulated for deep inelastic lepton-hadron scattering (DIS), it permits to write the cross section as a convolution of the perturbative partonic cross section  $\hat{\sigma}_i$ , with the non-perturbative but process independent (*i.e.* universal) object, so called parton distribution function (pdf) which determines the dynamics of the QCD partons inside the colliding hadrons

$$\sigma = \sum_i \int_0^1 dx_i f_{i/h}(x_i, \mu_F^2) \sum_{n=0}^{\infty} \alpha_s^n \hat{\sigma}_i^{(n)}(x_i, \alpha_s(\mu_R^2), \frac{Q^2}{\mu_F^2}, \frac{Q^2}{\mu_R^2}). \quad (2.16)$$

We can interpret the pdfs as probability distributions for the momentum of the parton constituents of the colliding hadrons. The total hadron momentum  $P_h^\mu$  is shared among the partons. The parton  $i$  carries the momentum  $p_i^\mu = x_i P_h^\mu$  with probability  $f_{i/h}(x_i, \mu_F^2)$ .

For a hadron-hadron collision the hadronic cross section can be written as<sup>2</sup>

$$\sigma_{h_1 h_2 \rightarrow f} = \sum_{i,j} \int dx_i dx_j f_{i/h_1}(x_i, \mu_F^2) f_{j/h_2}(x_j, \mu_F^2) \sum_{n=0}^{\infty} \alpha_s^n \hat{\sigma}_{ij}^{(n)}(x_i, x_j, \alpha_s(\mu_R^2), \frac{Q^2}{\mu_F^2}, \frac{Q^2}{\mu_R^2}). \quad (2.17)$$

Two facts should be highlighted:

- The partonic cross section is calculable in perturbation theory as a power series in  $\alpha_s$  and does not depend on the nucleon dynamics, only on its parton  $i$  and  $j$ .
- The pdfs are non-perturbative quantities and are obtained from fits to data. They constitute a parametrization of the momentum distributions of partons within a given nucleon.

---

<sup>2</sup>Factorization was just proven for inclusive cross sections in DIS and in Drell-Yan. The proof for the general hadron-hadron collisions is still missing in the literature and the factorization hypothesis is taken as an ansatz.

These two pictures are separated by the factorization scale ( $\mu_F$ ) representing the point of changing between the soft and hard QCD regimes. Roughly speaking, all the information from the emissions of the initial state parton below the energy scale  $\mu_F$  is included inside the pdfs and above this scale in the partonic cross section, as graphically represented in Fig. 2.1. If one included all orders in perturbation theory the final result would be independent of this unphysical scale. But in fixed order it will be dependent. Therefore, different choices in this scale yield different results on the cross section. This theoretical uncertainty reflects the influence of the missing higher order terms. In order to avoid unnaturally large logarithms in the perturbation series, it is common to define  $\mu_F$  within the same order of the typical momentum scale of the process.

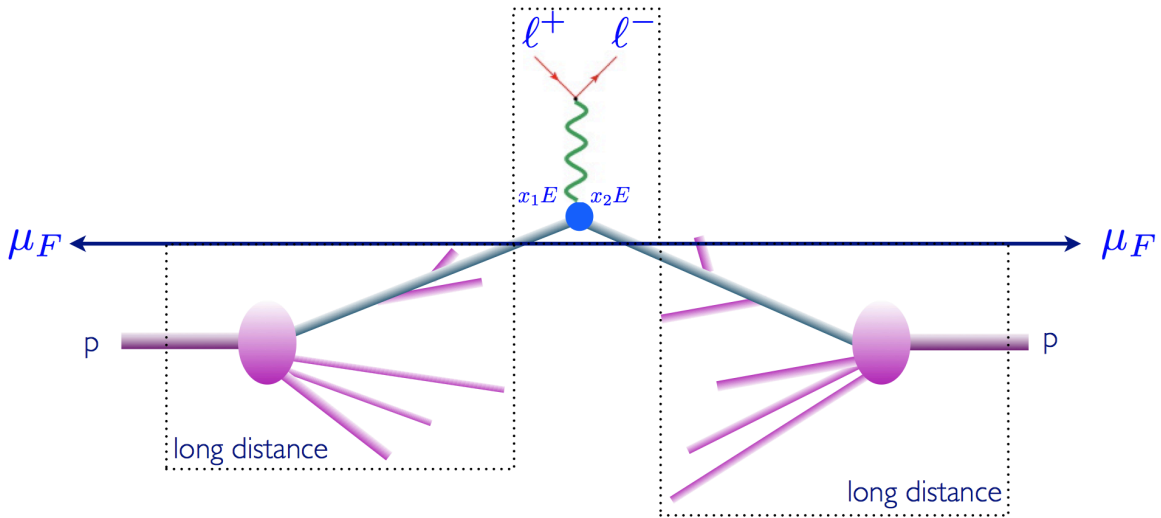


Figure 2.1: Pictorial representation of the factorization of the soft and hard regimes for the Drell-Yan process.

Although the pdfs are non-calculable from first principles, there are perturbative differential equations which describe their evolution with  $\mu_F$ . They are obtained by requiring that the cross section is independent of the choice of the scale  $\mu_F$  at a given order and they are known as DGLAP<sup>3</sup> evolution equations [5]

$$\begin{aligned} \frac{\partial q_i(x, \mu_F^2)}{\partial \log \mu_F^2} &= \frac{\alpha_s}{2\pi} \int_x^1 \frac{dz}{z} [P_{q_i q_j}(z, \alpha_s) q_j(x/z, \mu_F^2) + P_{q_i g}(z, \alpha_s) g(x/z, \mu_F^2)] \\ \frac{\partial g(x, \mu_F^2)}{\partial \log \mu_F^2} &= \frac{\alpha_s}{2\pi} \int_x^1 \frac{dz}{z} [P_{g q_j}(z, \alpha_s) q_j(x/z, \mu_F^2) + P_{g g}(z, \alpha_s) g(x/z, \mu_F^2)], \end{aligned} \quad (2.18)$$

where  $g(x, \mu_F)$  and  $q_i(x, \mu_F)$  denote respectively the gluon and the quark of flavor  $i$  pdfs.  $P_{ab}(z)$  is the so-called splitting function, which represents the probability that a parton of type  $b$  radiates a quark or gluon and becomes a parton of type  $a$  carrying a fraction of the

<sup>3</sup>DGLAP stands for Dokshitzer, Gribov, Lipatov, Altarelli and Parisi.

momentum  $z$  of the parton  $b$ . These can be expanded in perturbation theory as

$$P_{ab}(z, \alpha_s) = \sum_{n=0}^{\infty} \left( \frac{\alpha_s}{2\pi} \right)^n P_{ab}^{(n)}(z). \quad (2.19)$$

Therefore, if one aims to work a fixed-order prediction up to the term  $\hat{\sigma}_{ij}^{(n)}$  in Eq. 2.17 it is necessary to include in Eqs. 2.18 and 2.19 up to the terms  $P_{ab}^{(n)}$  to be consistent. The explicit form of these splitting functions are presented at Leading Order and Next to Leading Order in Ref. [1].

## 2.3 General structure of fixed order Perturbative QCD

For hadron colliders a straightforward systematic improvement in the theoretical predictions arises from the calculation of one further term in the perturbative expansion in  $\alpha_s$  of Eq. 2.17. At the LHC energy scale,  $\alpha_s \sim 0.1$ , therefore one would naively expect that the theoretical predictions at Leading Order (LO) are correct within an uncertainty of 10%. However, in some processes this is in practice not the case and we can actually get large corrections when performing the calculation at the Next to Leading Order (NLO). Indeed, as we will see in the processes presented in the following chapters of this thesis, it is quite common to obtain NLO corrections to the LO prediction of approximately 50 – 100%. Therefore it is a fundamental task to understand the structure of the fixed order calculations and provide results including high order terms, thus reducing the theoretical uncertainties.

### Leading Order calculations

The simplest predictions arise from the calculation of the observables at the lowest order in the perturbation expansion. In this case, let us suppose that we have  $m$  final-state partons. In this case the LO QCD cross section is given by

$$\sigma^{LO} = \sum_{i,j} \int d\Phi_m dx_i dx_j f_{i/h_1}(x_i, \mu_F^2) f_{j/h_2}(x_j, \mu_F^2) |\mathcal{M}_m^{(tree)}(\{p_l\})|^2 F_J^{(m)}(\{p_l\}), \quad (2.20)$$

where  $d\Phi_m$  is the total phase-space for an  $m$ -particle final state ( $p_l = p_1, \dots, p_m$ ),  $\mathcal{M}_m^{(tree)}(\{p_l\})$  is the tree-level matrix element which depends on the given process and  $F_J^{(m)}(\{p_l\})$  is the phase-space function that defines the physical quantity we want to compute, including the experimental cuts to be applied. In order to obtain fully differential distributions, the integration over the phase-space needs to be carried out numerically. For the LO we are provided with a great set of fully automatized tools to perform this task which allows us to consider up to  $m = 8 - 10$  partons in the final state [6–9].

### Next to Leading Order corrections

The next term in this expansion requires the consideration of extra contributions that arise from real and virtual (one-loop) contributions. The possible types of real emission diagrams

are generically sketched in Fig. 2.2. These have the same structure as the Born level diagrams, but with one extra parton radiated,  $\mathcal{M}_m^{(tree)} \rightarrow \mathcal{M}_{m+1}^{(tree)}$ .

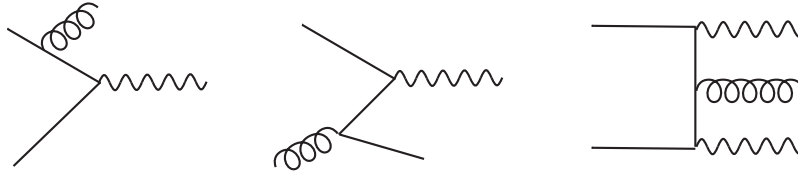


Figure 2.2: Sample of the real emission diagrams for the process  $pp \rightarrow V$  or  $pp \rightarrow VV$ , where  $V$  represents a gauge boson. From the left to the right we present *i*) the gluon emission from an external quark leg; *ii*) excited initial state arising from the splitting  $g \rightarrow q\bar{q}$ ; and *iii*) gluon emission from an internal quark leg.

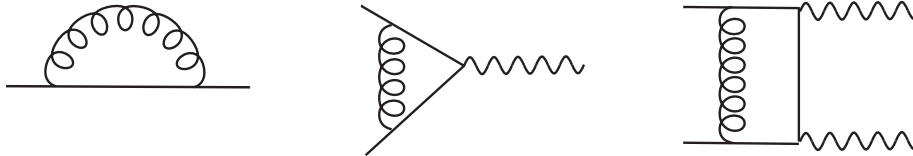


Figure 2.3: Sample of the virtual correction Feynman diagrams. From the left to the right we present graphs with *i*) two external legs (propagator correction); *ii*) three external legs (vertex correction); and *iii*) four external legs (box diagrams).

The other set of contributing diagrams are the one-loop graphs. These are diagrams with the same number of partons in the final state as the Born diagrams. They account for the internal exchange of virtual particles, e.g. gluons, and are expressed in terms of the one-loop integrals,  $\mathcal{M}_m^{(tree)} \rightarrow \mathcal{M}_m^{(1-loop)}$ . Its contribution to the cross section arises from the interference with the LO matrix elements. The matrix element squared of the one-loop diagrams, however, is already a NNLO contribution to the cross section and should not be included in the NLO calculation. A generic sample of Feynman diagrams for the virtual corrections is depicted in Fig. 2.3.

Beyond the one-loop and real emission corrections one also needs to add an extra term known as the collinear subtraction term. This term is responsible for the subtraction of the left-over singularities from collinear splittings off the initial state emitter that should be absorbed into the parton distribution function. Since these collinear divergencies correlated with the pdfs are unique and process independent, the parton distribution functions are process independent also at NLO. In fact, the *factorization theorem* states that this holds at every order in perturbation theory.

Therefore, we can present the NLO corrections as a sum of real emission corrections, collinear subtraction terms and virtual corrections terms as shown in Fig. 2.4. Here we sketch some peculiarities concerning this sum and each of these terms. The virtual corrections present ultraviolet (UV) singularities, which are removed by renormalization giving UV finite results. The renormalization procedure involves the introduction of corresponding counter-

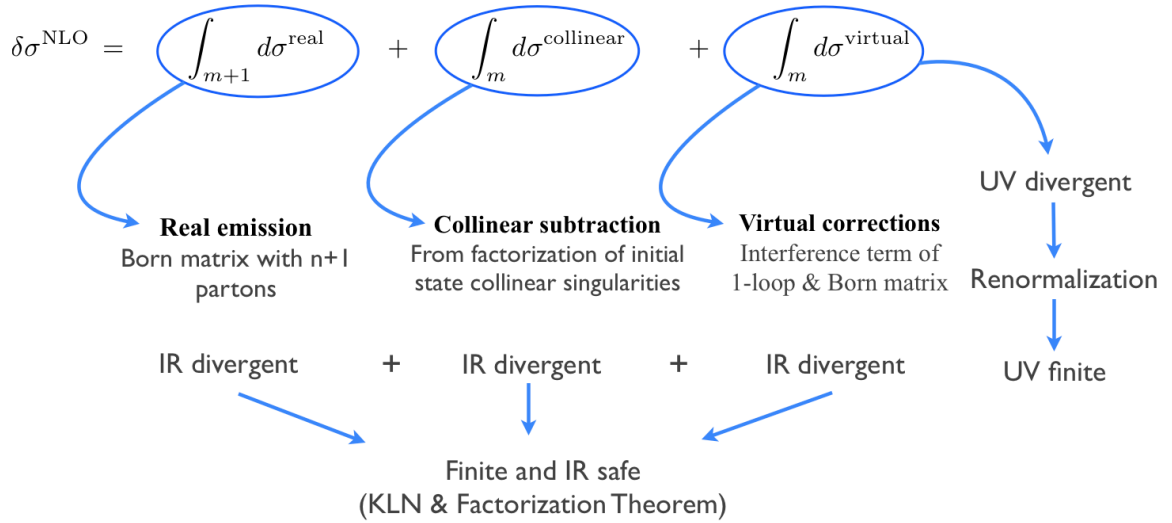


Figure 2.4: Structure of the NLO QCD corrections.

terms for the strong coupling constant and the masses, which are fixed for each particular model from a set of conditions defining our renormalization scheme (for more details see Appendix B). On the other hand, each of these terms presents Infrared (IR) divergencies and just after their sum is performed a finite and IR-safe quantity is obtained. The fact that the sum is finite is ensured by the theorems of Bloch and Nordsieck [10] and Kinoshita, Lee and Nauenberg [11, 12]. These theorems guarantee that this cancellation of the IR divergencies holds to all orders in perturbation theory and for any number of final state particles.

In the next section we will elaborate on the structure of the NLO corrections depicted in the Fig. 2.4. In the results to be presented we will put special emphasis on the technical procedures to perform the sum of each contribution without spoiling the cancellation of the IR singularities when using Monte Carlo methods.

## 2.4 Catani-Seymour dipole subtraction

QCD calculations beyond LO are very much involved and analytic treatments are feasible only for simple fully inclusive processes. On the other hand, the implementation of Monte Carlo methods is a non-trivial task given the IR structure that arises from the  $m+1$ -parton and  $m$ -parton phase-space integrals, see Fig. 2.4. Therefore these have to be numerically integrated separately and require a special method to treat their poles. Otherwise the numerical convergency would be spoilt.

As presented in Fig. 2.4, the NLO corrections to the cross section consist in a sum of the real emission contributions, virtual corrections and collinear subtraction terms, where each of these integrals is IR divergent. For the real emissions, the divergences appear when the extra radiated parton becomes soft or collinear to some other partons leading to on shell propagators in the matrix element. For the virtual corrections, the divergent structures arise from the unrestricted loop momentum integral, implying also that the propagator can go on

shell. And finally the divergent structures of the collinear subtraction terms are meant to subtract the left-over singularities from the parton distribution functions, in such a way that they implement a renormalization prescription for the latter.

Using dimension regularization, with  $d = 4 - 2\epsilon$  space time dimensions, these IR structures will appear either as single poles  $1/\epsilon$  (stemming from either a soft or a collinear singularity) or double poles  $1/\epsilon^2$  (when both types of singularities overlap). The idea of the Catani-Seymour subtraction method [14] is to define a subtraction term,  $d\sigma^A$ , for the real emission which encodes all its possible IR divergencies in the  $m + 1$ -parton phase-space integral and add this term back in the  $m$ -parton one. On this way the NLO corrections are rewritten as

$$\delta\sigma^{\text{NLO}} = \int_{m+1} \left( d\sigma_{\epsilon=0}^{\text{real}} - d\sigma_{\epsilon=0}^A \right) + \int_m \left( d\sigma^{\text{virtual}} + d\sigma^{\text{collinear}} + \int_1 d\sigma^A \right)_{\epsilon=0}. \quad (2.21)$$

The subtraction term  $d\sigma^A$  is constructed so that it satisfies the following requirements [13]:

- It should subtract locally, *i.e.* point by point in phase-space, the divergent structures present in  $d\sigma^{\text{real}}$ . Thus, one can safely calculate the  $m+1$ -parton phase-space integral taking in the limit  $\epsilon \rightarrow 0$

$$\delta\sigma_{m+1}^{\text{NLO}} = \int_{m+1} \left( d\sigma_{\epsilon=0}^{\text{real}} - d\sigma_{\epsilon=0}^A \right). \quad (2.22)$$

- The subtraction term  $d\sigma^A$  should be analytically integrable in  $d = 4 - 2\epsilon$  dimension over the extra single-parton phase-space. This allows us to add back the integrated expression for this term (the so-called integrated dipole) into the  $m$ -particle phase-space,

$$\delta\sigma_m^{\text{NLO}} = \int_m \left( d\sigma^{\text{virtual}} + d\sigma^{\text{collinear}} + \int_1 d\sigma^A \right)_{\epsilon=0}. \quad (2.23)$$

On this manner the phase-space integral to be implemented in the Monte Carlo analysis can be calculated separately in the  $m$  and  $m + 1$ -parton phase-space, and latter on combined

$$\delta\sigma^{\text{NLO}} = \delta\sigma_{m+1}^{\text{NLO}} + \delta\sigma_m^{\text{NLO}}. \quad (2.24)$$

The counter term  $d\sigma^A$  is constructed from the know properties of QCD factorization in the soft and collinear limits where the  $|\mathcal{M}_{m+1}^{(\text{tree})}|^2$  behaves as the born matrix element squared  $d\sigma^B$  convoluted in color and spin with a universal singular factor (named dipole factors)  $dV_{\text{dipole}}$ . Therefore one can write the subtraction terms schematically as

$$d\sigma^A = \sum d\sigma^B \otimes dV_{\text{dipole}}. \quad (2.25)$$

This structure allows a factorizable mapping from the  $m + 1$ -parton phase-space into a  $m$ -parton times a single-parton phase-space kinematics. This mapping permits the analytical integration of  $dV_{\text{dipole}}$  over the single-parton kinematics, so that

$$\int_{m+1} d\sigma^A + \int_m d\sigma^{\text{collinear}} = \int_m [d\sigma^B \otimes \mathbf{I}(\epsilon)] + \int_0^1 dx \int_m [d\sigma^B \otimes (\mathbf{P}(x, \mu_F^2) + \mathbf{K}(x))] , \quad (2.26)$$

where the operator  $\mathbf{I}(\epsilon)$  contains all the singular terms and the operators  $\mathbf{P}$  and  $\mathbf{K}$  contain just finite contributions.

On this manner, for a given real emission matrix element (this is to say, for each specific type of parton radiation, *e.g.* a gluon splitting off a quark external leg  $q \rightarrow qg$ ) one can find the appropriate choice of dipoles and integrated dipoles (operators  $\mathbf{I}$ ,  $\mathbf{K}$  and  $\mathbf{P}$ ) in [14], such that the NLO correction is computed as

$$\delta\sigma^{NLO} = \int_{m+1} [d\sigma^R]_{\epsilon=0} - d\sigma^B \otimes dV_{\text{dipole}}|_{\epsilon=0} + \int_m [d\sigma^{\text{virtual}} + d\sigma^B \otimes \mathbf{I}(\epsilon)]_{\epsilon=0} + \int_0^1 dx \int_m [d\sigma^B \otimes (\mathbf{P}(x, \mu_F^2) + \mathbf{K}(x))]. \quad (2.27)$$

In the appendix A we present the explicit formulas for the dipoles that do not appear in the SM but which are related to the genuine real emission involving SUSY particles. These expressions were lacking so far in the literature in its most general form, including their expanded formulation in terms of the so called phase-space parameter  $\alpha$ . This thesis provides for the first time the corresponding analytical formulae, which we have implemented in our program MADGOLEM in order to extend the reach of the automated NLO calculations. For more details see appendix A.

## 2.5 On Shell Subtraction Method

When performing NLO computations involving heavy particles one should take care to avoid some particular sources of double counting in the corrections which could potentially spoil the performance of the perturbative series. As an example we consider the real emission corrections to squark-neutralino production  $pp \rightarrow \tilde{q}\tilde{\chi}_1^0$  (a process which we analyze at NLO in Chap. 4): the partonic sub-channels with an additional quark in the final state  $qq \rightarrow \tilde{q}q\tilde{\chi}_1^0$  display a peculiar behavior which we illustrate in Fig. 2.5. The diagrams (a) and (b) are part of the genuine NLO corrections to squark-neutralino production. In contrast, the diagram (c) can be interpreted in two ways:

$$\begin{array}{ll} qq \rightarrow \tilde{q}\tilde{q}^{(*)} \rightarrow \tilde{q}q\tilde{\chi}_1^0 & \text{squark-neutralino production} \\ qq \rightarrow \tilde{q}\tilde{q} \rightarrow \tilde{q}q\tilde{\chi}_1^0 & \text{squark pair production plus squark decay} \end{array} \quad (2.28)$$

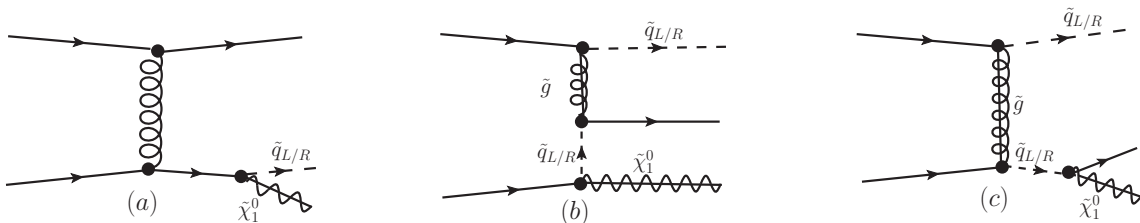


Figure 2.5: Sample diagrams for the real-emission corrections to squark-neutralino production  $pp \rightarrow \tilde{q}\tilde{\chi}_1^0$  with an additional quark in the final state.

The first interpretation simply assumes NLO corrections to the hard process  $pp(qq) \rightarrow \tilde{q}\tilde{\chi}_1^0$  and is generally valid for an intermediate on shell ( $\tilde{q}$ ) and off-shell ( $\tilde{q}^{(*)}$ ) squarks. The second interpretation accounts for the LO process for  $qq \rightarrow \tilde{q}\tilde{q}$  followed by the branching  $\text{BR}(\tilde{q} \rightarrow q\tilde{\chi}_1^0)$  and implicitly assumes an on shell squark. For a mass hierarchy  $m_{\tilde{q}} > m_{\tilde{\chi}_1^0}$  we can therefore separate the two instances into off-shell and on shell squarks. This distinction avoids double counting and is the basis of our on shell subtraction scheme. In the literature, approaches to tackle this problem include

- **a slicing procedure**, which separates the phase-space related to the on shell emissions and removes the on shell divergence by requiring  $|\sqrt{s_{\tilde{q}\tilde{\chi}_1^0}} - m_{\tilde{q}}| > \delta$  [15], where  $\delta$  is an unphysical phase-space cutoff. Phase-space methods of this kind do not offer an overall cancellation of the  $\delta$  dependence and do not act locally in phase-space. Moreover, as a pure phase-space approach, they do not allow for a proper separation into the different finite, on shell and interference contributions, which is crucial for a reliable rate prediction.
- **diagram removal**, where the resonant matrix elements are removed by hand. Even if in certain cases this method might perform properly in the limit  $\Gamma/m \ll 1$  [16], but it ignores any kind of interference contributions, which do not actually need to vanish in this narrow width limit. This scheme suffers from several theoretical drawbacks, in particular it does not preserve gauge invariance and is neither able to retain the spin correlations between the on shell resonance and the final state particles.
- **local on shell subtraction** in the so-called PROSPINO scheme [17, 22] which, under the name ‘diagram subtraction’, is also used in the single-top computation of MC@NLO [16]. This is the method employed in our program MADGOLEM.

To define the on shell subtraction we split the contributions of the real emission matrix element in two parts: the first piece concerns the resonant diagram (c) and is denoted as  $\mathcal{M}_{\text{res}}$ , while the second piece represents the non-resonant diagrams (a) and (b) and is denoted as  $\mathcal{M}_{\text{rem}}$  (where the suffix stands for ”remainder”). Note that this separation is defined at the amplitude level and is not based on the amplitude squared. The full matrix element squared becomes

$$|\mathcal{M}|^2 = |\mathcal{M}_{\text{res}}|^2 + 2\text{Re}(\mathcal{M}_{\text{res}}^* \mathcal{M}_{\text{rem}}) + |\mathcal{M}_{\text{rem}}|^2. \quad (2.29)$$

The divergent propagator within  $\mathcal{M}_{\text{res}}$  we regularize as a Breit-Wigner propagator

$$\frac{1}{p_{ij}^2 - m_{ij}^2} \rightarrow \frac{1}{p_{ij}^2 - m_{ij}^2 + im_{ij}\Gamma_{ij}}, \quad (2.30)$$

where  $m_{ij}$  is the mass of the mother particle, namely the heavy resonance in the splitting  $\tilde{i}\tilde{j} \rightarrow ij$ , as shown in Fig. 2.6.

As explained above, the appearance of a possible double counting is limited to the on shell configuration in  $|\mathcal{M}_{\text{res}}|^2$  and will depend, in practice, on the mass hierarchy between

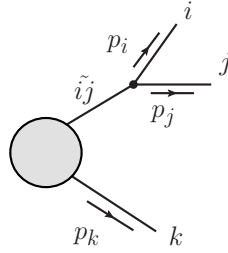


Figure 2.6: Kinematic variables for the on shell subtraction.

the particle  $ij$  and its final-states. To remove it we define a local subtraction term  $d\sigma^{\text{OS}}$  and insert it into the general expression for the real emission NLO amplitude in complete analogy to the Catani-Seymour dipole subtraction Eq.(A.3), such that the total cross section is given by

$$\delta\sigma^{\text{NLO}} = \int_{n+1} \left( d\sigma_{\epsilon=0}^{\text{real}} - d\sigma_{\epsilon=0}^{\text{A}} - d\sigma_{\epsilon=0}^{\text{OS}} \right) + \int_n \left( d\sigma^{\text{virtual}} + d\sigma^{\text{collinear}} + \int_1 d\sigma^{\text{A}} \right)_{\epsilon=0}. \quad (2.31)$$

The extra subtraction term  $d\sigma^{\text{OS}}$  correspond to  $|\mathcal{M}_{\text{res}}|^2$  with its momenta being remapped to the on shell kinematics,

$$d\sigma^{\text{OS}} = \Theta(\hat{s} - (m_{ij} + m_k)^2) \Theta(m_{ij} - m_i - m_j) \frac{1}{\frac{1}{m_{ij}^2 \Gamma_{ij}^2}} \left. |\mathcal{M}_{\text{res}}|^2 \right|_{\text{remapped}}. \quad (2.32)$$

The kinematic configuration is depicted in Fig. 2.6. The two step functions in Eq.(2.32) ensure that the partonic center-of-mass energy is sufficient to produce the intermediate on shell particle and that it can decay on shell into the two final-state particles. The ratio of the Breit-Wigner functions ensures that the subtraction has the same profile as the original  $|\mathcal{M}_{\text{res}}|^2$  over the entire phase-space. In the small width limit this ratio reproduces a delta distribution which factorizes the  $2 \rightarrow 3$  diagrams into the pairwise production cross section convoluted with the corresponding branching BR for the on shell resonance,  $\sigma \times \text{BR}$ .

The remapping of the phase-space kinematics to the on shell configuration can be obtained in analogy to the reshuffling of the massive *final-final* dipoles momenta [14]. The reshuffled momenta,  $\tilde{p}_{ij}^\mu$  and  $\tilde{p}_k^\mu$ , are defined in terms of the original momenta  $p_i$ ,  $p_j$  and  $p_k$  by

$$\begin{aligned} \tilde{p}_k^\mu &= \frac{\sqrt{\lambda(Q^2, m_{ij}^2, m_k^2)}}{\sqrt{\lambda(Q^2, (p_i + p_j)^2, m_k^2)}} \left( p_k^\mu - \frac{Q_\nu p_k^\nu}{Q^2} Q^\mu \right) + \frac{Q^2 + m_k^2 - m_{ij}^2}{2Q^2} Q^\mu \\ \tilde{p}_{ij}^\mu &= Q^\mu - \tilde{p}_k^\mu, \end{aligned} \quad (2.33)$$

where the above expressions satisfy the mass-shell conditions and the total momentum conservation

$$\tilde{p}_{ij}^2 = m_{ij}^2, \quad \tilde{p}_k^2 = m_k^2, \quad Q^\mu \equiv p_i^\mu + p_j^\mu + p_k^\mu = \tilde{p}_{ij}^\mu + \tilde{p}_k^\mu. \quad (2.34)$$

Now we reshuffle the momenta of the particles  $i$  and  $j$ , which we denote by  $\tilde{p}_i$  and  $\tilde{p}_j$ . These can be defined by

$$\tilde{p}_i^\mu = \left( \sqrt{m_i^2 + a^2}, a \frac{\vec{p}_i}{|\vec{p}_i|} \right), \quad \tilde{p}_j^\mu = \tilde{p}_{ij}^\mu - \tilde{p}_i^\mu, \quad (2.35)$$

with

$$a = \frac{\vec{p}_{ij} \cdot \vec{p}_i / |\vec{p}_i| ((\tilde{p}_{ij}^0)^2 + m_i^2 - b)}{4(\tilde{p}_{ij}^0)^2 - (\vec{p}_{ij} \cdot \vec{p}_i / |\vec{p}_i|)^2} + 2 \frac{\sqrt{(\tilde{p}_{ij}^0)^2 ((\tilde{p}_{ij}^0)^4 + m_i^4 + b^2 + m_i^2 ((\vec{p}_{ij} \cdot \vec{p}_i / |\vec{p}_i|)^2 - 2b) - 2(\tilde{p}_{ij}^0)^2 (m_i^2 + b))}}{4(\tilde{p}_{ij}^0)^2 - (\vec{p}_{ij} \cdot \vec{p}_i / |\vec{p}_i|)^2} \quad (2.36)$$

and  $b = m_i^2 + m_{ij}^2$ . With these definitions the momenta  $p_i$ ,  $p_j$ ,  $p_k$  reduce in the limit  $\sqrt{p_{ij}^2} \rightarrow m_{ij}$  to  $\tilde{p}_i$ ,  $\tilde{p}_j$ ,  $\tilde{p}_k$ . On this way we obtain a finite and well defined result also in the limit  $\Gamma_{ij}/m_{ij} \rightarrow 0$  because the divergent parts coming from  $|\mathcal{M}_{res}|^2$  are subtracted locally.

Note that this method works with a mathematical regulator  $\Gamma_{ij}$  which can be related to the physical width as in the MC@NLO implementation; alternatively we can interpret it as a mere phase-space parameter, on which the total NLO cross section 2.31 cannot depend once the subtraction term  $d\sigma^{OS}$  is introduced to cancel the on shell component within  $|\mathcal{M}_{res}|^2$ . This allows us, in particular, to realize the limit  $\Gamma_{ij} \ll m_{ij}$  which is used in the original PROSPINO implementation.

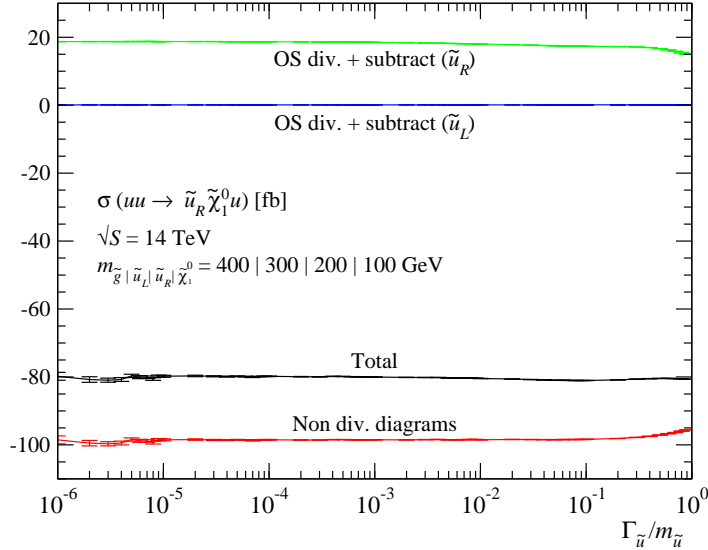


Figure 2.7: NLO contributions from intermediate on shell particles in the sub-channel  $uu \rightarrow \tilde{u}_R \tilde{\chi}_1^0 + X$  production as a function of  $\Gamma_{\tilde{u}}/m_{\tilde{u}}$ . The squark width acts as a mere unphysical cutoff in the PROSPINO subtraction scheme [17, 22]. The masses are chosen to illustrate all different resonant channels; virtual corrections are not included.

In summary, this on shell subtraction implemented in MADGOLEM exhibits several attractive features when it comes to the prediction for the total and differential cross sections. First, it subtracts all on shell divergences point-by-point over the entire phase-space. This means that not only total rates but also all distributions are automatically safe. Second, it preserves gauge invariance, at least in the narrow-width limit. Third, it takes into account spin correlations in the on shell decay  $\tilde{i}\tilde{j} \rightarrow ij$  because it includes the full  $2 \rightarrow 3$  matrix element. Fourth, it keeps track of the interference of the resonant and non-resonant terms,  $2\text{Re}(\mathcal{M}_{\text{res}}^* \mathcal{M}_{\text{rem}})$ , which can be numerically sizeable, at variance with alternative methods used in the literature, *e.g.* diagram removal. Finally, Fig. 2.7 shows that it smoothly interpolates between a finite width  $\Gamma_{ij}/m_{ij} \sim 0.10$  and the narrow-width limit  $\Gamma_{ij}/m_{ij} \rightarrow 0$ . Let us emphasize here the robustness of the MADGOLEM numerical implementation, which provides stable results for values of  $\Gamma/m$  down to  $\mathcal{O}(10^{-6})$ , this is to say, closed by to the actual divergent region from  $|\mathcal{M}_{\text{res}}|^2$ .

## 2.6 Scale dependence

One of the main motivations in calculating the higher order corrections is to lower the dependence of the cross section on the unphysical quantities that we need to introduce as numerical artifacts to cancel the UV and IR divergences, namely the renormalization ( $\mu_R$ ) and factorization ( $\mu_F$ ) scales. Just if we had arbitrarily large number of terms in the  $\alpha_s$  expansion, these dependences would vanish. The fact that it does not in the presence of a fixed number of terms is used as an estimate of the theoretical uncertainties. More precisely, if the calculation is performed to  $\mathcal{O}(\alpha_s^n)$ , the variations of these unphysical scales will lead to an effect of  $\mathcal{O}(\alpha_s^{n+1})$  [4]

$$\mu^2 \frac{d}{d\mu^2} \sigma = \mathcal{O}(\alpha_s^{n+1}), \quad (2.37)$$

with  $\mu \equiv \mu_{R,F}$ . We can understand this expression as a reflect that the dependence in the unphysical parameters appears one order in perturbation theory beyond that of the actual calculation. Namely, it is a NLO effect when looking at the LO cross section (respectively a NNLO effect when considering the NLO cross section). On these lines the scale variation has become a standard procedure to assess these theoretical uncertainties. However, such an estimate must be taken just as a lower limit, since it does not take into account the kinematics of the process itself, which can change substantially with the addition of higher order corrections.

In the absence of all-orders predictions, an important task is to define the scales  $\mu_{R,F}$  in such a way that the uncertainties are minimized, providing a result as close as possible to the ideal all-orders one. Although there are no theorems that prove which is the best scheme to define these scales, it has been shown in numerous cases that choosing them close to the typical momentum scale of a given process leads to stable perturbative results [23, 24]. But this is just an estimation to minimize the scale dependences and there is no replacement for actually performing the higher-order corrections to reduce the uncertainties in a solid way.

The reduction, as we will explicitly observe in several contexts along this thesis, and can be substantial when comparing the the LO and NLO predictions for a given process.

Another fact concerning the scale dependence that is worth mentioning is that, in general, when considering a LO contribution that depends on larger powers of the coupling constant  $\alpha_s$ , this will imply in larger scale uncertainties, in special arising from  $\mu_R$ . In order to have an estimate on the behavior of the uncertainties as a function of  $\mu_R$ , we can use Eq. 2.11 to derive the following relation

$$\mu_R^2 \frac{d\alpha_s^n(\mu_R^2)}{d\mu_R^2} = n \alpha_s^n(\mu_R^2) \frac{\beta(\alpha_s)}{\alpha_s}. \quad (2.38)$$

Therefore, if we have a LO process whose cross section behaves like  $\sigma^{\text{LO}} \sim \alpha_s^n$ , it will imply that

$$\mu_R^2 \frac{d\sigma^{\text{LO}}}{d\mu_R^2} \sim n \frac{\beta(\alpha_s)}{\alpha_s} \sigma^{\text{LO}}. \quad (2.39)$$

From the latter equation we see that the scale uncertainty is proportional to the factor  $n$ , which corresponds to the QCD order of the LO process. This fact we will explicitly see in the following chapters, if we compare the results obtained for the process  $pp \rightarrow \tilde{q}\tilde{\chi}_1^0$  (which is generated at LO with  $\mathcal{O}(\alpha_s\alpha_{EW})$ ) with e.g.  $pp \rightarrow GG^*$  (which is a process generated at LO with  $\mathcal{O}(\alpha_s^2)$ ). The outcome of the comparison shows a lower dependence with  $\mu_R$  for the former process, reflecting the analytical prediction of Eq. 2.39. It is worthwhile noticing that the dependence on the factorization  $\mu_F$  will only rely on the number of active flavors in the initial-state and which will enter the DGLAP evolution equations, which define the running of the pdfs, see Eq. 2.18.

## 2.7 MADGOLEM: Automizing NLO predictions for new physics

One major outcome of our work is the contribution to the automated tool called MADGOLEM, which completely automates the calculation of cross sections and the generation of parton-level events at NLO QCD for arbitrary  $2 \rightarrow 2$  processes in a generic new physics framework.

This tool is build up using the MADGRAPH [6] basic structures, so on the same way the user just needs to specify the process and the model to be analyzed, the parameters of the model and the collider setup, with the help of respective input cards, namely *process\_card*, *param\_card* and *run\_card*. Given this information MADGOLEM automatically provides the NLO amplitudes which are further processed by our event generator giving the NLO cross section, K-factor and the distributions at NLO, as we illustrate in Fig. 2.8.

To provide the NLO amplitude we divide the calculation in several modules highlighted in Fig. 2.8, where each of them is responsible to generated one of the terms in the Eq. 2.31:

- $\mathbf{d}\sigma^{\text{LO}}$  and  $\mathbf{d}\sigma^{\text{real}}$  - For the LO and real emission contributions, which are produced by the tree level matrix element generator from MADGRAPH.

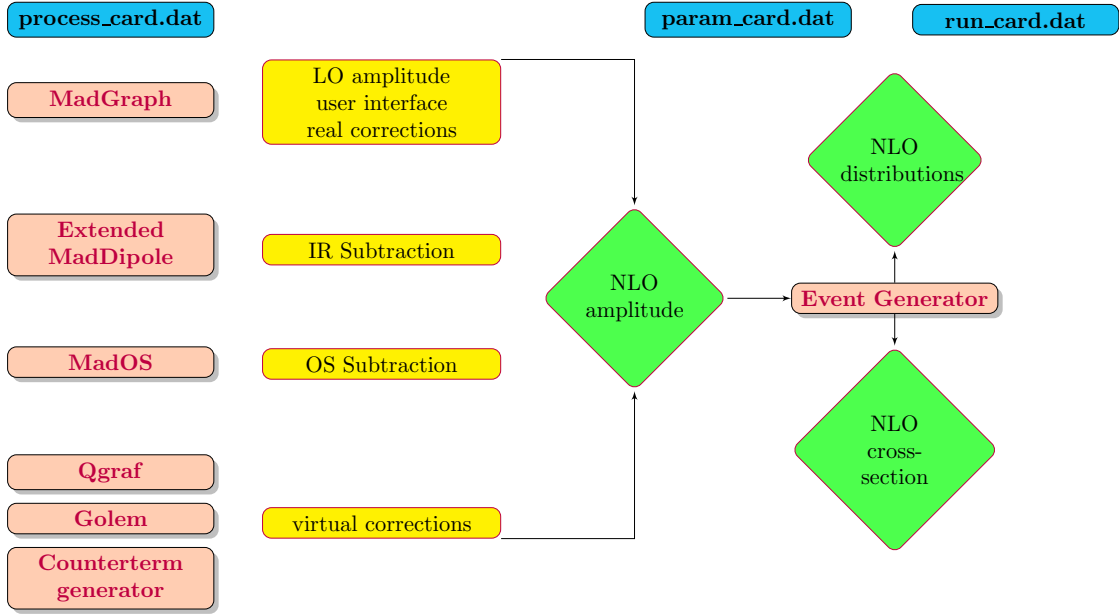


Figure 2.8: Modular structure of MADGOLEM.

- $d\sigma^{\text{A}}$  and  $(d\sigma^{\text{collinear}} + \int_1 d\sigma^{\text{A}})$  - To remove IR divergences from real and virtual corrections we use the Catani-Seymour dipole subtraction [14], which we have introduced in Sec. 2.4. The unintegrated and integrated Catani-Seymour dipoles are automatically generated in our implementation, which we build as an expanded version of MADDIPOLE [25]. In our extension, beyond the Catani-Seymour SM dipoles, we also provide all the dipole structures needed to cope with the new IR divergent structures that appear in the QCD radiation processes involving SUSY particles, as well as other heavy colored resonances, e.g. scalar color-octets, leptogluons, all of them with the FKS-like phase-space parameter  $\alpha$ . For more details see Sec. 2.4 and Appendix A.
- $d\sigma^{\text{OS}}$  - The counter term which is responsible to subtract possible double counting arising from on shell resonances is automatically generated by our own module MADOS, which is process and model independent. Given one process, this module identifies which are the possible on shell resonances associated to the real emission matrix element  $\mathcal{M}_{m+1}^{(\text{tree})}$ . From this starting point, the respective set of subtraction terms of Eq. 2.32 is generated. Beyond the generation of these terms, MADOS also takes care of the required reshuffling of momenta on the counter term expressions when performing the phase-space integration, in order to subtract all the on shell resonances locally. For more details on the On Shell subtraction method see Sec. 2.5.
- $d\sigma^{\text{virtual}}$  - The virtual corrections are generated by a combination of QGRAF [26], GOLEM [27, 28] and our own counter term generator. These we describe in more detail further down.

The calculation of the virtual contributions starts with QGRAF providing all the possi-

ble one-loop Feynman diagrams for the required process. This QGRAF output is translated by MADGOLEM into a code suitable for symbolic calculation languages. This is done by rewriting the Feynman diagrams and Feynman rules into algebraic expressions which keep track of external wave functions, vertex couplings and internal propagators, color factors, Lorentz structure, and the overall sign from external fermion fields. This feature allows MADGOLEM to deal with genuine features of new physics processes, e.g. Majorana fermions. Then MADGOLEM maps the amplitudes into a basis of color, helicity and tensor structures. This is followed by the reduction into a basis of scalar loop integrals using GOLEM, which applies a modified version of the Passarino-Veltman reduction scheme. As a last step, the UV counter terms implemented in MADGOLEM are combined with the genuine one-loop amplitude. The latter are expressed in terms of two-point functions and are supplied in a separate library. For more details on the renormalization procedure see Appendix B.

One particularly distinctive feature within the MadGolem, its one-loop matrix element calculation follows a fully analytical, Feynman-diagrammatic approach, based on spinor helicity and color flow techniques, as well as on the mentioned Golem implementation of the Passarino-Veltman scheme for the tensor reduction of the one-loop Lorentz structures. The user can therefore access and retrieve the analytical form of the amplitude at different stages through the entire calculation. It also allows for an explicit selection and/or separation of the different one-loop NLO contributions, for instance in terms of topologies: self-energies, boxes, and vertex corrections to the different interactions (feature which we will make extensive use in the physics analyses contained in this thesis).

Alternative methods to address the automated calculation of one-loop amplitudes resort to the use of the so-called generalized unitarity [29] and on shell reduction methods [30]. Based on different combinations of strategies to carry out the calculation of the tree-level and one-loop amplitudes, and the automated handle of the renormalization of the UV poles and the subtraction of the IR singularities, a number of independent, and nicely complementary approaches to fully automated NLO tools are currently underway. These include aMC@NLO [31], BlackHat/Sherpa [9], FeynArts/FormCalc/LoopTools [7], HELAC-NLO [32], GoSam [27] and MadGolem [36–38].

MADGOLEM is meant to be a fully automatic program. Therefore it does not require from the user any further intervention than the setup of the process through the basic input cards, depicted in blue in Fig. 2.8. Default MADGRAPH options like multi-particle notation are supported together with additional specifications that allow us, for instance, to separate QCD from SUSY-QCD effects or retain specific subsets of one-loop contributions.

## 2.8 Numerical tests

An exhaustive cross-checking program we have undertaken to ensure the robustness and reliability of MADGOLEM. The total NLO rates and corresponding  $K$  factors we have calculated for a wide variety of  $2 \rightarrow 2$  processes both within the SM and the MSSM, covering all representative possibilities of spin and color representations, interactions and topologies. The

Processes	Check against
$e^+e^- \rightarrow q\bar{q}$ - massless and massive final state	analytical calculation [14]
$e^+e^- \rightarrow \tilde{q}\tilde{q}$ - final state correction	Zerwas <i>et al</i> [33]
$pp \rightarrow \tilde{l}\tilde{l}$ - initial state correction	PROSPINO [24]
$pp \rightarrow \tilde{q}\tilde{\chi}$ - colored particles in the initial/final state	FEYNARTS, FORMCALC, LOOPTOOLS [7]
$pp \rightarrow GG^*$ - fully colored process	FEYNARTS, FORMCALC, LOOPTOOLS [7]
$pp \rightarrow \tilde{q}\tilde{q}(\tilde{q}\tilde{g})[\tilde{g}\tilde{g}]\{\tilde{q}\tilde{q}^*\}$ - fully colored processes	PROSPINO [17–19]

Table 2.2: Summarized cross-check table which documents some of the tested processes in MadGOLEM with the respective source of comparison. The comparisons against FEYNARTS, FORMCALC, LOOPTOOLS concerns only the finite part of the one-loop amplitudes.

cancellation of the UV and IR divergences, as well as the gauge invariance of the overall result, has been explicitly confirmed (in all cases numerically, and also analytically for some specific ones). As for the finite parts of the renormalized one-loop amplitudes, we have systematically compared them with the results from independent calculations performed with FEYNARTS, FORMCALC and LOOPTOOLS [7]. Particular care we have devoted to the numerical stability and the convergence of the results, ensuring a robust implementation of the Catani-Seymour dipoles and the On Shell subtraction method. The specific performance of the dipoles, as well as of the On Shell subtraction terms nearby the singular regions, has been carefully investigated including, e.g. *i*) The  $\alpha$ -parameter independence of the subtraction procedure from the arbitrary phase-space regulator we use, as presented in the right plot of Fig. 2.9; *ii*) The numerical convergence of the cross section when the on shell contributions we subtracted for small regulators  $\Gamma_{ij} \ll m_{ij}$ , as presented in Fig. 2.7.

In addition, the MADGOLEM total NLO rates and corresponding  $K$  factors we have exhaustively contrasted to the numerical outcomes from PROSPINO. In order to conduct such a systematic comparison we have settled common parameter benchmarks, probing all the different squark/gluino mass hierarchies, and so all possible on shell divergent configurations. The results we have checked for all the available channels in PROSPINO, considering both the LHC ( $pp$ ) and the Tevatron ( $p\bar{p}$ ) colliders and for several center-of-mass energies. For each of the production processes, we have explicitly separated the different partonic subchannels and compared them independently. Agreement has been confirmed in all cases at the percent level.

As an explicit example for the numerous numerical tests that we performed, we present here one cross-check of the dipole subtraction for soft gluon emission off the squark final-state in the hard process  $e^+e^- \rightarrow \tilde{u}_R\tilde{u}_R^*$ . In the left panel of Fig. 2.9 we show how the dipole subtraction cancels the IR divergence locally, *i.e.* point by point in phase-space. Observe that the matrix element for the real emission presents values spanning in the range from  $\mathcal{O}(10^{-8})$  (when far from the soft limit) to  $\mathcal{O}(10^8)$  (when going towards the soft limit  $y_{g\tilde{q},k} \rightarrow 0$ ). However the dipole subtraction terms match them in the whole soft range, canceling the possible IR divergencies. This we can read off the flat profile of the curve  $\sum_{\text{dipoles}} D_{g\tilde{q},k}/|\mathcal{M}_{\text{real}}^2|$

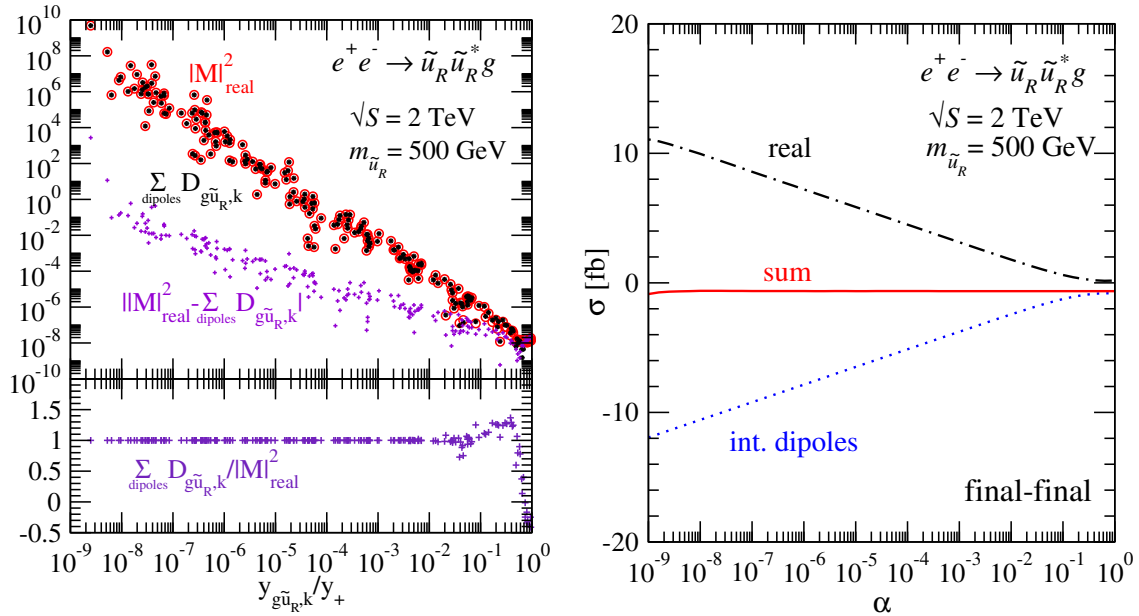


Figure 2.9: Left: real emission matrix element (red circles) and the dipole subtraction (black crosses inside) towards the soft limit  $y_{g\tilde{q},k} \rightarrow 0$ . Right:  $\alpha$  dependence for final-final squark dipoles.

(displayed in the bottom panel of the plot) and also in the overlap of the black dots with the red circles (displayed in the top panel of the plot). In fact, the numerical agreement of the real emission matrix element with the dipole subtraction term improves for softer gluons. In the soft limit both terms grow as  $1/E_g^2$ . Even though we find  $|\mathcal{M}_{\text{real}}^2 - \sum_{\text{dipoles}} D_{g\tilde{q},k}| \sim 1/E_g$  (in magenta) the phase-space factor  $E_g dE_g$  cancels this dependence.

In the right panel of Fig. 2.9 we show the  $\alpha$  dependence for the final-final squark dipole. Both the real emission and the integrated dipole depend separately on  $\alpha$ . Their sum, instead, does not. This is precisely what the subtraction prescription requires. No trace of an eventual dependence on the  $\alpha$  parameter is left and the result remains numerically stable over many orders of magnitude down to  $\alpha = \mathcal{O}(10^{-9})$ . More details on the  $\alpha$  parameter see Appendix A.

## Chapter 3

# Sgluon pair production

Scalar gluons (sgluons) are color-octet scalars without electroweak charges. They appear in various extensions to the SM as composite or fundamental degrees of freedom. The most well-know example we find in extended supersymmetric models like the R-symmetric MSSM [34] or  $\mathcal{N} = 1/\mathcal{N} = 2$  hybrid models [35], where the sgluons emerge as scalar partners of a Dirac gluino. At the LHC the sgluon pairs will be copiously produced by their couplings to gluons, with the most generic signature being  $pp \rightarrow GG^* \rightarrow 4$  jets [39].

In this chapter we present a complete next-to-leading order QCD calculation of sgluon pair production at the LHC. We examine the features and quantitative impact of the QCD quantum effects on the production rates and the sgluon distributions. The results presented in this chapter are based on the publication [37]. We also present the status of the current searches from the ATLAS collaboration [39], where the theoretical prediction for the sgluon pair productions at NLO is produced by our code MADGOLEM.

### 3.1 Theoretical setup

Our calculation is based on the minimal extension of the SM where the gluonic QCD corrections to sgluon pair production are well defined and it can be interpreted as the relevant QCD part of an effective strongly interacting theory. Following this approach we minimally extend the SM by one additional color octet, weak singlet, electrically neutral, and complex scalar field  $G$ . With the sgluons coupling to the SM particles only through the covariant derivative,  $D_\mu G^A \equiv \partial_\mu G^A + g_s f^{ABC} G^B A_\mu^C$ , where  $A_\mu^C$  denotes the gluon field,  $g_s$  the strong coupling constant, and  $f^{ABC}$  the adjoint  $SU(3)$  generators. The sgluon dynamics is defined by the lagrangian

$$\begin{aligned} \mathcal{L} &\supset D_\mu G^* D^\mu G - m_G^2 G G^* \\ &\supset -g_s f^{ABC} [G^{A*} (\partial^\mu G^B) - (\partial^\mu G^{A*}) G^B] A_\mu^C \\ &\quad + g_s^2 [f^{ACE} f^{BDE} + f^{ADE} f^{BCE}] G^{C*} G^D A_\mu^A A^{B\mu}. \end{aligned} \tag{3.1}$$

Therefore from the 3 and 4 point interaction terms in Eq. 3.1 we can derive that there are only two production channels at leading order

$$q\bar{q} \rightarrow GG^* \quad \text{and} \quad gg \rightarrow GG^* \quad (3.2)$$

with the correspondent Feynman diagrams depicted in Fig. 3.1.

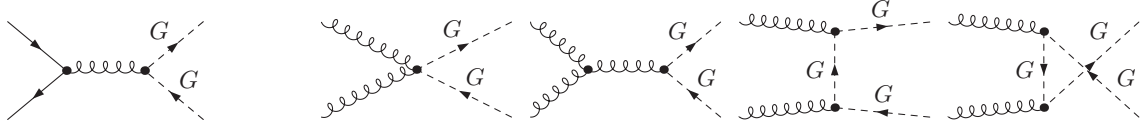


Figure 3.1: Leading order Feynman diagrams for sgluon pair production via quark-antiquark annihilation and gluon fusion.

The corresponding total cross sections at the tree-level can be written as [35]

$$\sigma(q\bar{q} \rightarrow GG^*) = \frac{4\pi\alpha_s^2}{9s}\beta_G^3, \quad (3.3)$$

$$\sigma(gg \rightarrow GG^*) = \frac{15\pi\alpha_s^2\beta_G}{8s} \left[ 1 + \frac{34m_G^2}{5s} - \frac{24m_G^2}{5s} \left( 1 - \frac{m_G^2}{s} \right) \frac{1}{\beta_G} \log \left( \frac{1 + \beta_G}{1 - \beta_G} \right) \right] \quad (3.4)$$

where  $\sqrt{s}$  is the invariant parton-parton energy and  $\beta_G = (1 - 4m_G^2/s)^{1/2}$  is the center-of-mass velocity of the  $G$  particle.

From Eqs. 3.3 and 3.4 we notice that while the gluon fusion increases near the threshold with  $\sigma_{gg} \sim \beta_G$ , as characteristic of the  $s$ -wave component of the 4-point  $ggGG^*$  interaction, the quark-antiquark annihilation increases as  $\sigma_{q\bar{q}} \sim \beta_G^3$ , which corresponds to a  $p$ -wave component of the derivative coupling  $gGG^*$ . Notice also the asymptotical scaling of the partonic cross section with  $\sigma \sim s^{-1}$  either for quark-antiquark annihilation or gluon fusion.

There is an important SUSY process which shares some similarities to  $pp \rightarrow GG^*$ , namely squark pair production, when considering the gluinos decoupled. This process leads to the same diagrams as in Fig. 3.1 with the adjoint final state scalars  $G$  replaced by fundamental final state scalars  $\tilde{q}$ . Therefore at tree-level their differences can be traced back to the relative strength of the color interactions [35]

$$\frac{\sigma(q\bar{q} \rightarrow GG^*)}{\sigma(q\bar{q} \rightarrow \tilde{q}\tilde{q}^*)} = \frac{\text{tr}(\frac{\lambda^a}{2} \frac{\lambda^b}{2})\text{tr}(F^a F^b)}{\text{tr}(\frac{\lambda^a}{2} \frac{\lambda^b}{2})\text{tr}(\frac{\lambda^a}{2} \frac{\lambda^b}{2})} = 6 \quad \text{for any } \beta_G, \quad (3.5)$$

$$\frac{\sigma(gg \rightarrow GG^*)}{\sigma(gg \rightarrow \tilde{q}\tilde{q}^*)} = \begin{cases} \frac{\text{tr}(\{F^a, F^b\}\{F^a, F^b\})}{\text{tr}(\{\frac{\lambda^a}{2}, \frac{\lambda^b}{2}\}\{\frac{\lambda^a}{2}, \frac{\lambda^b}{2}\})} = \frac{216}{28/3} \approx 23 & \text{for } \beta_G \rightarrow 0, \\ \frac{\text{tr}(2F^a F^b F^b F^a + F^a F^b F^a F^b)}{\text{tr}(2\frac{\lambda^a}{2} \frac{\lambda^b}{2} \frac{\lambda^b}{2} \frac{\lambda^a}{2} + \frac{\lambda^a}{2} \frac{\lambda^b}{2} \frac{\lambda^a}{2} \frac{\lambda^b}{2})} = 18 & \text{for } \beta_G \rightarrow 1. \end{cases} \quad (3.6)$$

Thus, the larger color charge of the sgluons expresses that they will be more copiously produced than squarks of the same mass.

## 3.2 Production rates at NLO

In this section we will present the total rates for  $pp \rightarrow GG^*$  and some features characterizing the NLO corrections to this process. The numerical analysis is performed with the MAD-GOLEM package, using the CTEQ6L1 and CTEQ6M as the LO and NLO parton densities with 5 flavors [40]. We set the factorization and renormalization scales at the average of the final state mass  $\mu^0 = \mu_R = \mu_F = m_G$ , which represents the energy scale of the process and has been shown to provide stable perturbative results [17]. For the strong coupling we use the corresponding  $\alpha_s(\mu_R)$ . Its value is given by the two-loop running from  $\Lambda_{QCD}$  to the required scale  $\mu_R$  with five active flavors. Unless stated otherwise we set the LHC center of mass energy at  $\sqrt{S} = 8$  TeV and the sgluon mass to  $m_G = 500$  GeV.

In Table 3.1 we present the total cross sections and corresponding  $K$ -factors ( $K = \sigma^{NLO}/\sigma^{LO}$ ) for different sgluon masses and LHC energies. We observe that the NLO corrections are generally large,  $K > 1.5$ . For LHC energies of 7 TeV or 8 TeV and particle masses between 500 GeV to 1 TeV we observe that the  $K$ -factor becomes unexpectedly large. This is a well-know fact also in the supersymmetric particle production, which is not to be seen as a sign of poor perturbative behavior but as an artifact of the LO CTEQ parton densities which tend to provide artificially suppressed rates [40, 41].

$m_G$ [GeV]	$\sqrt{S} = 7$ TeV			$\sqrt{S} = 8$ TeV			$\sqrt{S} = 14$ TeV		
	$\sigma^{LO}$ [pb]	$\sigma^{NLO}$ [pb]	$K$	$\sigma^{LO}$ [pb]	$\sigma^{NLO}$ [pb]	$K$	$\sigma^{LO}$ [pb]	$\sigma^{NLO}$ [pb]	$K$
200	$1.40 \times 10^2$	$2.26 \times 10^2$	1.61	$2.12 \times 10^2$	$3.36 \times 10^2$	1.58	$9.77 \times 10^2$	$1.48 \times 10^3$	1.52
350	$4.83 \times 10^0$	$8.21 \times 10^0$	1.70	$8.16 \times 10^0$	$1.36 \times 10^1$	1.66	$5.44 \times 10^1$	$8.46 \times 10^1$	1.56
500	$4.05 \times 10^{-1}$	$7.32 \times 10^{-1}$	1.81	$7.64 \times 10^{-1}$	$1.34 \times 10^0$	1.75	$7.14 \times 10^0$	$1.14 \times 10^1$	1.60
750	$1.48 \times 10^{-2}$	$3.01 \times 10^{-2}$	2.03	$3.40 \times 10^{-2}$	$6.54 \times 10^{-2}$	1.93	$5.56 \times 10^{-1}$	$9.29 \times 10^{-1}$	1.67
1000	$8.60 \times 10^{-4}$	$2.00 \times 10^{-3}$	2.33	$2.47 \times 10^{-3}$	$5.29 \times 10^{-3}$	2.15	$7.31 \times 10^{-2}$	$1.28 \times 10^{-1}$	1.75

Table 3.1: Total  $pp \rightarrow GG^*$  cross sections and corresponding  $K$ -factors for different sgluon masses and LHC energies.

In Fig. 5.8 we provide a study of the LO and NLO cross sections as a function of the sgluon mass. The left panel displays it is shown the total LO and NLO rates with their corresponding theoretical uncertainties. These are estimated by the factorization and renormalization scale variation in the range  $\mu^0/2 < \mu_{R,F} < 2\mu^0$ . From the size of the envelopes we observe a clear reduction of the uncertainties when going from LO to NLO. A more detailed analysis of the scale dependences see Sec. 3.3.

In order to understand the structure of the NLO corrections, in the right panel of Fig. 5.8 we separate the contributions from the different partonic sub-channels:  $q\bar{q}$ ,  $gg$  and the purely NLO crossed channel triggered by the  $gq/g\bar{q}$  initial state. We observe the dominance of the gluon fusion sub-channel, which is approximately two orders of magnitude larger than the second most important one ( $q\bar{q}$ ). The reason for this can be traced back at:

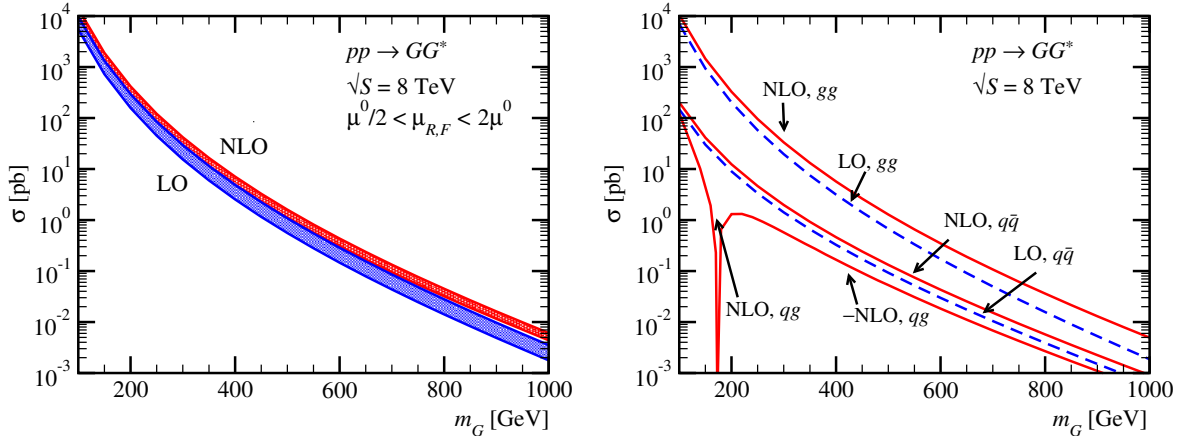


Figure 3.2: LO and NLO cross sections  $\sigma(pp \rightarrow GG^*)$  as a function of the sgluon mass. The band corresponds to a scale variation  $\mu^0/2 < \mu_{R,F} < 2\mu^0$ . In the right panels we explicitly separate the contributions from the different partonic sub-channels,  $q\bar{q}$ ,  $gg$  and also  $gq$ .

- In Eqs. 3.3 and 3.4 we observe that the color charge in the four color-octet interaction is larger than in the triplet-octet.
- The  $gg$  sub-channel benefits from some particular kinematic features. As we discussed after Eqs. 3.3 and 3.4, at the threshold the total partonic cross sections scales as  $\sigma_{gg} \sim \beta_G$  corresponding to a  $s$ -wave while the  $q\bar{q}$  scales as  $\sigma_{q\bar{q}} \sim \beta_G^3$  corresponding to a  $p$ -wave. Hence, the former dominates at the vicinity of the threshold.
- Moreover the threshold region corresponds to low- $x$  where the gluon parton densities become larger and dominate.

It is important to notice that the initial states  $gq/g\bar{q}$  are purely NLO sub-channels, *i.e.* they do not have correspondent LO processes. In the absence of the tree-level piece, there is no NLO virtual correction arising from them, since  $\sigma^{\text{Virtual}} = \int d\Phi_2 2\text{Re}[\mathcal{M}^{\text{LO}*} \mathcal{M}^{\text{Virtual}}]$ . However we still need to account for the initial-initial and initial-final Catani-Seymour dipoles and the collinear counterterm  $d\sigma^{\text{Collinear}}$  associated with their corresponding genuine NLO contributions.

### 3.3 Scale dependence

One of the main motivations for calculating the high order corrections is to lower the dependence of the cross section on the unphysical quantities that we need to introduce as numerical artifacts to cancel the UV and IR divergences, namely renormalization ( $\mu_R$ ) and factorization ( $\mu_F$ ) scales, reducing on this manner the theoretical uncertainties. These scales are responsible to remove the UV and IR divergences order by order in perturbation theory. Only for an arbitrarily large number of terms in the  $\alpha_s$  expansion, these dependencies would vanish. The fact that it does not in the presence of a fixed number of terms is used to provide a

handle on the uncertainties estimation. This explains why the scale variation has become a standard procedure for the assessment of these theoretical uncertainties.

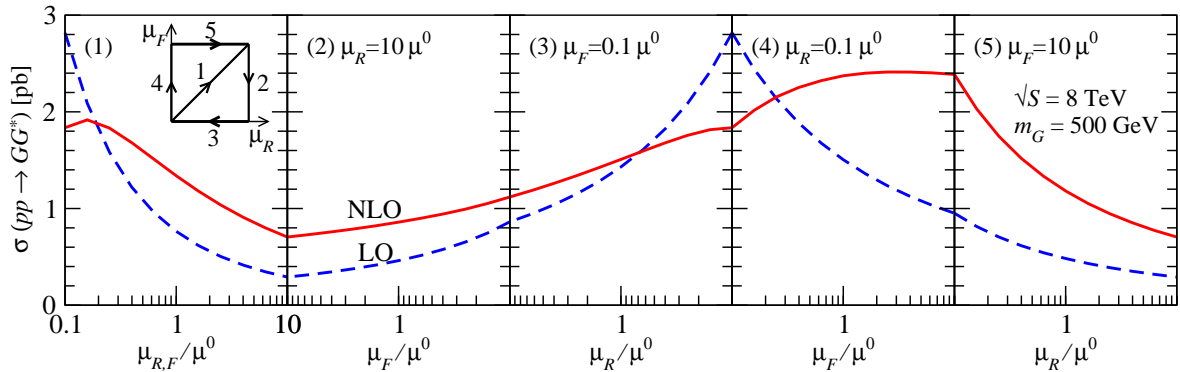


Figure 3.3: Renormalization and factorization scale dependence. The plot traces the scale dependence following a contour in the  $\mu_F$ - $\mu_R$  plane in the range  $\mu = (0.1 - 10) \times \mu^0$  with  $\mu^0 = m_G$ , as illustrated in the little square in the first panel. The sgluon mass we fix to  $m_G = 500$  GeV.

The scale variation analysis in general should be done via independent variation of the two scales, since they have different origins which makes them independent quantities. In Fig. 3.3 we show the scale dependence for the  $pp \rightarrow GG^*$  production at LO and NLO, moving along the contour in the  $\mu_R$ - $\mu_F$  plan. The contour is illustrated in the little square in the first panel. The individual scale variation is chosen as  $\mu^{(0)}/10 < \mu < 10\mu^{(0)}$ , where  $\mu^{(0)}$  stands for our central value choice  $\mu^{(0)} = m_G = 500$  GeV. The stabilization of the scale dependence becomes apparent as a smoother profile in the  $\sigma^{\text{NLO}}$  slope. From this plot we can also infer that the renormalization scale dependence dominates the combined scale dependence. Quantitatively, we obtain that the LO uncertainty ranges around  $\Delta\sigma^{\text{LO}}/\sigma^{\text{LO}} \sim \mathcal{O}(80\%)$ , while the addition of the next-to-leading order corrections reduces to approximately  $\Delta\sigma^{\text{NLO}}/\sigma^{\text{NLO}} \sim \mathcal{O}(30\%)$ .

### 3.4 Real and virtual corrections

Real emission corrections to sgluon pair production arise from three particle final state contributions  $pp \rightarrow GG^*j$  at order  $\alpha_s^3$ , where the extra jet can be  $j = g, q, \bar{q}$ . Fig. 3.4 displays a sample of the real emission diagrams. In Fig. 3.4a we observe the appearance of a new type of diagonal splitting which is not present in the SM, namely  $G \rightarrow Gg$ . This splitting from a color-octet scalar leads to a new type of infrared divergencies not present in the SM Catani-Seymour dipoles available in the MADDIPOLE [25] implementation. In order to deal with these novel type of divergencies we include the corresponding sgluon dipoles in MADGOLEM. These divergences arise when the sgluons radiate soft gluons requiring new final-final and final-initial dipoles to subtract the IR divergencies. As a colored particle, sgluons perform as spectator partons, however the dipole function only carries information about the mass of the spectator particle, not about its spin. Therefore we can simply use the SM dipoles in the

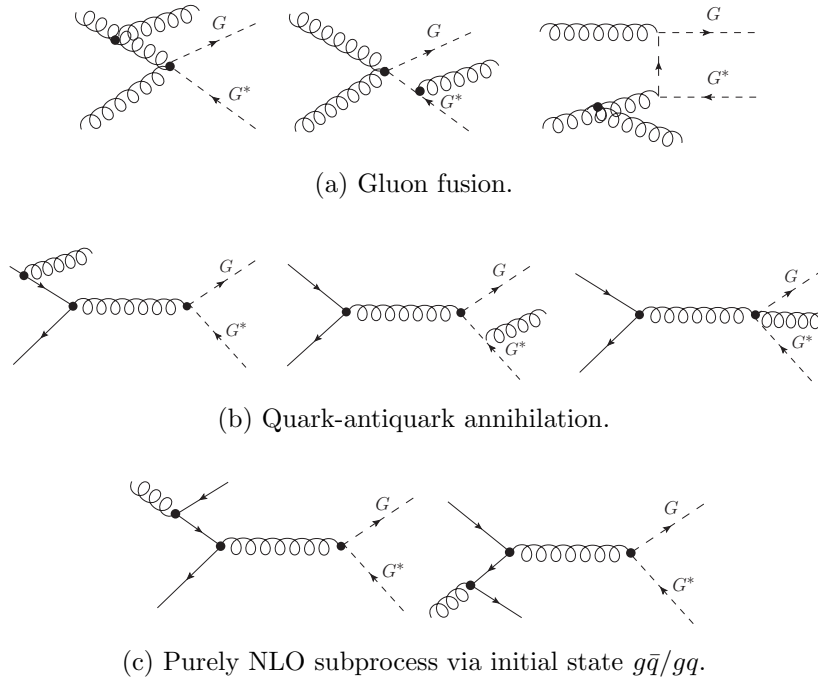


Figure 3.4: Sample Feynman diagrams for real emission corrections to sgluon pair production denoting the different initial state subchannels.

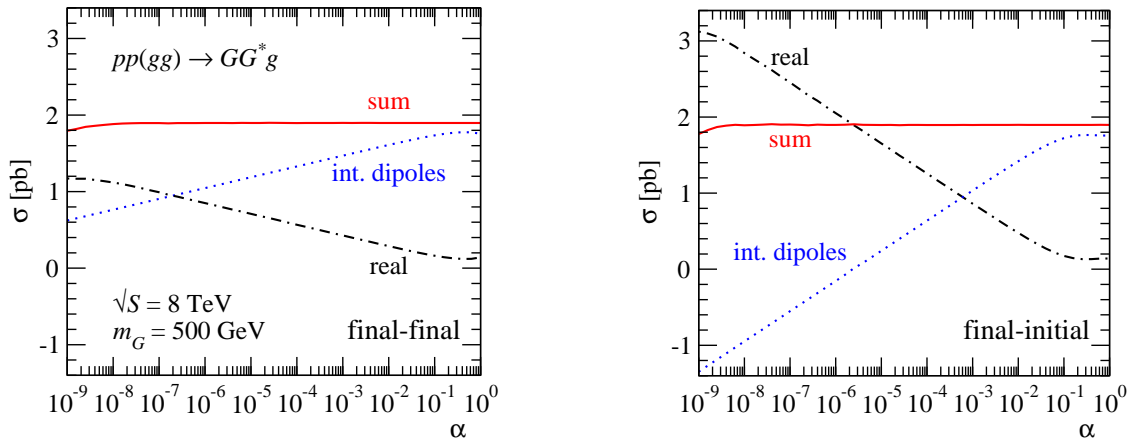


Figure 3.5:  $\alpha$  dependence of the final-final (left) and final-initial (right) sgluon dipoles for the sub-process  $gg \rightarrow GG^*g$ .

initial-final case. For more details see Appendix A. There we present the new sgluon dipoles including the FKS-style phase-space parameter  $0 < \alpha \leq 1$  [42]. In Fig. 3.5 we prove that the cross section is numerically stable for a very wide range  $\alpha = 1 - 10^{-8}$ , which confirms the satisfactory performance of the procedure and highlights its numerical stability, which holds down to phase-space regions close to the actual instability,  $\alpha \rightarrow 0$ .

Virtual corrections to  $pp \rightarrow GG^*$  arise from all possible one-loop exchanges of the virtual gluons to quarks and sgluons. Dimension regularization is used to regulate the UV divergen-

cies, where the number of dimensions is  $d = 4 - 2\epsilon$ . In order to remove the UV divergences one has to include the proper counterterms, which implement the renormalization of the strong coupling constant and the sgluon mass. For more details in the renormalization procedure see Appendix B. It is important to highlight that as an internal check we use an independent implementation of our sgluon model in FEYNARTS. This way we could numerically check our MADGOLEM virtual corrections to the output from FEYNARTS, FORMCALC and LOOPTOOLS [7].

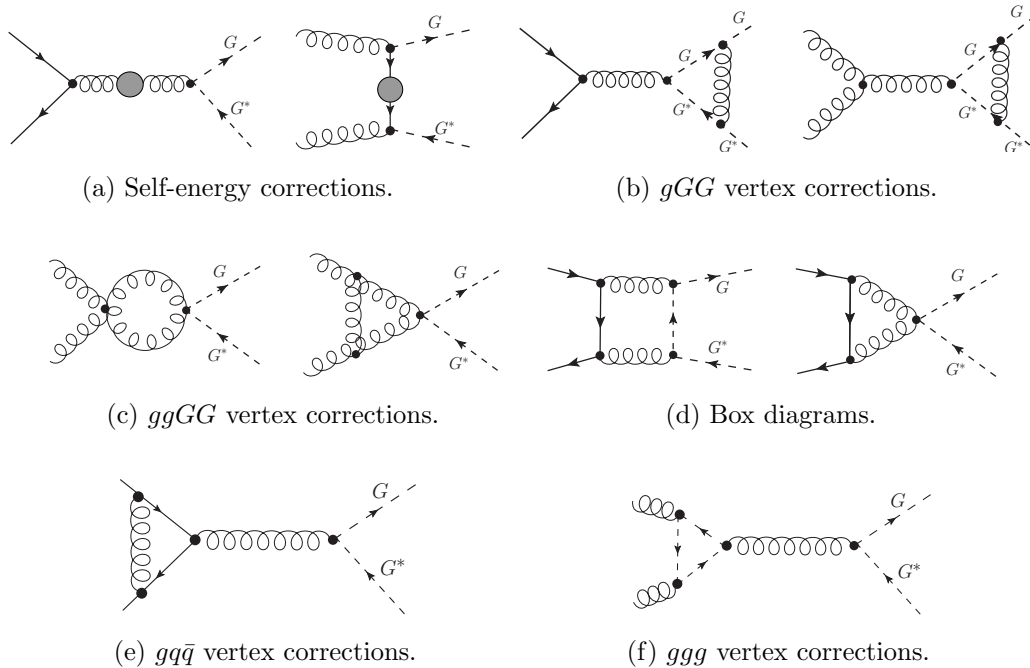


Figure 3.6: Sample Feynman diagrams for virtual corrections to sgluon pair production via quark-antiquark annihilation and gluon fusion.

We organize a sample of the virtual correction Feynman diagrams in Fig. 3.6. They are divided into self-energy insertions, vertex corrections to the couplings  $gGG$ ;  $ggGG$ ;  $gq\bar{q}$  and box contributions. In Fig. 3.7 we separately examine the different contributions of the real and virtual NLO corrections to the hadronic process  $pp \rightarrow GG^*$  as a function of the sgluon mass. We explore the relative contribution of each class of one-loop corrections as denoted in Figs. 3.4 and 3.6 normalizing each piece by the LO cross section,  $\Delta\sigma^{NLO}/\sigma^{LO}$ . We distinguish two partonic subprocesses  $gg$  (left panel) and  $q\bar{q}$  (right panel). In this specific analysis we left aside the  $gq/g\bar{q}$  channels, which have a minor contribution to the total rate and, as we discussed previously, do not develop virtual corrections.

The bulk of the NLO quantum corrections arises from real emission and the  $gGG$  vertex corrections. Both of them grow with the sgluon mass and for intermediate sgluon masses of approximately  $m_G = 500$  GeV each contribution amounts to a correction of roughly 40%. The real corrections reach up to 100% for sgluons with masses at the TeV scale. As QCD corrections to our supersymmetric setup are well defined this rise in the correction with mass

cannot be interpreted as a break-down of perturbation theory. In fact we can interpret their increase with the sgluon mass from the threshold behavior of the NLO corrections, since the real emission diagrams have more contribution with the 4-point interaction vertex  $ggGG^*$  than the LO part.

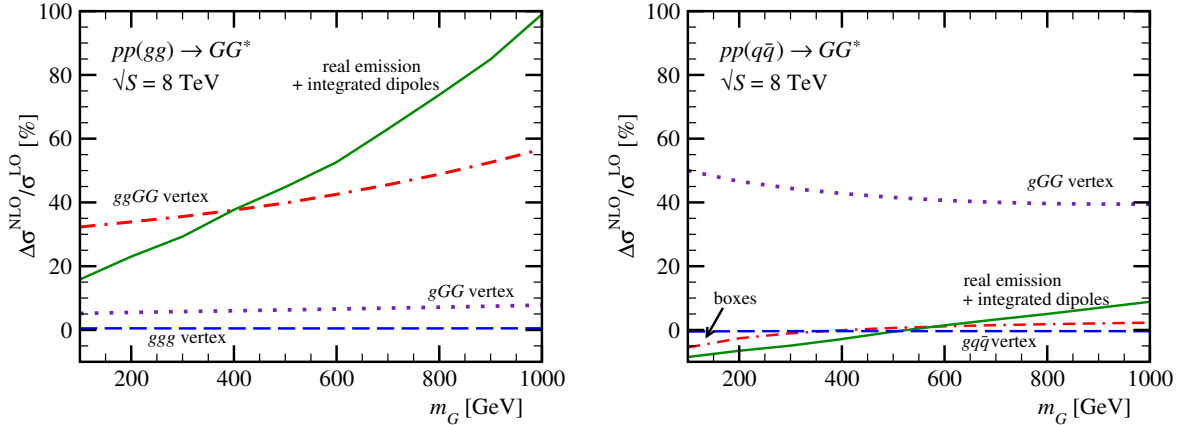


Figure 3.7: Relative size  $\Delta\sigma^{\text{NLO}}/\sigma^{\text{LO}} \equiv (\sigma^{\text{NLO}} - \sigma^{\text{LO}})/\sigma^{\text{LO}}$  of the real emission and virtual corrections to  $\sigma(pp \rightarrow GG^*)$  as a function of the sgluon mass  $m_G$ . We separate the partonic  $gg$  (left) and  $q\bar{q}$  (right) initial states. The contribution from the self-energies is negligible and not explicitly shown.

### 3.5 Distributions: fixed order versus multi-jet merging

As we have seen for the specific case of  $pp \rightarrow GG^*$ , predictions based on the NLO cross section incorporate significant improvements on the central values and theory uncertainties. Now we want to ensure that these improvements hold also for the main distributions, adequately describing their shapes.

We establish this comparison to the multi-jet merging computation [43, 44]. This method has been shown to capture the main features of the processes and yield very satisfactory description of experimental data concerning the shapes of distributions. The method consists of the combination, without double counting, of the tree-level multi-jet matrix elements of varying jet multiplicity with the parton showers. The former captures the features of the process where the partons are hard and well separated and the latter the features of the partons in the soft/collinear approximation, resumming the large logs. Therefore it merges two complementary limits. The matching procedure between the matrix element calculation and the parton shower satisfies a set of criteria that eliminate the double counting of the effects that would be accounted for by both descriptions.

It is worth mentioning that despite the improvements in shapes for the multi-jet merged approach, the overall normalization of the distributions depend to some degree on the merging parameters. Therefore, to get a proper normalization the approach generally chosen is the normalization of the multi-jet merged distributions to the NLO rate.

In Fig. 3.8 we quantitatively check how well the NLO distributions from our fixed order MADGOLEM computation perform in terms of shapes, when compared to the multi-jet merging computation. For the latter we report to the MLM scheme [43] with up to two hard jets using MADGRAPH 4.5 [45] interfaced with PYTHIA [46]. The NLO and multi-jet merging distributions are normalized to unity. We also present the LO, real and virtual contributions to the NLO distributions separately and are shown to scale. It is important to point out that the inclusion of just one hard jet instead of two jets in the merging prescription does not change the results within the numerical precision.

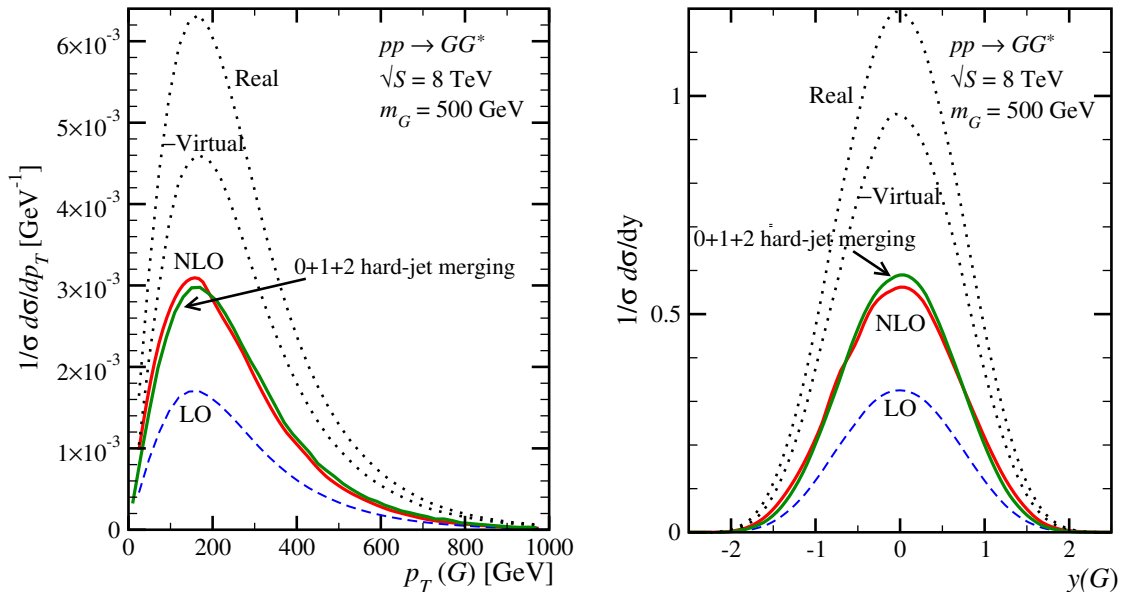


Figure 3.8: Sgluon transverse momentum and rapidity distributions at parton level. We assume  $m_G = 500$  GeV and  $\sqrt{S} = 8$  TeV. For the NLO curves we separately display the LO, virtual, and real contributions ( $\alpha = 10^{-3}$ ). In addition, we show the corresponding distributions based on multi-jet merging in the MLM scheme [43] with up to two hard radiation jets. The NLO and merged results are normalized to unity while the different contributions to the NLO rates are shown to scale.

We observe that the NLO and merged distributions agree very well either for the sgluon transverse momentum or rapidity. The small differences like the slightly harder  $p_T$  profile for the MLM prediction are attributed to the additional recoil jets. We observe this by comparing the real emission distributions and the LO ones. From the left panel of Fig. 3.8 we see a slightly harder profile for the real emissions. Analogously, in the right panel we observe slightly more central sgluons in the merged distributions. This we can understand as a balance of the first emission with the second jet in the initial state.

### 3.6 Status of the current searches

Assuming a SUSY embedding for our effective description of the sgluon dynamics, the sgluon pair production would not depend at tree-level on the supersymmetric parameters, except on the mass of the sgluon itself, which would be related to the soft-SUSY breaking mechanism. It has been shown that sgluons with masses of the order of 100 GeV are expected to decay to two gluons with a branching ratio close to one [34, 35], where the sgluon-gluon-gluon by the one-loop interchange of squarks. From this an effective dimension-five operator is obtained [34]

$$\mathcal{L}_{Ggg}^{5D} \propto \frac{g_s^3}{16\pi^2} \frac{m_{\tilde{g}}}{m_G^2} (f^{abc} G^a F_{\mu\nu}^b F^{c\mu\nu} + h.c.) \quad (3.7)$$

allowing the decay  $G \rightarrow gg$ .

The ATLAS collaboration has performed a recent search for sgluons [39]. It assumes the pair production of scalar gluons, each decaying as  $G \rightarrow gg$ , leading to a four-jet final state. The analysis uses the data sample collected in the year 2011 corresponding to the integrated luminosity of  $4.6 \text{ fb}^{-1}$  with center of mass energy  $\sqrt{s} = 7 \text{ TeV}$ . The main challenge of this analysis is to manage the enormous QCD multi-jet background, which exceeds the signal by orders of magnitude.

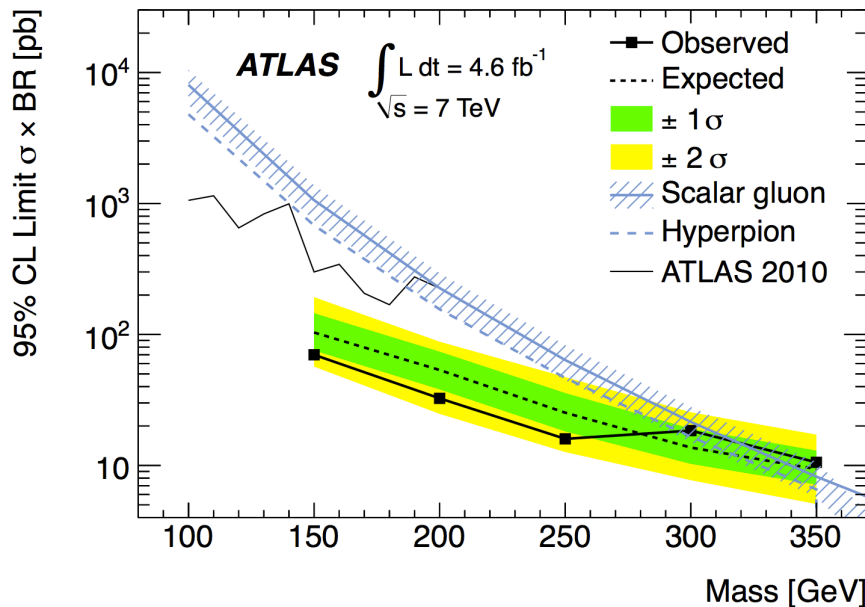


Figure 3.9: The 95% C.L. upper limits on the sgluon pair production cross sections  $\times$  branching ratio to gluon pair as a function of the sgluon mass. Analysis performed by the ATLAS collaboration [39]. The theoretical prediction for the sgluon pair productions at NLO was produced by our code MADGOLEM [37].

Fig. 3.9 shows the 95% C.L. upper limits on the sgluon pair production cross sections  $\times$  branching ratio to gluon pair as a function of the sgluon mass. The theoretical prediction for the sgluon pair production at NLO in the plot was produced by our code MADGOLEM [37].

Taking the cross section limit with the NLO calculation (blue line), sgluons with masses from 150 - 287 GeV (316 GeV expected) are excluded at the 95% C.L. by the ATLAS experiment with the data from 2011.



## Chapter 4

# SUSY monojet signatures

The main discovery channels for supersymmetry at the LHC are mediated by strong interactions, these are  $pp \rightarrow \tilde{q}\tilde{q}; \tilde{q}\tilde{q}^*; \tilde{q}\tilde{g}; \tilde{g}\tilde{g}$ , which we will analyze in detail in the Chapter 5. Also the sgluon pair production  $pp \rightarrow GG^*$  discussed in the Chapter 3 could reveal a signature of an underlying (non-minimal) realization of SUSY. The main limitation of these production modes is that it will be hard to extract any model parameters beyond the new particle masses. Nevertheless, mass measurements alone would not provide enough evidence for a SUSY interpretation. Therefore it is also important to study production modes involving the new physics weakly interacting sector, accessing thereby some information about the SUSY breaking pattern realized in this model.

In SUSY the simplest channels to access the new physics electroweak sector are the associated production of a colored particle and a weak gaugino: gluino [47] or a squark with chargino or neutralino. With these processes, apart from measuring the final state masses, it is also possible to extract information about the gaugino couplings [48].

Among these channels the squark-neutralino production,  $pp \rightarrow \tilde{q}\tilde{\chi}_1^0$ , provides some additional interesting features, *e.g.* its phenomenological signature is monojet+ $\cancel{E}_T$ , since  $\tilde{q} \rightarrow q\tilde{\chi}_1^0$ . This is a striking signature for Beyond SM physics. In this chapter we will study for the first time in the literature the production of neutralinos in association with squarks  $pp \rightarrow \tilde{q}\tilde{\chi}_1^0$ . Throughout our analysis we will: 1) Show the structure of the NLO QCD corrections; 2) Present a scan in the Minimal Supersymmetric Standard Model (MSSM) parameter space depicting the main differences from point to point; 3) Present a comparison between the NLO transverse momentum distributions and the multi-jet merging. In this manner we intend to help upgrading the analysis of this channel to the NLO QCD level, benefitting from a strongly reduced theoretical uncertainty. The results presented on this chapter are based on the publication [36].

### 4.1 Leading order production

Squark-gaugino associated production is a semi-weak process  $\mathcal{O}(\alpha_{EW}\alpha_s)$ , therefore it is expected to naturally provide a smaller rate when compared to channels mediated by strong

interactions only  $\mathcal{O}(\alpha_s^2)$ . Despite this fact, this production mode has a smaller phase-space suppression than the strong interaction processes, since  $m_{\tilde{\chi}_1^0} \ll m_{\tilde{q}}, m_{\tilde{g}}$ . This is valid because the lightest neutralino,  $\tilde{\chi}_1^0$ , usually corresponds to the dark matter candidate in most Supersymmetric scenarios.

At the leading order there is only one channel for squark neutralino production

$$qg \rightarrow \tilde{q}\tilde{\chi}_1^0, \quad (4.1)$$

with the corresponding Feynman diagrams shown in Fig. 4.1. From these diagrams we observe

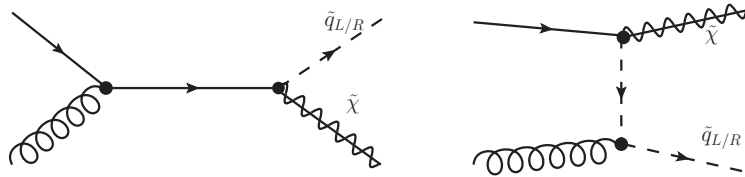


Figure 4.1: Feynman diagrams for the associated squark-gaugino production to LO.

some features that appear at leading order which are important to be highlighted:

- This is a flavor locked process, *i.e.* if this process starts with the initial-state quark  $u$  the final-state will have the squark  $\tilde{u}$ .
- Beyond the QCD vertices  $q$ - $q$ - $g$  or  $\tilde{q}$ - $\tilde{q}$ - $g$ , this process is driven also by the SUSY-electroweak interaction vertex  $q$ - $\tilde{q}$ - $\tilde{\chi}$ . As we adhere to first and second generation squarks and do not entertain the possibility of squark mixing, these couplings remain diagonal in flavor space.

It is worth mentioning that, within the assumption that the lightest neutralino  $\tilde{\chi}_1^0$  is the dark matter candidate, the knowledge of its coupling  $g_{q\tilde{q}\tilde{\chi}_1^0}$  is a fundamental ingredient to predict its thermal relic density in the universe. For instance, in the study of dark matter annihilation described by the Feynman diagram of Fig. 4.2 (a). Another fundamental process in which this coupling appears is in the study of dark matter direct detection experiments, where the nuclear recoil would occur via a t-channel squark exchange, Fig. 4.2 (b).

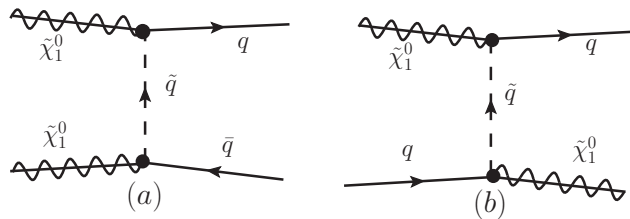


Figure 4.2: Leading order Feynman diagrams to the (a) dark matter annihilation and (b) dark matter direct detection, involving the lightest neutralino  $\tilde{\chi}_1^0$  as a dark matter candidate. Observe that at LO for both process we have  $\sigma \sim g_{q\tilde{q}\tilde{\chi}_1^0}^2$ .

A recent analysis proposing to extract this coupling at the LHC via the process  $pp \rightarrow \tilde{q}\tilde{\chi}_1^0$  was carried out at LO and can be found in Ref. [48]. Given the importance of this process it is also crucial to provide the production rate with a small theoretical uncertainty. Therefore it is important to calculate it within the NLO precision.

## 4.2 Real and virtual corrections

The NLO contributions to this production process appear at order  $\mathcal{O}(\alpha_{EW}\alpha_s^2)$ . The real emission contributions can arise from gluon and quark radiation. Depending on the squark-gluino and squark-neutralino mass hierarchy, the latter may induce on shell squark or gluino decays. A sample of these Feynman diagrams are depicted in Fig. 4.3.

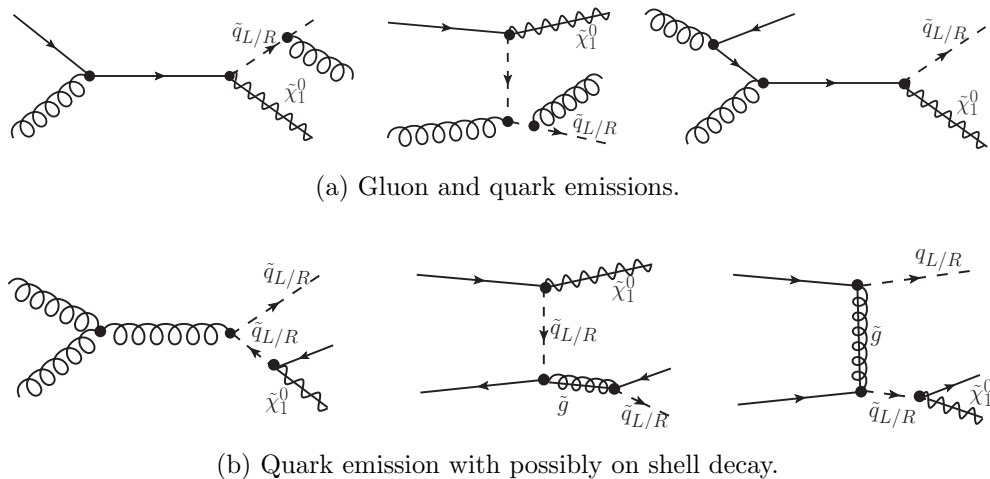


Figure 4.3: Sample Feynman diagrams for real emission corrections to squark-neutralino production.

For the gluon emission, Fig. 4.3a we observe the appearance of the splitting  $\tilde{q} \rightarrow \tilde{q}g$ . This type of radiation leads to a novel type of IR singularity not present in the SM, which occurs via the diagonal emission of soft gluons from squarks. To cope with this new divergent structure we introduce into MADGOLEM the respective Catani-Seymour dipoles. In Appendix A we present these Catani-Seymour SUSY dipoles including the FKS-style phase-space cutoff  $0 < \alpha \leq 1$  [42]. While the dipole subtraction always covers the soft and collinearly divergent phase-space regions, in terms of a variable parameter  $\alpha$  they can be defined extending more ( $\alpha = 1$ ) or less ( $\alpha \ll 1$ ) into the non-divergent phase-space regime; for more details see Appendix A.

Another special feature concerning the real emission diagrams appears when integrating in phase-space the on shell contributions arising from the diagrams of Fig. 4.3b. This integration can lead to double counting. For instance, let us consider the first diagram. In the case of  $m_{\tilde{q}} > m_{\tilde{\chi}_1^0}$  this will render two types of contributions depending on whether we consider off

shell and on shell squark decays:

$$\begin{aligned}
 gg &\rightarrow \tilde{q}(\tilde{q}^*)^{(*)} \rightarrow \tilde{q}\tilde{\chi}_1^0\bar{q} && \text{squark-neutralino production} \\
 gg &\rightarrow \tilde{q}\tilde{q}^* \rightarrow \tilde{q}\tilde{\chi}_1^0\bar{q} && \text{squark anti-squark production.}
 \end{aligned}
 \tag{4.2}$$

The first accounts for part of the real emission corrections of the squark-neutralino production. However the second is already taken into account when calculating the squark anti-squark production at LO, followed by the decay of the squark on its mass shell to the final state  $\tilde{\chi}_1^0\bar{q}$ . In order to avoid this double counting we subtract all on shell contributions. This is done by means of the ‘‘On Shell Subtraction Method’’ in the PROSPINO scheme. For more details see Sec. 2.5.

The virtual corrections to  $pp \rightarrow \tilde{q}\tilde{\chi}_1^0$  arise from self-energy corrections, vertex corrections and box diagrams. Beyond the pure QCD (gluon mediated) effects we also include the SUSY-QCD (gluino mediated) corrections. We show a sample of these Feynman diagrams in Fig. 4.4.

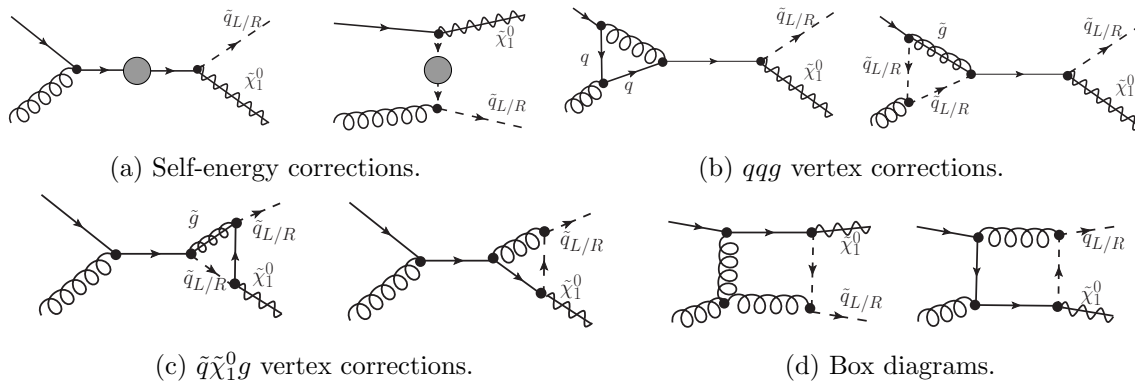


Figure 4.4: Sample Feynman diagrams for virtual corrections to squark-neutralino production.

## Numerical analysis

In our numerical analysis we use the CTEQ6L1 and CTEQ6M parton densities with five flavors [40], for respectively the LO and the NLO contributions. For the strong coupling we consistently rely on the corresponding  $\alpha_s(\mu_R)$ . We compute its value using two-loop running from  $\Lambda_{\text{QCD}}$  to the required renormalization scale, again with five active flavors. For the central renormalization and factorization scales we use the average final state masses  $\mu_R^0 = \mu_F^0 = (m_{\tilde{q}} + m_{\tilde{\chi}})/2$ , which has been shown to lead to stable perturbative results [23, 24].

Given the current LHC bounds on squark and gluino production [49] we modified the standard SPS1a point [50] to SPS1a<sub>1000</sub> increasing the gluino mass to 1 TeV, thus being more consistent with the recent bounds. This modification will only have an impact on the loop corrections for  $pp \rightarrow \tilde{q}\tilde{\chi}_1^0$ , since the gluinos do not appear at LO. Moreover, as we will discuss further down, the influence of the gluino mass is certainly meager.

In Tab. 4.1 we present the individual production rates and corresponding  $K$  factors for the different squark-neutralino channels involving first and second generation squarks and for each of the squark chiralities separately. The main contributions for this process appear from the  $\tilde{u}$  and  $\tilde{d}$  in the final state. This is due to the flavor-locked nature of the LO process, where the valence quarks  $u$  and  $d$  in the initial state lead to major contributions from high parton luminosities. The second generation gives just a sub-leading contribution to the total rate of around 5%, as will be shown, it is within the NLO scale uncertainty.

$\sqrt{S}$ [TeV]		$\sigma^{\text{LO}}$ [fb]	$\sigma^{\text{NLO}}$ [fb]	$K$		$\sigma^{\text{LO}}$ [fb]	$\sigma^{\text{NLO}}$ [fb]	$K$	$m_{\tilde{q}_R}$ [GeV]	$m_{\tilde{q}_L}$ [GeV]
7	$\tilde{u}_R \tilde{\chi}_1^0$	29.62	42.17	1.42	$\tilde{u}_L \tilde{\chi}_1^0$	0.83	1.26	1.52	549	561
14		176.36	245.74	1.39		5.03	7.52	1.49		
7	$\tilde{d}_R \tilde{\chi}_1^0$	3.61	5.31	1.47	$\tilde{d}_L \tilde{\chi}_1^0$	1.21	1.77	1.46	545	568
14		24.89	35.50	1.43		8.67	12.37	1.43		
7	$\tilde{c}_R \tilde{\chi}_1^0$	1.12	1.81	1.61	$\tilde{c}_L \tilde{\chi}_1^0$	0.03	0.06	2.00	549	561
14		13.69	20.69	1.51		0.38	0.66	1.70		
7	$\tilde{s}_R \tilde{\chi}_1^0$	0.57	0.78	1.38	$\tilde{s}_L \tilde{\chi}_1^0$	0.19	0.29	1.56	545	568
14		5.86	8.45	1.44		2.00	2.98	1.49		
7	$\sum \tilde{q}_R \tilde{\chi}_1^0$	34.92	50.07	1.43	$\sum \tilde{q}_L \tilde{\chi}_1^0$	2.26	3.38	1.50		
14		220.80	310.38	1.41		16.08	23.53	1.46		

Table 4.1: Individual production rates  $\sigma(pp \rightarrow \tilde{q}\tilde{\chi}_1^0)$  and corresponding  $K$  factors for the modified SPS1a<sub>1000</sub> scenario. The first and second generation squark masses happen to be degenerate. The scales are set to their central values  $\mu_R^0 = \mu_F^0 = (m_{\tilde{q}} + m_{\tilde{\chi}_1^0})/2$ . In the last line we show the sum of all contributions. We quote the relevant squark masses in the right columns.

In Fig. 4.5 we present the LO and NLO cross sections as functions of the squark mass  $m_{\tilde{u}_R}$ . We vary in parallel all squark masses, so that the original mass splitting  $m_{\tilde{u}_L} - m_{\tilde{u}_R}$  is kept constant. The bulk of the quantum effects arises from the virtual corrections, which largely dominate over the real emission corrections. In order to correctly interpret this observation we should point out that real and virtual corrections are separated by means of Catani-Seymour dipoles for  $\alpha = 1$ . As discussed in Appendix A, however, when changing this parameter to smaller values we shuffle part of the virtual contribution to the real part since the dipole subtraction term covers a smaller phase-space range. It is important to remember that despite this shuffling between real and virtual corrections the total rate is independent on the unphysical  $\alpha$  parameter.

The relative size of the NLO corrections is shown to be mostly independent on the squark mass leading to a correction of order  $K \simeq 1.4$  for squark mass in the range  $300 \text{ GeV} < m_{\tilde{u}_R} < 900 \text{ GeV}$ . At variance notice that, for the same mass range, the total LO and NLO rates nail down by two orders of magnitude due to phase-space suppression. In order to understand the source of the NLO corrections and the reason for an almost constant  $K$  factor we present in the right panel of Fig. 4.5 the relative size of each contributions to the real and virtual parts. For the real corrections we present the results separately in terms of the different initial states. For the virtual corrections we present all the contributions from the different one-loop topologies in Fig. 4.4 except for the self-energy corrections, which lie below 1%.

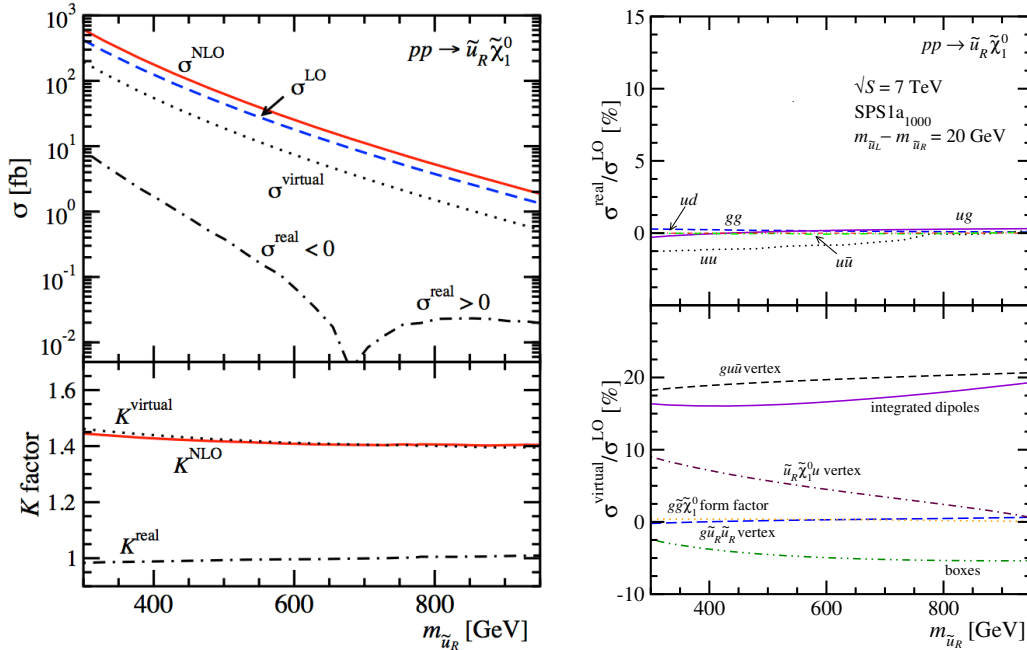


Figure 4.5: On the left panel we present the cross sections  $\sigma(pp \rightarrow \tilde{u}_R\tilde{\chi}_1^0)$  (top figure) and  $K$  factor (bottom figure) as a function of the squark masses, which we vary simultaneously, preserving a constant mass splitting  $m_{\tilde{u}_L} - m_{\tilde{u}_R} = 20$  GeV. For negative contributions to the total rate we show the absolute value  $|\sigma|$ . The remaining MSSM parameters are fixed to the SPS1a<sub>1000</sub> benchmark point. Real and virtual corrections are separated using the original Catani-Seymour dipoles [14] with  $\alpha = 1$ ; the integrated dipoles are included in the virtual corrections. On the right panel we show the relative size of each type of real and virtual corrections. Contributions from quark and squark self-energies lie below 1% and are not explicitly shown.

The bulk of the NLO corrections arises from the  $qqg$  vertex corrections and integrated dipoles, each of them leading to a 20% shift in the cross section. The corrections are mostly constant when changing the squark mass because their main contributions arise from pure QCD corrections. These involve the exchange of one virtual gluon (diagram on the left on Fig. 4.4b) while the SUSY-QCD ones (diagram on the right on Fig. 4.4b) are suppressed by the SUSY masses present in the loops. Thereby we observe that the vertex correction  $\tilde{q}\tilde{\chi}_1^0q$  decreases when increasing the squark mass. This happens because all the loop corrections are pure SUSY-QCD; they present at least one SUSY particle in the corresponding one-loop diagram, see Fig. 4.4c.

### 4.3 Scale dependence

In Fig 4.6 we analyze the dependence of the cross section as a function of the unphysical parameters, namely factorization and renormalization scales, when we move from LO to NLO. We observe the stabilization of the cross section when going to NLO. Unlike a Drell-Yan type

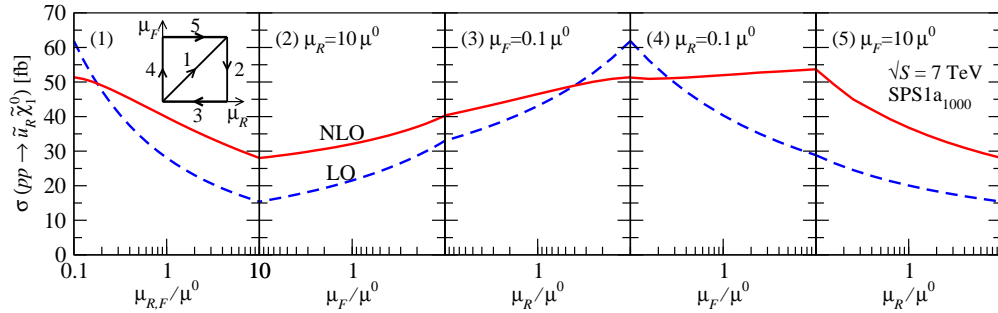


Figure 4.6: Profile of the renormalization and factorization scale dependence for  $pp \rightarrow \tilde{u}_R \tilde{\chi}_1^0$ . The plot traces the scale dependence following a contour in the  $\mu_R$ - $\mu_F$  plane covering  $\mu = (0.1 - 10)\mu^0$  as shown in the left panel. We assume our benchmark parameter choice and  $\sqrt{S} = 7$  TeV.

channel, in the current associated production process we have an explicit renormalization scale dependence at LO, as far as  $\sigma^{LO} \sim \alpha_s$ . But the  $\mu_R$  dependence does not dominate the scale dependence as in the QCD pair production,  $\sigma^{LO} \sim \alpha_s^2$ . This feature can be explicitly seen when comparing the scale dependence plot presented here with the sgluon pair production in Fig. 3.3.

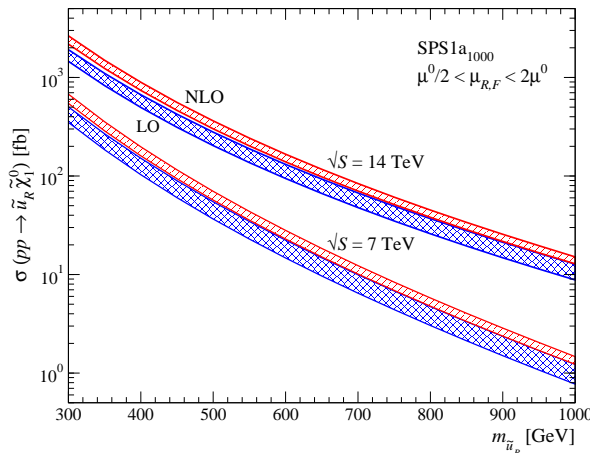


Figure 4.7: Total cross section for  $pp \rightarrow \tilde{u}_R \tilde{\chi}_1^0$  including the scale uncertainty as a function of the squark mass. The band corresponds to a scale variation  $\mu^0/2 < \mu_{R,F} < 2\mu^0$ . All the MSSM parameters we fix to the benchmark choice SPS1a<sub>1000</sub> and show results for  $\sqrt{S} = 7$  TeV and 14 TeV.

Finally, in Fig. 4.7 we show LO and NLO cross section for 7 and 14 TeV. The bands represent the scale dependence which is obtained for a simultaneous scale variation  $\mu^0/2 < \mu_{R,F} < 2\mu^0$ . The NLO uncertainty band shrinks down to  $\Delta\sigma/\sigma \lesssim 20\%$ , as opposed to the 70% level of the LO one. Comparing the two LHC energies we see that for 14 TeV the same number of signal events corresponds to an increase in the squark mass by at least 200 GeV. This gives an estimate on how much the discovery reach may increase when promoting the LHC to the high energy run.

## 4.4 MSSM parameter space

Given the enormous size of the parameter space present in the MSSM, it was defined a set of benchmark points, namely SPS points [50]. These represent several types of realizations of the MSSM involving different mass hierarchies, coupling constants and assume a different underlying SUSY-breaking mechanism. These points by no means cover the whole parameter space, however are very useful in order to understand the effects when changing the MSSM parameters.

In Tab. 4.2 we survey all the SPS points and compute the corresponding cross section and K-factor predictions for each of them. We observe that the total cross section strongly depends on each parameter space point. The reason is twofold:

- **Kinematics effect** – the different phase-space suppression in each case depending on the final-state masses.
- **Dynamics effect** – the strength of the coupling  $g_{q\tilde{q}\tilde{\chi}_1^0}$ , which changes substantially from one SPS point to another.

	$\sqrt{S}$ [TeV]	$\sigma^{\text{LO}}$ [fb]	$\sigma^{\text{NLO}}$ [fb]	$K$	$m_{\tilde{u}}$	$m_{\tilde{d}}$	$m_{\tilde{g}}$	$m_{\tilde{\chi}_1^0}$
SPS1a <sub>1000</sub>	7	35.27	50.44	1.43	$\tilde{u}_L : 561$	$\tilde{d}_L : 568$	1000	97
	14	215.02	301.27	1.40	$\tilde{u}_R : 549$	$\tilde{d}_R : 545$		
SPS1b	7	2.77	3.99	1.45	$\tilde{u}_L : 872$	$\tilde{d}_L : 878$	938	162
	14	27.21	37.46	1.38	$\tilde{u}_R : 850$	$\tilde{d}_R : 843$		
SPS2	7	0.04	0.07	1.52	$\tilde{u}_L : 1554$	$\tilde{d}_L : 1559$	782	123
	14	1.21	1.64	1.36	$\tilde{u}_R : 1554$	$\tilde{d}_R : 1552$		
SPS3	7	3.15	4.55	1.44	$\tilde{u}_L : 854$	$\tilde{d}_L : 860$	935	161
	14	30.20	41.59	1.38	$\tilde{u}_R : 832$	$\tilde{d}_R : 824$		
SPS4	7	6.44	9.04	1.40	$\tilde{u}_L : 760$	$\tilde{d}_L : 766$	733	120
	14	52.87	71.40	1.35	$\tilde{u}_R : 748$	$\tilde{d}_R : 743$		
SPS5	7	13.26	18.11	1.37	$\tilde{u}_L : 675$	$\tilde{d}_L : 678$	722	120
	14	95.81	132.29	1.38	$\tilde{u}_R : 657$	$\tilde{d}_R : 652$		
SPS6	7	9.84	14.06	1.43	$\tilde{u}_L : 670$	$\tilde{d}_L : 676$	720	190
	14	77.08	107.03	1.39	$\tilde{u}_R : 660$	$\tilde{d}_R : 650$		
SPS7	7	2.19	3.17	1.45	$\tilde{u}_L : 896$	$\tilde{d}_L : 904$	950	163
	14	22.36	30.80	1.38	$\tilde{u}_R : 875$	$\tilde{d}_R : 870$		
SPS8	7	0.65	0.95	1.45	$\tilde{u}_L : 1113$	$\tilde{d}_L : 1122$	839	139
	14	8.73	11.79	1.35	$\tilde{u}_R : 1077$	$\tilde{d}_R : 1072$		
SPS9	7	0.39	0.58	1.49	$\tilde{u}_L : 1276$	$\tilde{d}_L : 1279$	1872	187
	14	7.65	10.42	1.36	$\tilde{u}_R : 1282$	$\tilde{d}_R : 1289$		

Table 4.2: Summed cross section and corresponding  $K$  factors for all four first-generation squark processes  $pp \rightarrow \tilde{q}\tilde{\chi}_1^0$  in different SPS benchmark scenarios. The scales are chosen at  $\mu_{R,F}^0$ . All masses are given in GeV.

Instead, we should also notice that the corrections are largely insensitive to the specific SPS point remaining around  $K \sim 1.4$ . We already observed this feature at Fig. 5.8. As previously explained, the reason stems from the dominance of genuine QCD effects (gluon mediated), arising mostly from  $q\bar{q}g$  vertex correction and integrated dipoles. These effects are not high to any SUSY mass suppression, therefore the relative size barely depends on the SUSY mass spectrum.

## 4.5 Distributions: fixed order versus multi-jet merging

After our study of the total production rate at NLO for  $pp \rightarrow \tilde{q}\tilde{\chi}_1^0$  we also want to ensure that this picture includes improvements in the main distributions. We study quantitatively this via a comparison between the NLO distributions from MADGOLEM and the multi-jet merging computation. For the latter we use the MLM scheme [43] with up to two hard jets, as implemented in MADGRAPH5 [45] interfaced with PYTHIA [46]. We have confirmed that carrying out these simulation using up to one hard jet does not change these results within the numerical precision.

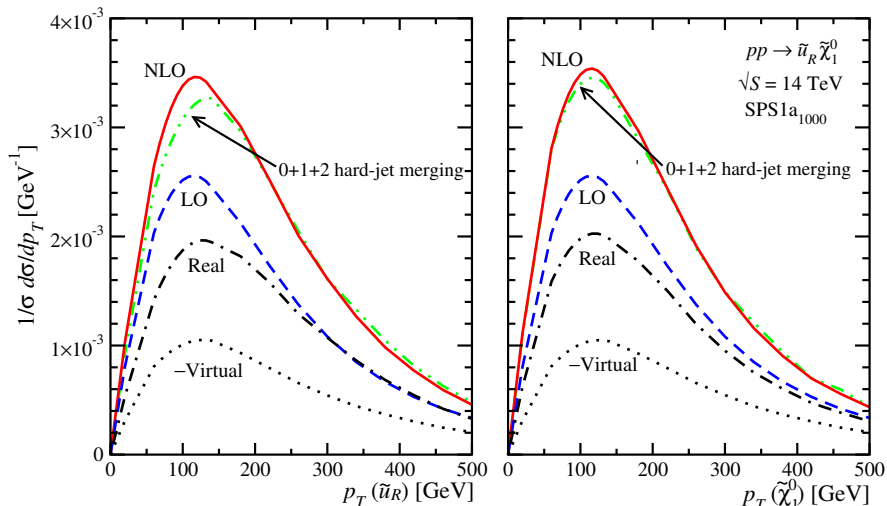


Figure 4.8: Squark and neutralino  $p_T$  distributions at the LHC ( $\sqrt{S} = 14$  TeV) for SPS1a<sub>1000</sub>. We compare the merged sample with the fixed order NLO computation. Both curves are normalized. We also show contributions to the NLO cross sections from the leading order, virtual and real parts. The latter are separated using the Catani-Seymour dipole with  $\alpha = 0.01$ .

In Fig. 4.8 we present the  $p_T$  distributions for the squarks and neutralinos at NLO and for multi-jet merging, both normalized to unit. We also present the LO, real and virtual contributions to the NLO distributions separately and shown to scale with respect to the former. We observe a fine agreement between the NLO and the merged distributions. There is a slightly harder  $p_T$  profile for the squarks in the merged approach. This change in profile is attributed to the additional recoil jets. This can be seen by the observation that the NLO

real corrections have a slightly harder profile which partially counter-balances the transverse momentum with the additional jet emission.

## 4.6 Squark-gaugino channels

Until now in this chapter, we have concentrated in the  $pp \rightarrow \tilde{q}\tilde{\chi}_1^0$  production. In this section we are interested in considering the LO and NLO rates for some other squark-gaugino channels, namely  $pp \rightarrow \tilde{q}\tilde{\chi}_1^0, \tilde{q}\tilde{\chi}_2^0, \tilde{q}\tilde{\chi}_1^\pm$ , this way including heavier neutralinos as well as charginos. These can lead to additional leptons in the signature from the decay of the charginos and the heavier neutralinos. For instance, with  $\tilde{\chi}_2^0$  in the final state we could have the following decay chain  $\tilde{\chi}_2^0 \rightarrow l^\pm \tilde{l}^\mp \rightarrow l^\pm l^\mp \tilde{\chi}_1^0$ .

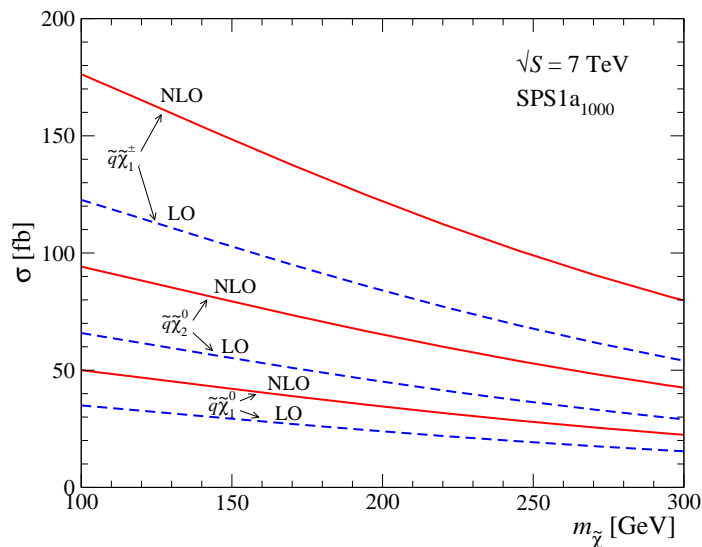


Figure 4.9: Cross sections for different squark and neutralino/chargino production channels,  $pp \rightarrow \tilde{q}\tilde{\chi}_1^0, \tilde{q}\tilde{\chi}_2^0, \tilde{q}\tilde{\chi}_1^\pm$ , as a function of the final-state neutralino/chargino mass. We show results for  $\sqrt{S} = 7 \text{ TeV}$  and the modified SPS1a scenario. As in Tab. 4.2 we sum over all first-generation squarks. The scales are fixed to  $\mu_{R,F}^0$ .

In Fig. 4.9 we show the LO and NLO total rate for squark with neutralino or chargino production as a function of the gaugino mass. The differences in cross sections for the explored channels can be traced back to their differences in strength for the coupling  $g_{q\tilde{q}\tilde{\chi}}$ . For example, the total rate for production of  $\tilde{q}\tilde{\chi}_1^0$  is roughly four times smaller than the  $\tilde{q}\tilde{\chi}_2^0$  mostly because of the relative strength  $(g_{q\tilde{q}\tilde{\chi}_2^0})/g_{q\tilde{q}\tilde{\chi}_1^0} \sim 1.8$ .

## Chapter 5

# Squark and gluino pair production to Next-to-Leading Order

NLO QCD corrections to squark and gluino production were first computed more than 10 years ago [17–19] and made public in the PROSPINO package [20]<sup>1</sup>. They have been proven to be essential for improved total rate predictions, substantially reducing the theoretical uncertainties from  $\mathcal{O}(100\%)$  at LO down to  $\mathcal{O}(20\%)$  at NLO.

In this chapter we will present an improved, brought-to-date analysis of the squark and gluino production, focusing in their NLO QCD effects. Using the MADGOLEM package we go beyond the former analyses, since in our framework no restriction assumptions on the supersymmetric mass spectra are needed. Moreover the code can also provide a study at the distribution level. In addition, benefitting from the automatic, fully flexible generation of the processes, as well as of the analytical Feynman-diagrammatic approach, we can single out specific elements of the QCD quantum corrections leading to a better understanding of the NLO contributions. For instance, we can consider the contributions arising from different partonic sub-channels, or separate the different one-loop topologies.

Particular emphasis we devote to illustrating the reduction of the theoretical uncertainties in total rates and kinematic distributions as a key improvement of NLO predictions. We conduct a comprehensive comparison of the fixed order differential cross sections with those obtained by multi-jet matrix element merging, including a variation of the renormalization and factorization scales. To conclude, we perform an analysis in terms of total rates and distributions, in which we check the numerical implications of the usual simplifying assumptions taken in the hitherto available NLO predictions for these major SUSY-pair processes, in special, that of assuming a mass-degenerate squark spectrum. The results presented in this chapter are based on the publication [38].

---

<sup>1</sup>As highlighted in Sec. 2.8, all the presented results have been checked to agree with PROSPINO2 wherever applicable.

## 5.1 Rates

In this section we start by performing a scan in the MSSM parameter space at the LHC involving all the pairs of squarks and gluinos in the final state:

$$pp \rightarrow \tilde{q}\tilde{q}, \tilde{q}\tilde{q}^*, \tilde{g}\tilde{g}, \tilde{g}\tilde{g}. \quad (5.1)$$

Following the typical decay signature we focus on the dominant first and second generation squarks  $\tilde{q} = \tilde{u}_{L,R}, \tilde{d}_{L,R}, \tilde{s}_{L,R}, \tilde{c}_{L,R}$  (where we do not consider flavor-mixing, *i.e.* the SUSY-QCD couplings are flavor-diagonal).

In our numerical analysis we use the CTEQ6L1 and CTEQ6M parton densities with five active flavors [40]. Unless stated otherwise, both the central renormalization and factorization scales we fix at the average final-state mass  $\mu_R = \mu_F \equiv \mu^0 = (m_1 + m_2)/2$ . From previous studies, this choice is known to lead perturbatively stable results [17–19]. The strong coupling constant  $\alpha_s(\mu_R)$  we compute accordingly. For this we use two-loop running from  $\Lambda_{\text{QCD}}$  to the required renormalization scale, within the five active flavor scheme. When applicable, the symmetry factor 1/2 stemming from the presence of two identical particles in the final state, *viz.* a pair of gluinos or of same-sign squarks with equal chirality and flavor, is introduced automatically.

The NLO corrections to these processes arise at order  $\mathcal{O}(\alpha_s^3)$ . The virtual corrections include the one-loop exchange of virtual gluons and gluinos. The standard 't Hooft-Feynman gauge is employed for internal gluons to avoid higher rank loop integrals. Accordingly, Fadeev-Popov ghosts appear in the gluon self-energy and in the three-gluon vertex corrections. Ultra-violet divergences are cancelled by renormalizing the strong coupling constant and all masses. Supersymmetry identifies the strong gauge coupling constant  $g_s$  and the Yukawa coupling of the quark–squark–gluino interaction,  $\hat{g}_s$ . At the one-loop level dimensional regularization induces an explicit breaking of this symmetry via the mismatch between the 2 fermionic gluino components and the  $(2 - 2\epsilon)$  degrees of freedom of the transverse gluon field. We restore the underlying supersymmetry with an appropriate finite counter term [19, 51]. Details on the renormalization procedure can be found in Appendix B.2.

The real emission contributions arise from gluon and quark radiation. The associated infrared divergences we subtract using Catani-Seymour dipoles, generalized to include the massive colored SUSY particles (*cf.* Ref [14] and our representation in the Appendix A of this thesis). Their respective dipoles are provided in our code, which includes the FKS-like phase space cutoff  $\alpha$  [42]. The soft and collinearly divergent phase space regions covered by the dipole subtraction we can select to extend more ( $\alpha = 1$ ) or less ( $\alpha \ll 1$ ) into the non-divergent phase space by changing this cutoff  $\alpha$ , for more details see Appendix A. Still concerning the real emission, on shell intermediate states can lead to double-counting which need to be subtracted. For instance, the real corrections for the squark–antisquark production depicted on Fig. 5.1 can lead to on shell gluino decays if  $m_{\tilde{q}} < m_{\tilde{g}}$  and these contributions can lead to a double-counting when studied alongside with the associated production of

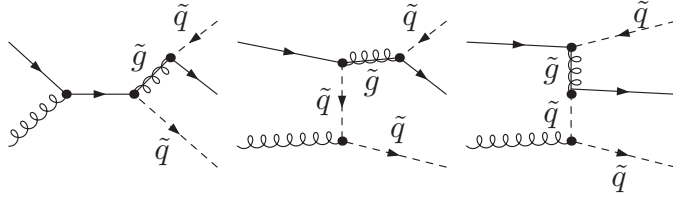


Figure 5.1: Sample Feynman diagrams for real emission corrections to squark–antisquark production, the first two diagrams illustrate situations that may lead to an on-shell decay of a gluino, whereas the third one describes a typical non-resonant contribution.

squark-gluino pairs. In fact we can separate them into two different types of contributions

$$\begin{aligned}
 qg &\rightarrow \tilde{q}(\tilde{g})^* \rightarrow \tilde{q}\tilde{q}^*q && \text{squark–antisquark production} \\
 qg &\rightarrow \tilde{q}\tilde{g} \rightarrow \tilde{q}\tilde{q}^*q && \text{squark–gluino production ,}
 \end{aligned}
 \tag{5.2}$$

and subtract the pure squark–gluino part in which the on-shell gluino decays promptly into a quark-squark pairs, from the squark–antisquark production by an off-shell gluino intermediate state  $\tilde{g}^*$ , and which indeed constitutes part of the genuine real correction to the squark-antisquark production to NLO. Following the PROSPINO scheme, MADGOLEM removes automatically all the on-shell configurations locally through a point-by-point subtraction over the entire phase space. For more details see Sec. 2.5.

### 5.1.1 Parameter space

	$m_{\tilde{u}_L}$	$m_{\tilde{u}_R}$	$m_{\tilde{d}_L}$	$m_{\tilde{d}_R}$	$m_{\tilde{g}}$	mass hierarchy
CMSSM 10.2.2	1162	1120	1165	1116	1255	$\tilde{q}_R < \tilde{q}_L < \tilde{g}$
CMSSM 40.2.2	1200	1168	1202	1165	1170	$\tilde{q}_R < \tilde{g} < \tilde{q}_L$
CMSSM 40.3.2	1299	1284	1301	1284	932	$\tilde{g} < \tilde{q}_R < \tilde{q}_L$
mGMSB 1.2	899	868	902	867	946	$\tilde{q}_R < \tilde{q}_L < \tilde{g}$
mGMSB 2.1.2	933	897	936	895	786	$\tilde{g} < \tilde{q}_R < \tilde{q}_L$
mAMSB 1.3	1274	1280	1276	1289	1282	$\tilde{u}_L < \tilde{u}_R < \tilde{g}, \tilde{d}_L < \tilde{g} < \tilde{d}_R$

Table 5.1: Squark and gluino masses (in GeV) for different benchmark points, by which we profile the trademark MSSM phenomenology.

In this section we perform a scan in the MSSM parameter space for LHC center-of-mass energy of  $\sqrt{S} = 14$  TeV. We choose new benchmark points in agreement with the current LHC constraints [52]. In Tab. 5.1 we list these benchmark points and explicitly show their mass hierarchy and in Tab. 5.2 we present the corresponding results for the predicted total rates to LO and NLO. Using the general MADGOLEM setup it is possible to separate the squark flavor and chirality in squark pair production and in associated squark–gluino production. The size of the NLO QCD effects we express through the consistent ratio  $K \equiv \sigma^{\text{NLO}}/\sigma^{\text{LO}}$ .

	$\tilde{u}_L\tilde{u}_L$			$\tilde{u}_R\tilde{u}_R$			$\tilde{u}_L\tilde{u}_R$			$\tilde{u}\tilde{d}$					
	$\sigma^{\text{LO}}$	$\sigma^{\text{NLO}}$	$K$	$\sigma^{\text{LO}}$	$\sigma^{\text{NLO}}$	$K$	$\sigma^{\text{LO}}$	$\sigma^{\text{NLO}}$	$K$	$\sigma^{\text{LO}}$	$\sigma^{\text{NLO}}$	$K$			
CMSSM 10.2.2	26.2	29.2	1.11	31.0	34.3	1.11	26.2	30.7	1.17	87.7	104.8	1.19			
CMSSM 40.2.2	22.8	26.0	1.14	26.0	29.4	1.13	25.2	30.2	1.20	75.2	91.2	1.21			
CMSSM 40.3.2	14.8	18.1	1.22	15.8	19.1	1.21	23.1	29.9	1.29	49.8	63.6	1.28			
mGMSB 1.2	85.3	97.0	1.14	98.1	110.7	1.13	99.7	120.4	1.21	316.6	387.8	1.22			
mGMSB 2.1.2	73.9	88.7	1.20	87.6	104.5	1.19	113.9	144.5	1.27	293.3	372.6	1.27			
mAMSB 1.3	16.8	18.9	1.13	16.4	18.4	1.12	16.1	19.1	1.19	48.3	58.1	1.20			
	$\tilde{u}_L\tilde{u}_L^*$			$\tilde{u}_R\tilde{u}_R^*$			$\tilde{u}_L\tilde{u}_R^*, \tilde{u}_R\tilde{u}_L^*$			$\tilde{u}\tilde{d}^*$					
	$\sigma^{\text{LO}}$	$\sigma^{\text{NLO}}$	$K$	$\sigma^{\text{LO}}$	$\sigma^{\text{NLO}}$	$K$	$\sigma^{\text{LO}}$	$\sigma^{\text{NLO}}$	$K$	$\sigma^{\text{LO}}$	$\sigma^{\text{NLO}}$	$K$			
CMSSM 10.2.2	3.0	4.6	1.54	3.8	5.8	1.53	4.6	6.0	1.30	16.0	19.3	1.21			
CMSSM 40.2.2	2.5	3.8	1.49	3.0	4.6	1.53	3.7	4.9	1.32	13.1	15.8	1.21			
CMSSM 40.3.2	1.7	2.5	1.44	1.9	2.7	1.44	1.9	2.6	1.33	7.7	9.3	1.20			
mGMSB 1.2	17.8	27.5	1.54	21.9	33.7	1.54	21.1	27.8	1.32	74.1	92.8	1.25			
mGMSB 2.1.2	16.0	23.0	1.44	20.2	29.2	1.45	17.1	22.5	1.32	66.0	81.6	1.24			
mAMSB 1.3	1.6	2.4	1.54	1.5	2.3	1.53	2.2	3.0	1.32	7.7	9.2	1.20			
	$\tilde{u}_L\tilde{g}$			$\tilde{u}_R\tilde{g}$			$\tilde{u}_L^*\tilde{g}$			$\tilde{d}\tilde{g}$			$\tilde{g}\tilde{g}$		
	$\sigma^{\text{LO}}$	$\sigma^{\text{NLO}}$	$K$	$\sigma^{\text{LO}}$	$\sigma^{\text{NLO}}$	$K$	$\sigma^{\text{LO}}$	$\sigma^{\text{NLO}}$	$K$	$\sigma^{\text{LO}}$	$\sigma^{\text{NLO}}$	$K$	$\sigma^{\text{LO}}$	$\sigma^{\text{NLO}}$	$K$
CMSSM 10.2.2	78.7	108.6	1.38	87.7	120.3	1.37	2.3	3.8	1.63	58.2	83.6	1.44	23.3	53.4	2.29
CMSSM 40.2.2	93.5	131.3	1.40	101.7	142.3	1.40	2.8	4.6	1.65	68.7	100.5	1.46	41.1	94.5	2.30
CMSSM 40.3.2	159.4	239.5	1.50	165.6	248.2	1.50	5.2	9.0	1.73	116.3	182.0	1.57	249.2	552.9	2.22
mGMSB 1.2	467.0	610.6	1.31	511.4	665.4	1.30	18.7	28.3	1.52	371.2	503.3	1.36	222.8	453.4	2.03
mGMSB 2.1.2	777.0	1077.6	1.39	868.0	1193.9	1.38	33.6	52.5	1.56	638.1	914.6	1.43	849.6	1755.0	2.07
mAMSB 1.3	54.4	78.1	1.44	53.5	77.0	1.44	1.5	2.6	1.71	36.3	54.5	1.50	19.0	46.1	2.42

Table 5.2: Total cross sections (in fb) and corresponding  $K$  factors for squark and gluino production at  $\sqrt{S} = 14$  TeV. The renormalization and factorization scales are chosen as the average final state mass. The notation  $\tilde{u}\tilde{d}$  indicates the summation over all possible final-state chiralities  $\tilde{u}\tilde{d} = \tilde{u}_L\tilde{d}_L + \tilde{u}_L\tilde{d}_R + \tilde{u}_R\tilde{d}_L + \tilde{u}_R\tilde{d}_R$ . Symmetry factors 1/2 are automatically included, when applicable.

Analogously to the results obtained from a similar analysis for the squark-neutralino process  $pp \rightarrow \tilde{q}\tilde{\chi}_1^0$  in Sec. 4.4, we observe that the total cross section strongly depends on the specific benchmark point that we consider. Here as the process is just driven by the strong coupling constant  $\alpha_s$  the main variations in the rates for different scenarios have a mere kinematical origin, and arise essentially from the different phase space suppression in each case depending on the final-state masses. We also observe that the  $K$  factors remain stable when comparing the different scenarios analyzed for the same process. This is so because the main corrections arise from pure QCD effects while the SUSY-QCD ones are mass suppressed. This fact we will study in more detail in the next sections. Let us also point out that the corresponding results for the lower nominal center-of-mass energy  $\sqrt{S} = 8$  TeV typically render smaller cross-sections (falling down by factor 10 – 50) and slightly larger  $K$  factors resulting from the different scaling behavior of the LO and NLO contributions convoluted with the pdfs, and also in part to a well-know poor perturbative behavior of the CTEQ parton densities at LO.

Lastly, the different color charges of squarks and gluinos as well as their spin are clearly reflected in the production rates. Interactions among color octets will give larger rates than color triplets. Similarly, fermion pairs yield larger cross sections than scalar pairs. This effect is not only observed in the LO and NLO rates but also in the relative  $K$  factor, namely the in the relative size of the QCD-induced quantum corrections.

### 5.1.2 Squark pair production

Squark pair production can lead to a multitude of final states, which we first classify into two basic categories:

1. squark–squark pairs  $\tilde{q}\tilde{q}$ , to leading order, as depicted in Fig. 5.3, are mediated by  $t$ -channel gluino interchange between colliding quarks. This mechanism is flavor-locked, so first generation squarks will dominate. In particular in proton-proton collisions at large parton- $x$  values this channel will contribute large cross sections because it links incoming valence quarks.

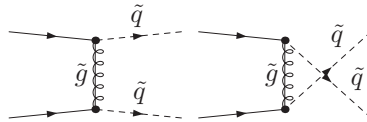


Figure 5.2: Sample Feynman diagrams for squark–squark production to LO.

2. squark–antisquark pairs  $\tilde{q}\tilde{q}^*$  with three distinct sub-channels:  $q\bar{q}$  annihilation through an  $s$ -channel gluon;  $q\bar{q}$  scattering via a  $t$ -channel gluino, and  $gg$  fusion with  $s$ -channel and  $t$ -channel diagrams. Due to the large adjoint color charge and the higher spin representations involved the  $gg$  initial-state dominates at the LHC up to moderate parton- $x$  values, while the quark-mediated partonic sub-channels become more relevant in the large  $x$  limit. In the absence of flavor mixing, the gluino-induced sub-channel is flavor-locked to the initial state while the other two are flavor-locked within the final state. First and second generation squarks will therefore contribute with similar rates, at variance with the (same sign) squark–squark production.

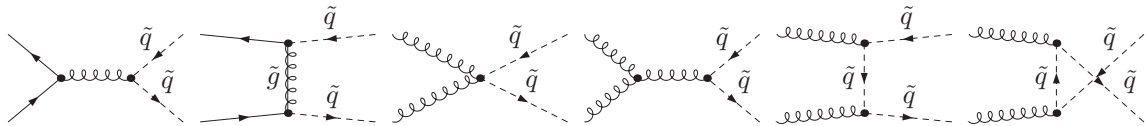


Figure 5.3: Sample Feynman diagrams for squark–antisquark production to LO.

The predicted LO and NLO rates alongside their  $K$  factors we document in Table 5.2. The production of squark pairs  $\tilde{q}\tilde{q}$  yields cross sections of 10 to 100 fb for squark and gluino masses around 1 TeV. The squark–antisquark rates for this mass range are roughly one order of magnitude smaller. These cross sections are highly sensitive to the strongly interacting superpartner masses. This is largely due to kinematics, *i.e.* the different squark masses in each benchmark point. For instance, the production of the lighter right-handed squarks comes with larger production rates than that of their left-handed counterparts. According to Tab. 4.2 this is true for all benchmark points except for mAMSB 1.3. This means that in a squark–(anti)squark sample right-handed squarks will be overrepresented. This can be a problem if the NLO computation does not keep track of the different masses of left-handed and right-handed quarks.

In contrast, we see that the  $K$  factors barely change between benchmark points, because the bulk of the NLO effects are genuine QCD effects. Notice that, all  $K$  factors range around  $K \sim 1.2$  for squark-squark production – correspondingly, for squark-antisquark production they render  $K \sim 1.2–1.5$  depending on the specific channel. Some sample Feynman diagrams depicting the NLO SUSY-QCD corrections we show in Fig. 5.4. The supersymmetric QCD corrections including one-loop squark and gluino loops are power-suppressed by the heavy particle masses.

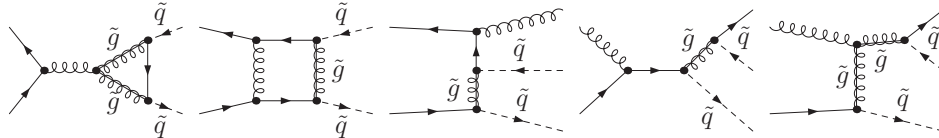


Figure 5.4: Sample Feynman diagrams for squark-antisquark production to NLO. Virtual corrections involve the exchange of gluons, gluinos and squarks. Real corrections denote the emission of one quark or gluon.

An interesting observation we make for squark pairs with different chiralities, *e.g.*  $\tilde{u}_L\tilde{u}_R$ . As mentioned above, all  $\tilde{q}\tilde{q}$  channels proceed via a  $t$ -channel gluino. For identical final-state chiralities, the gluino propagator corresponds to a mass insertion – enhancing the LO rates for heavy gluinos. This is not true for  $\tilde{u}_L\tilde{u}_R$  production, where we probe the  $\not{p}$  term in the gluino propagator (cf. the Feynman diagrams shown in Fig. 5.3). This difference can be read off Tab. 5.2. The  $\tilde{u}_L\tilde{u}_L$  and  $\tilde{u}_R\tilde{u}_R$  channels are suppressed from CMSSM 10.2.2 to CMSSM 40.3.2, following a decrease in the gluino mass. On the other hand, the  $\tilde{u}_L\tilde{u}_R$  rate remains quite constant. This different behavior is also visible from their  $K$  factors, which are ordered as  $K_{LL} \sim K_{RR} < K_{LR}$ .

In Fig. 5.5 we separate the real and virtual QCD and SUSY-QCD corrections for  $\tilde{u}_L\tilde{u}_L^*$  production as a function of the final state mass  $m_{\tilde{u}_L}$ . All the other heavy masses we vary simultaneously, keeping the absolute mass splittings of the CMSSM 10.2.2 benchmark point shown in Tab. 4.2. The two main partonic subprocesses contributing to the process we show separately. The separation into real and virtual corrections we define through Catani-Seymour dipoles with a FKS-like cutoff  $\alpha = 1$ . The integrated dipoles count towards the virtual corrections while only the hard gluon radiation counts towards the real corrections. This is the reason why the real corrections appear negligible. The cross sections for both the gluon fusion  $gg$  and the quark-antiquark  $q\bar{q}$  subprocesses are essentially determined by the squark masses and the corresponding phase space suppression. The gluon fusion dominates in the lower squark mass range, contributing with rates of roughly a factor 2 above the  $q\bar{q}$  mechanism. Conversely, the  $gg$  channel depletes slightly faster than the  $q\bar{q}$ , especially for large squark masses. This can be traced back to the respective scaling behavior of the cross sections [17] as a function of the partonic energy, and its correlation to the parton luminosities. As already mentioned, heavier final-states probe larger parton- $x$  values — this

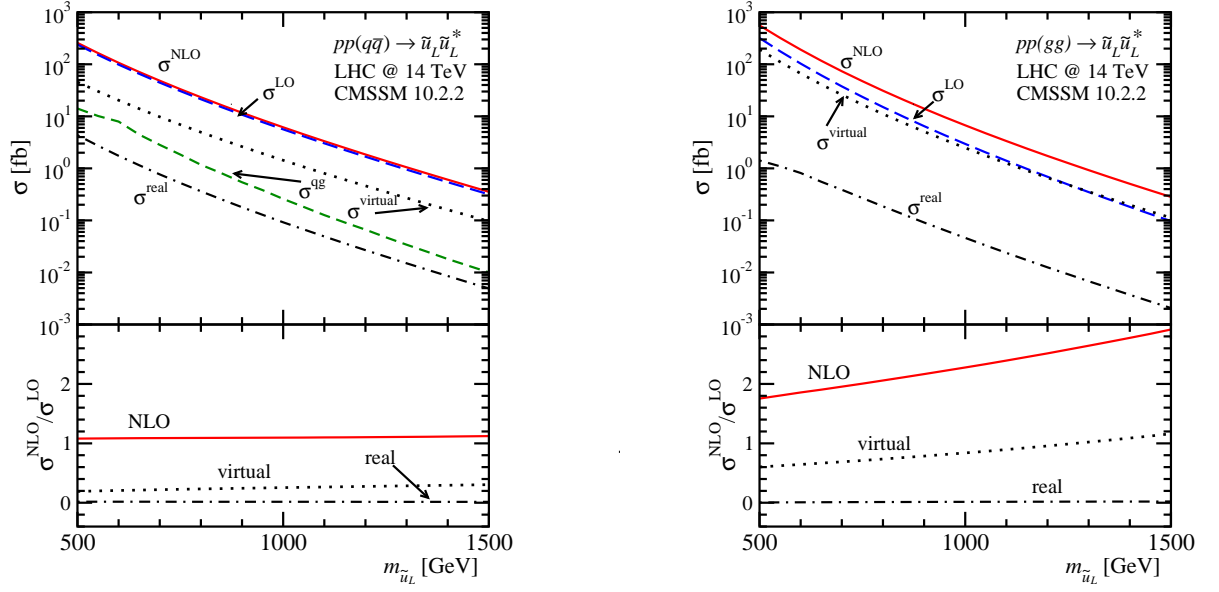


Figure 5.5: Cross sections for  $\tilde{u}_L \tilde{u}_L^*$  production for the different initial states as a function of the squark and the gluino masses. The  $q\bar{q}$  process (left) includes also the  $qg$  crossed-channels. Together with  $m_{\tilde{u}_L}$  we vary all squark and gluino masses such that the mass splittings of the CMSSM 10.2.2 benchmark point are kept. In the lower panels we evaluate the relative size of the NLO cross section with respect to the total LO rate for each sub-channel.

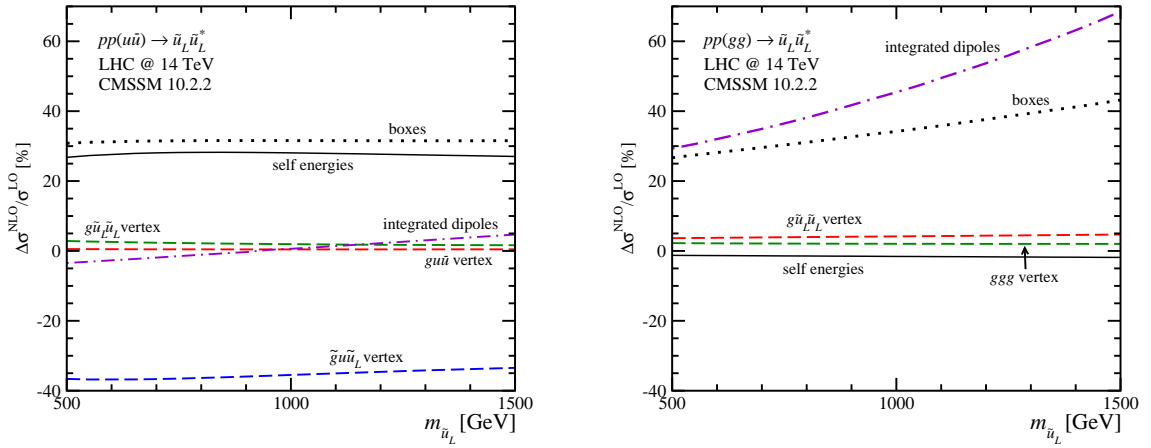


Figure 5.6: Relative shift  $\Delta\sigma^{\text{NLO}}/\sigma^{\text{LO}}$  for the different parts of the virtual corrections to  $q\bar{q}/gg \rightarrow \tilde{u}_L \tilde{u}_L^*$  production. All squark and gluino masses we vary in parallel, just like in Fig. 5.5.

being the region where the quark parton densities become more competitive, while the gluon luminosity depletes.

The lower panels of Fig. 5.5 show the relative size of the NLO contributions with respect to the total LO rate. While  $\sigma^{\text{virtual}}/\sigma^{\text{LO}}$  grows with increasing squark masses, specially for the  $gg$  initial state,  $\sigma^{\text{real}}/\sigma^{\text{LO}}$  stays constant. This effect is related to threshold enhancements: first, a long-range gluon exchange between slowly moving squarks in the  $gg \rightarrow \tilde{u}\tilde{u}^*$  channel gives rise to a Coulomb singularity  $\sigma \sim \pi\alpha_s/\beta$ , where  $\beta$  denotes the relative squark velocity in the center-of-mass frame,  $\beta \equiv \sqrt{1 - 4m_{\tilde{u}}^2/\hat{S}}$ . This is nothing but the well-known Sommerfeld enhancement [53]. The associated threshold singularity cancels the leading  $\sigma \sim \beta$  dependence from the phase space and leads to finite rates but divergent  $K$  factors [19]. In addition, there exists a logarithmic enhancement  $\sigma \sim [A \log^2(\beta) + B \log(8\beta^2)]$  from initial-state soft gluon radiation. This second effect is common to the  $gg$  and  $q\bar{q}$  initial states. Threshold effects can be re-summed to improve the precision of the cross section prediction [54].

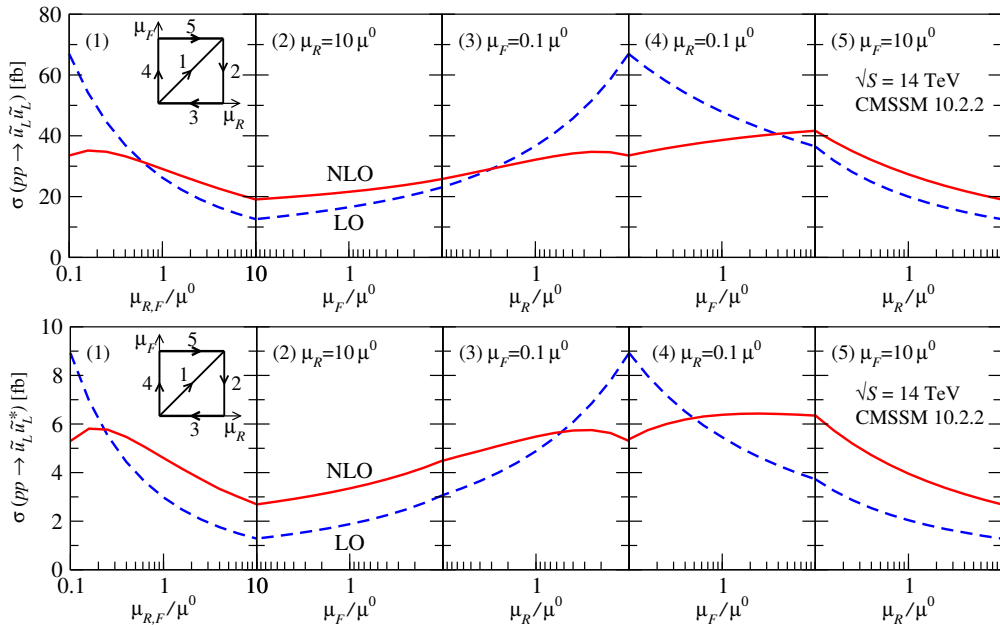


Figure 5.7: Renormalization and factorization scale dependence for squark pair production  $pp \rightarrow \tilde{u}_L \tilde{u}_L$  (upper) and  $pp \rightarrow \tilde{u}_L \tilde{u}_L^*$  (lower). The plots trace a contour in the  $\mu_R$ - $\mu_F$  plane in the range  $\mu = (0.1 - 10) \times \mu^0$  with  $\mu^0 = m_{\tilde{u}_L}$ . All MSSM parameters follow the CMSSM 10.2.2 benchmark point in Tab. 4.2.

The internal architecture of the virtual corrections we analyze in Fig. 5.6. Virtual diagrams come in different one-loop topologies: self-energy and wave-function corrections, three-point vertex corrections, and box corrections. The box diagrams also include the one-loop corrections to the quartic  $gg\tilde{q}\tilde{q}$  vertex. Again, we assume the specific flavor/chirality final state  $\tilde{u}_L \tilde{u}_L^*$  with the CMSSM 10.2.2 parameter point. Just like in Fig. 5.5 the masses vary in parallel, keeping the splitting constant. The threshold effects discussed in the previous paragraph are nicely visible in the increasing ratio  $\Delta\sigma^{\text{NLO}}/\sigma^{\text{LO}}$  for the boxes and the integrated dipoles, where the quantity  $\Delta\sigma^{\text{NLO}}/\sigma^{\text{NLO}}$  accounts for the genuine  $\mathcal{O}(\alpha_s)$  NLO contributions. This enhancement leads to sizable quantum effects in the 30% – 70% range for the  $gg$  initial

state.

For the  $q\bar{q}$ -initiated subprocess the integrated dipoles are numerically far smaller. The bulk of the virtual corrections is driven by the boxes, the gluino self-energy, and the negative quark–squark–gluino vertex correction. Their remarkable size we can trace back to mass insertions in the gluino-mediated diagrams, which can enhance the relative size of their contributions for large gluino masses, very much in the same way as we have encountered for the LO rates. Barring these dominant sources, Fig. 5.6 illustrates that all remaining NLO contributions stay at the  $\sim 5\%$  level or below. In the absence of threshold effects, all these pieces are insensitive to the squark mass. As a consequence, both the LO and the NLO cross sections undergo essentially the same phase space suppression as a function of the final state mass. Because we vary all masses in parallel this is also indicative of the dominance of the gluon-mediated QCD effects as compared to SUSY-QCD corrections. In the large-mass regime the latter have to be power suppressed, matching on to the decoupling regime.

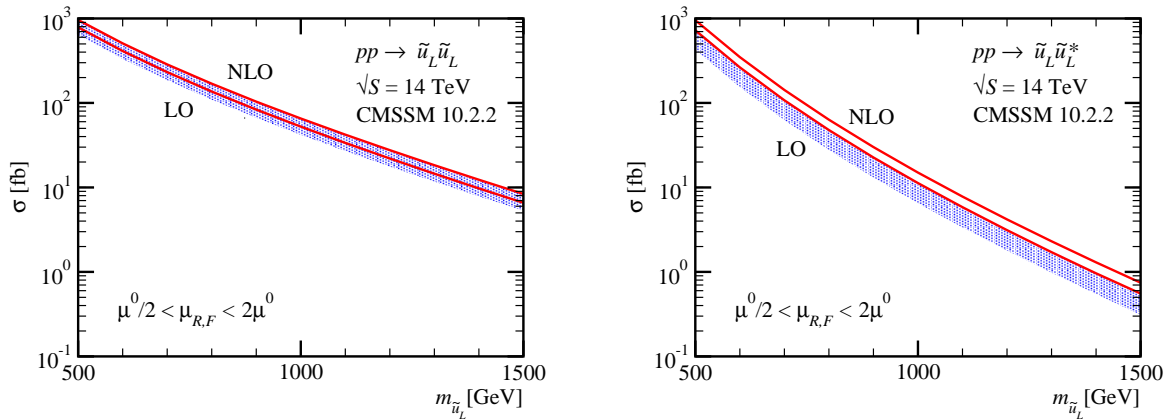


Figure 5.8: Cross sections  $\sigma(pp \rightarrow \tilde{u}_L \tilde{u}_L)$  (left) and  $\sigma(pp \rightarrow \tilde{u}_L \tilde{u}_L^*)$  (right) as a function of the squark mass. The band corresponds to the scale variation envelope  $\mu^0/2 < \mu_{R,F} < 2\mu^0$ , where  $\mu^0 = m_{\tilde{u}_L}$ . The central MSSM parameters are given by the CMSSM 10.2.2 benchmark point. The squark and gluino masses we vary in parallel, just like in Fig. 5.5.

The fact that cross section predictions increase, *i.e.* exclusion limits become stronger once we include NLO cross sections is only a superficial effect of the improved QCD predictions. The main reason for higher order calculations is the increased precision, reflected in the stabilization of the renormalization and factorization scale dependence. As is well known, these scale dependences do not have to be an accurate measure of the theoretical uncertainty. This can be seen for example in Drell-Yan-type processes at the LHC where the LO factorization scale dependence hugely undershoots the known NLO corrections. For the pair production of heavy states mediated by the strong interaction instead, the detailed studies of top pairs give us hope that the scale dependence can be used as a reasonable error estimate.

In Fig. 5.7 we trace the scale dependences of squark–squark and squark–antisquark production. Note that such a separate scale variation is not possible in PROSPINO, where both scales are identified in the analytic expressions. We profile the behavior of  $\sigma^{\text{LO}}(\mu)$  and

$\sigma^{\text{NLO}}(\mu)$  for an independent variation of the renormalization and the factorization scales in the range  $\mu^0/10 < \mu_{R,F} < 10\mu^0$ . As usual, the central scale choice is  $\mu^0 = m_{\tilde{u}_L}$ . The path across the  $\mu_R - \mu_F$  plane we illustrate in the little square in the left panel. The numerical results are again given for the CMSSM 10.2.2 parameter point and  $\sqrt{S} = 14$  TeV. As expected, due to  $\mathcal{O}(\alpha_s)$  dependence of the LO cross-sections, the renormalization scale dependence dominates the leading order scale dependence. Unlike in other cases there is no cancellation between the renormalization and the factorization scale dependences. The stabilization of the scale dependence manifests itself as smoother NLO slope. While the LO scale variation covers an  $\mathcal{O}(100\%)$  band, the improved NLO uncertainty is limited to  $\mathcal{O}(30\%)$ . Interestingly, the NLO plateau at small scales is not generated by a combination of the two scale dependences, but is visible for a variation of the renormalization scale alone at fixed small values of the factorization scale. This observation alone spells out again the dominant rule of the renormalization scale in determining the overall theoretical uncertainty.

In Fig. 5.8 we show the usual LO and NLO cross sections as a function of the final-state mass  $m_{\tilde{u}_L}$ . The error bar around the central values represents a simultaneous scale variation  $[\mu^0/2, 2\mu^0]$ . Both error bands nicely overlap and reflect, for  $\tilde{u}_L\tilde{u}_L$ , a reduction of the theoretical uncertainties from  $\mathcal{O}(50\%)$  at LO down to  $\mathcal{O}(20\%)$  at NLO – similarly, from  $\mathcal{O}(60\%)$  down to  $\mathcal{O}(30\%)$  for  $\tilde{u}_L\tilde{u}_L^*$ .

### 5.1.3 Squark–gluino production

The squark-gluino production has the important feature of being a flavor locked process at LO proceeding through just one channel

$$qg \rightarrow \tilde{q}\tilde{g}, \quad (5.3)$$

with the corresponding Feynman diagrams shown in Fig. 5.9. Bearing this in mind we can

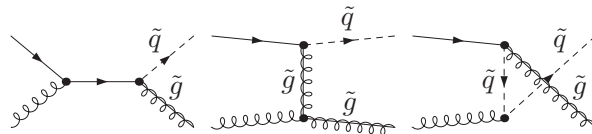


Figure 5.9: Feynman diagrams for the squark-gluino production at LO.

nicely explain several features shown in Tabs. 5.2. For instance, we see how  $\tilde{u}_L\tilde{g}$  production dominates over the charge conjugated channel  $\tilde{u}_L^*\tilde{g}$ , simply due to the valence  $u$  quark. This is also the reason why the QCD corrections are larger for the  $\tilde{u}_L^*\tilde{g}$  process, because  $gg$ -initiated NLO contributions are not suppressed by the relative size of the underlying parton luminosities.

In Fig. 5.10 we display the dependence of the total cross section  $\sigma(pp \rightarrow \tilde{u}_L\tilde{g})$  at LO and NLO as a function of the final state squark mass  $m_{\tilde{u}_L}$ , noting that the gluino mass is changed

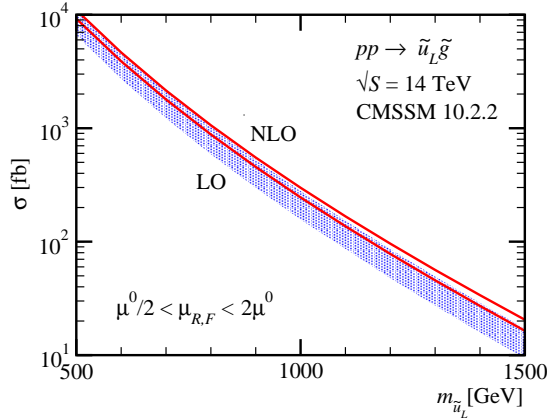


Figure 5.10: Cross sections for  $\sigma(pp \rightarrow \tilde{u}_L \tilde{g})$  as a function of the squark mass  $m_{\tilde{u}_L}$ . The band corresponds to a scale variation  $\mu^0/2 < \mu_{R,F} < 2\mu^0$ , where  $\mu^0 = (m_{\tilde{u}_L} + m_{\tilde{g}})/2$ . The MSSM parameters are given by the CMSSM 10.2.2 benchmark point. The squark and gluino masses we vary in parallel, just like in Fig. 5.5.

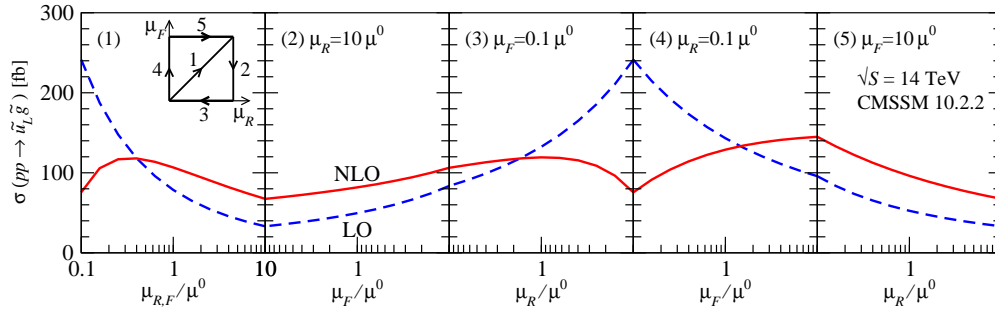


Figure 5.11: Renormalization and factorization scale dependence for  $\tilde{u}_L \tilde{g}$  associated production. The plot traces a contour in the  $\mu_R$ - $\mu_F$  plane in the range  $\mu = (0.1 - 10) \times \mu^0$  with  $\mu^0 = (m_{\tilde{u}_L} + m_{\tilde{g}})/2$ . All parameters are the same as for Fig. 5.7, with mass values  $m_{\tilde{u}_L} = 1162$  GeV and  $m_{\tilde{g}} = 1255$  GeV.

together with the squark mass. We observe that the cross section decreases three orders of magnitude by raising the squark mass from 500 up to 1500 GeV. By comparing the LO and NLO uncertainty bands we find that the scale uncertainties decrease from  $\Delta\sigma^{LO}/\sigma^{LO} \sim \mathcal{O}(60)\%$  down to  $\Delta\sigma^{NLO}/\sigma^{NLO} \sim \mathcal{O}(20)\%$ . A complementary viewpoint we provide in Fig. 5.11, where we probe scale variations of the total cross section as usually in the two-dimensional renormalization versus factorization scale plane. In this plot we explicitly see the stabilization of both scales when going from LO to NLO in a smoother profile of the latter one.

#### 5.1.4 Gluino pair production

Similar features we identify for the gluino pair production. In special, in Fig. 5.12 we observe again the same suppression in the total rate of 3 orders of magnitude when running the gluino

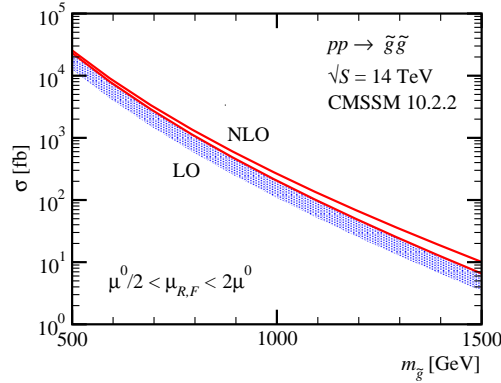


Figure 5.12: Cross sections for  $\sigma(pp \rightarrow \tilde{g}\tilde{g})$  as a function of the gluino mass  $m_{\tilde{g}}$ . The band corresponds to a scale variation  $\mu^0/2 < \mu_{R,F} < 2\mu^0$  with  $\mu^0 = m_{\tilde{g}}$ . The MSSM parameters are given by the CMSSM 10.2.2 benchmark point. The squark and gluino masses we vary in parallel, just like in Fig. 5.5.

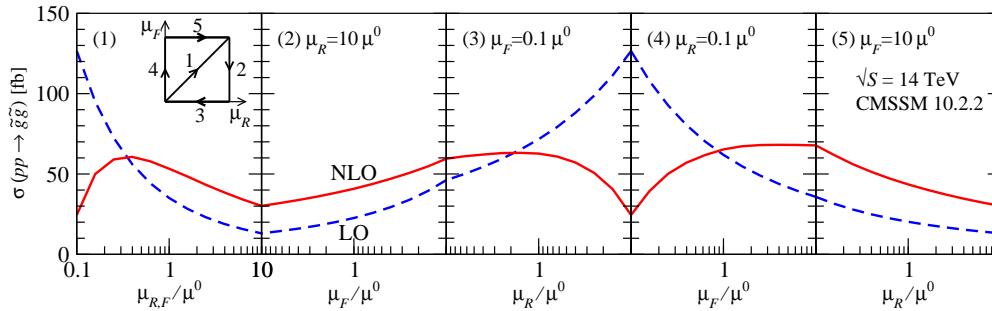


Figure 5.13: Renormalization and factorization scale dependence for gluino pair production. The plot traces a contour in the  $\mu_R$ - $\mu_F$  plane in the range  $\mu = (0.1 - 10) \times \mu^0$  with  $\mu^0 = m_{\tilde{g}}$ . All parameters are the same as for Fig. 5.7, with  $m_{\tilde{g}} = 1255$  GeV.

mass in the range  $m_{\tilde{g}} \sim 500 - 1500$ . Besides this, from the size of the envelope for the scale variations we obtain the theoretical uncertainty reduction from  $\Delta\sigma^{LO}/\sigma^{LO} \sim \mathcal{O}(70\%)$  at LO down to  $\Delta\sigma^{NLO}/\sigma^{NLO} \sim \mathcal{O}(30\%)$  at NLO.

The scale uncertainty analysis we complement with Fig. 5.13, where we predict the behavior of the cross section  $\sigma(pp \rightarrow \tilde{g}\tilde{g})$  at LO and NLO under independent variation of these scales. Again we observe a considerable flatten in the slope of the NLO cross section when compared to the LO for both scales.

Finally, let us point out that due to the stronger color charge and larger spin representation, gluino pair production constitutes the dominant SUSY-pair production mode at the LHC for most conventional MSSM benchmark, with total rates in the ballpark of 1 pb (and K factors around 2) for  $\mathcal{O}(1)$  TeV gluino masses.

Gluino pair final-states are particularly attractive in the light of the current experimental SUSY searches, which tend to disfavor 1st and 2nd generation squarks below the TeV range, while still allow stops and sbottoms in the ballpark of  $\mathcal{O}(100\text{GeV})$ . In such scenarios gluino decays into a top-stop opening excellent opportunities from the experimental viewpoint, spe-

cially if combined with the modern top tagging strategies [55].

## 5.2 Distributions

After analyzing the impact of the NLO corrections to the total rate in Sec. 5.1, now we want to perform a comprehensive study of their impact in the distributions from the fixed order expansion more specifically, we aim at: *i*) Confirming that for the processes analyzed in this chapter there are no large NLO effects present in the distribution profiles and that this conclusion holds independently from the benchmark point analyzed; *ii*) Numerically predicting the scale uncertainties for the distributions, confirming that the MLM [43] and NLO predictions agree within the theoretical uncertainty. In particular, we are interested in confirming that the usual procedure of rescaling the multi-jet merged distributions by the NLO rate is valid.

### 5.2.1 Fixed order versus multi-jet merging

As in the previous chapters, to make quantitative statements beyond total cross sections we use MADGOLEM to compute NLO distributions and for the multi-jet merging we obtain the distributions via MADGRAPH5 [6]. As in Sec. 3.5 and Sec. 4.5, the multi-jet merging approach is chosen for comparison since it has been shown to capture the main kinematic features of the process mostly in what concerns shapes of distributions. So within this method we generate tree-level matrix element events with zero, one, or two hard jets with the help of MADGRAPH5 [6] and combine them with each other and with the PYTHIA [46] shower using the MLM procedure [43] as implemented in MADGRAPH.

When defining the hard matrix element corrections we follow three different approaches:

1. We include up to one additional hard gluon in the matrix elements. This automatically excludes all topologies which could lead to on shell divergences.
2. We instead allow for two additional hard gluons in the matrix elements. As before, we avoid any possible problems with on-shell singularities.
3. We generate samples with one additional quark or gluon. In this case, the double-counting arising from on-shell states (squarks and/or gluinos, depending on the channel) will appear, just like for the real emission contributing to the NLO rate. These double-counting we remove using the numerical prescription implemented in MADGRAPH [6]. It subtracts all events with phase space configurations close to the on shell poles, by means of a slicing procedure which avoids the region in phase space close to the on-shell configurations. As we explained in Sec. 2.5 this method has some drawbacks and is not equivalent to the consistent PROSPINO scheme. However, we have checked that it gives numerically similar results as long as we only compare normalized distributions.

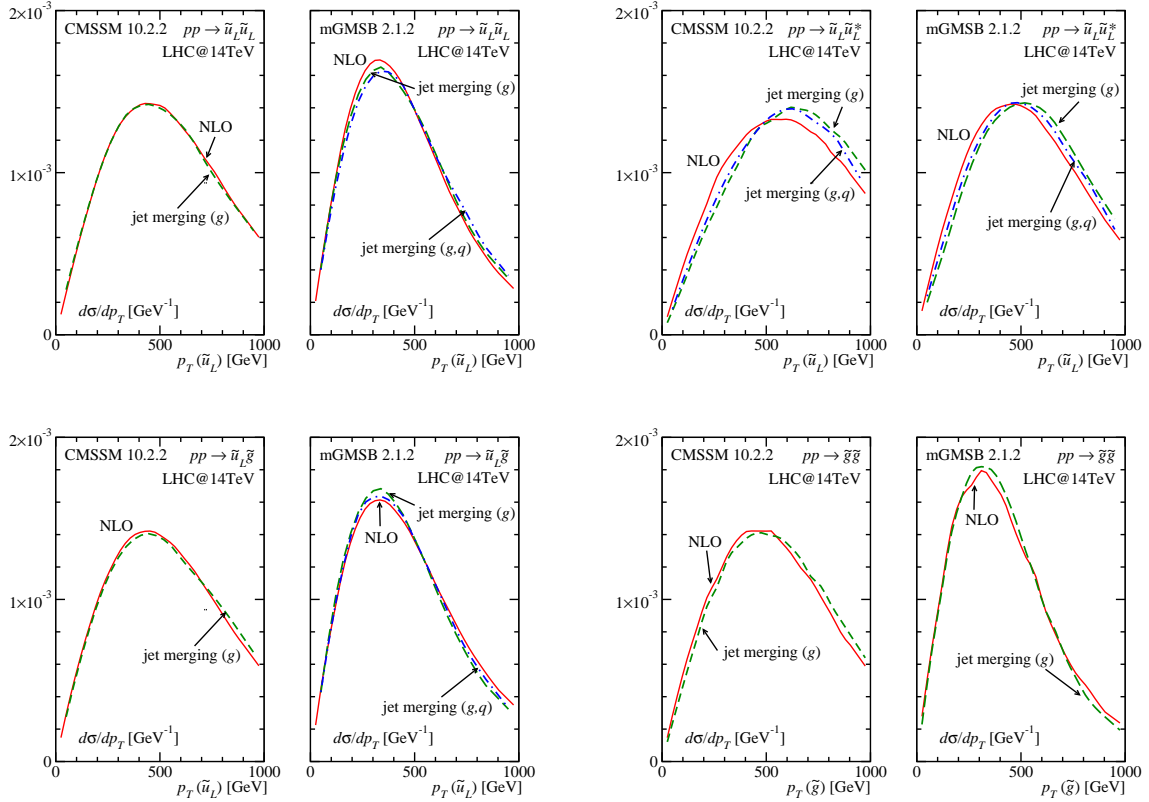


Figure 5.14: Normalized transverse momentum distributions for different processes for the benchmark points CMSSM 10.2.2 and mGMSB 2.1.2. We compare NLO predictions to LO jet merging [43] with three different setups: up to one hard gluon; up to two hard gluons; up to one hard quark or gluon jet. The latter two we only display when differences are visible.

In Fig. 5.14 we present the transverse momentum distributions of squarks and gluinos for the NLO and for these three different multi-jet merging prescriptions. To analyze the dependence on the chosen MSSM parameter space configuration we focus on two benchmark points CMSSM 10.2.2 and mGMSB 2.1.2, which present different squark-gluino mass hierarchy, see Tab. 5.1. Comparing the different jet merging setups we confirm that the one- and two-gluons merged results essentially overlap within the numerical uncertainty, so we do not show them separately. This is an effect of the large hard scale in the process (namely, the masses of the heavy final-state particles), which implies that the second radiated gluon can be well described by the parton shower. Results allowing for one additional quark or gluon jet we only show when the curves are visibly different from the single gluon jet case. From the possible three merging setups analyzed we observe that the bulk of the contribution comes from one-gluon radiation, since when adding the possible quark radiation does not change the profile of the former once the on-shell states are properly removed.

Here, as in the processes analyzed in the previous chapters ( cf. Sec. 3.5 and Sec. 4.5), we observe that the usual assumption about the stability of the main distributions does indeed

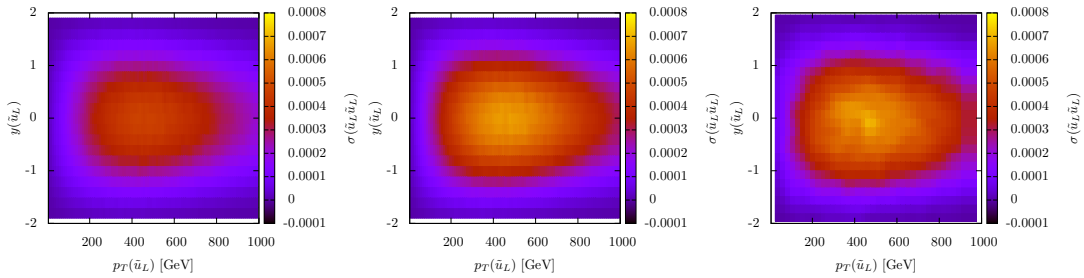


Figure 5.15: Two-dimensional distributions for squark pair production  $pp \rightarrow \tilde{u}_L \tilde{u}_L$  at  $\sqrt{S} = 14$  TeV as contour plots in the  $p_T(\tilde{u}_L)$ - $y(\tilde{u}_L)$  plane. The different panels show the results from LO (left), NLO (center), and jet merging (right). While the LO result is shown to scale the two right histograms are normalized to unity. We use the CMSSM 10.2.2 parameters.

hold correct. The normalized distributions from the fixed order NLO calculation and from multi-jet merging agree very well and just some mild departures are visible, *e.g.* in some cases the jet-merging predictions become slightly harder than the NLO results. We can essentially understand them as arising from the extra recoil jets accounted by the parton shower regime involved in the jet-merging computation.

In order to generalize this analysis we extend the comparison between the jet-merging and NLO for two-dimensional distributions in Fig. 5.15. Here we simultaneously show the NLO phase space dependence on the transverse momentum and the rapidity of one final-state particle. The three panels give LO, NLO, and merged predictions for squark pair production  $pp \rightarrow \tilde{u}_L \tilde{u}_L$ . The NLO and the merging histograms are normalized to unity, while the LO distribution is shown to scale. Once again we observe the agreement between the NLO and jet merging approach, with just mild visible departures, and without any correlations between rapidity and transverse momentum.

### 5.2.2 Scale uncertainties

In Sec. 5.1 we performed a comprehensive study of the scale uncertainties for total rates. Here we want to extend this analysis to the distribution level. For this study we focus on the squark pair production  $pp \rightarrow \tilde{u}_L \tilde{u}_L$ . In Figure 5.16 we present the squark transverse momentum and rapidity distributions. The NLO and multi-jet merging distributions are normalized to one. For the NLO curve, in order to get an estimate on the theoretical uncertainty, we compute the envelope varying the renormalization and factorization scales between  $\mu^0/2$  and  $2\mu^0$ , keeping the normalization relative to the central scale choice.

We observe that the MLM and NLO are indeed within the theoretical error. In order to quantify this statement we show two differences separately: first, the yellow (light) histogram shows the difference  $d\sigma/dp_T(\mu^0/2) - d\sigma/dp_T(2\mu^0)$ . It indicates a theoretical uncertainty of  $\mathcal{O}(10\%)$  on the distribution, with no obvious caveats. In addition, we show the difference between the central NLO prediction and MLM multi-jet merging  $d\sigma^{\text{MLM}}/dp_T - d\sigma^{\text{NLO}}/dp_T$

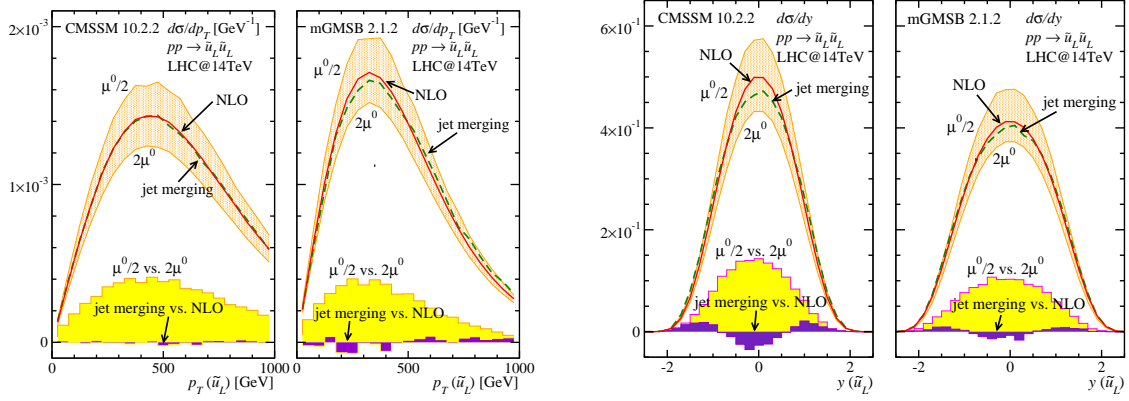


Figure 5.16: Distributions for squark pair production  $pp \rightarrow \tilde{u}_L \tilde{u}_L$  as a function of the squark transverse momentum (left) and rapidity (right). The curves for the central scales we normalize to unity. The scale uncertainty curves we normalize to the same central value. The yellow area shows the scale uncertainty, e.g.  $d\sigma/dp_T(\mu^0/2) - d\sigma/dp_T(2\mu^0)$ , compared to the purple area contrasting the jet merging and the fixed order NLO  $d\sigma^{\text{MLM}}/dp_T - d\sigma^{\text{NLO}}/dp_T$ . We examine the benchmark points CMSSM 10.2.2 and mGMSB 2.1.2.

point-by-point in the purple (dark) histogram. Both comparisons we repeat for the squark rapidity distributions. We see that when it comes to normalized distributions the NLO and MLM multi-jet merging predictions are in excellent agreement, for example compared to the sizable NLO scale dependence.

A complementary viewpoint in terms of phase space dependent  $K$  factors we display in Fig. 5.17. The NLO histograms using central scales  $\mu^0$  are supplemented by a band showing a simultaneous renormalization and factorization scale dependence at NLO. We confirm that

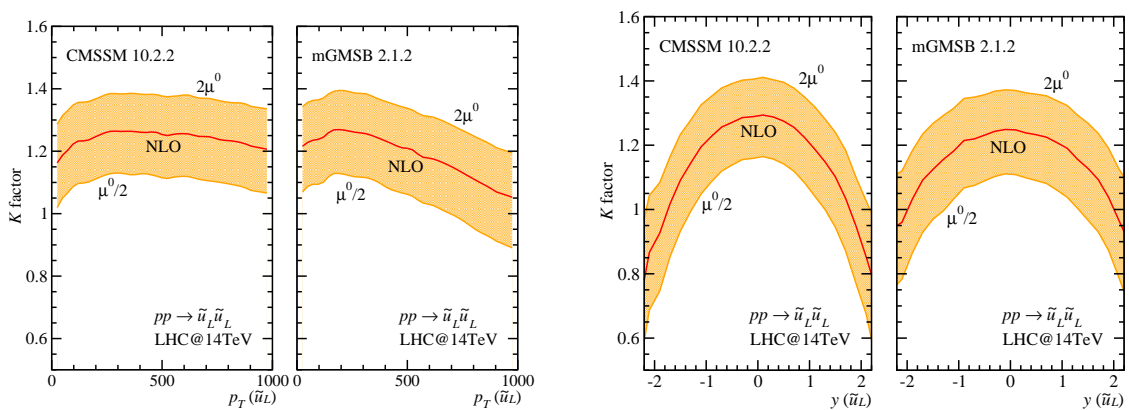


Figure 5.17:  $K$  factor as a function of  $p_T(\tilde{u}_L)$  and  $y(\tilde{u}_L)$  for squark production  $pp \rightarrow \tilde{u}_L \tilde{u}_L$ . The band shows a scale variation  $\mu^0/2 < \mu < 2\mu^0$ . All MSSM parameters we fix to CMSSM 10.2.2 and mGMSB 2.1.2.

the  $K$  factors remain stable and relatively constant for the transverse momentum and the central rapidity regime. From the above discussion we know that the slight change in the  $K$  factor over the entire phase space should correspond to distributions computed using multi-jet merging. This result we interpret as a strong argument in favor of the conventional procedure, where a global  $K$ -factor or event re-weighting to NLO is applied to kinematic distributions generated via multi-jet merging.

### 5.3 Degenerate versus non-degenerate squarks

In this section we want to check the validity of the usual assumptions taken in the literature and in the presently available tools for the NLO predictions, e.g. in PROSPINO [17–20], which introduce simplifying relations between the supersymmetric masses (such as squark mass degeneracy) to calculate the NLO effects. In MADGOLEM these assumptions are not necessary and we can freely scan over the entire parameter space of a given model, varying each input parameters independently. A general fully unconstrained scan as shown in Tab. 5.2, is thus beyond the reach of these previous tools. Our target in this section is to analyze the numerical impact of these simplifying relations directly quantifying their influence on rates and distributions.

#### 5.3.1 Rates

We address the effect of a general squark mass pattern on total rates in Figure 5.18. In this analysis we focus on the (partially inclusive) production of all first-generation squark pairs  $pp \rightarrow \tilde{q}\tilde{q}$  (figures on top) and squark–gluino production  $pp \rightarrow \tilde{q}\tilde{g}$  (figures at the bottom) with  $\tilde{q} = \tilde{u}_L, \tilde{u}_R, \tilde{d}_L, \tilde{d}_R$ , and examine the response to an independent variation of the different squark masses. As benchmark points for our study we take CMSSM 10.2.2 and mGMSB 2.1.2 scenarios. For each of them, we explore the relative change in the total rate  $|\sigma - \sigma^0|/\sigma^0$  when we increase mass splittings from zero ( $\sigma_0$ ). We separately examine the following two cases: *i*) fixing all left-handed and right-handed squarks at one common mass value and increasing the right-left mass splitting  $\Delta m_{R-L}$ ; and *ii*) setting a common mass for up-type and down-type squarks and increasing  $\Delta m_{u-d}$ . We observe that for the two processes analyzed the total rates change by  $\mathcal{O}(5 - 20\%)$  for a squark mass splitting of 10 – 100 GeV, as commonly featured by most of the conventional MSSM benchmark points. Therefore these effects lie within the NLO theory uncertainty.

Complementarily we observe that the LO and NLO rates scale in parallel, with a small deviation at the few per-cent level. This relies on the fact that the main effect when varying the splitting, in what concerns total rates, is to change the phase space suppression from the final-state particles. The impact of these mass shifts on the genuine virtual corrections, instead, is rather meager as the SUSY-QCD effects are typically mass suppressed. This implies that the  $K$  factors are essentially constant when increasing the mass separation. Thus, the MADGOLEM results confirm that the PROSPINO  $K$ -factors  $K_{\text{PROSPINO}} = \sigma_{\text{degenerate}}^{\text{NLO}}/\sigma_{\text{degenerate}}^{\text{LO}}$ , which do not take into account the mass splitting neither for the LO rate  $\sigma_{\text{degenerate}}^{\text{LO}}$  nor

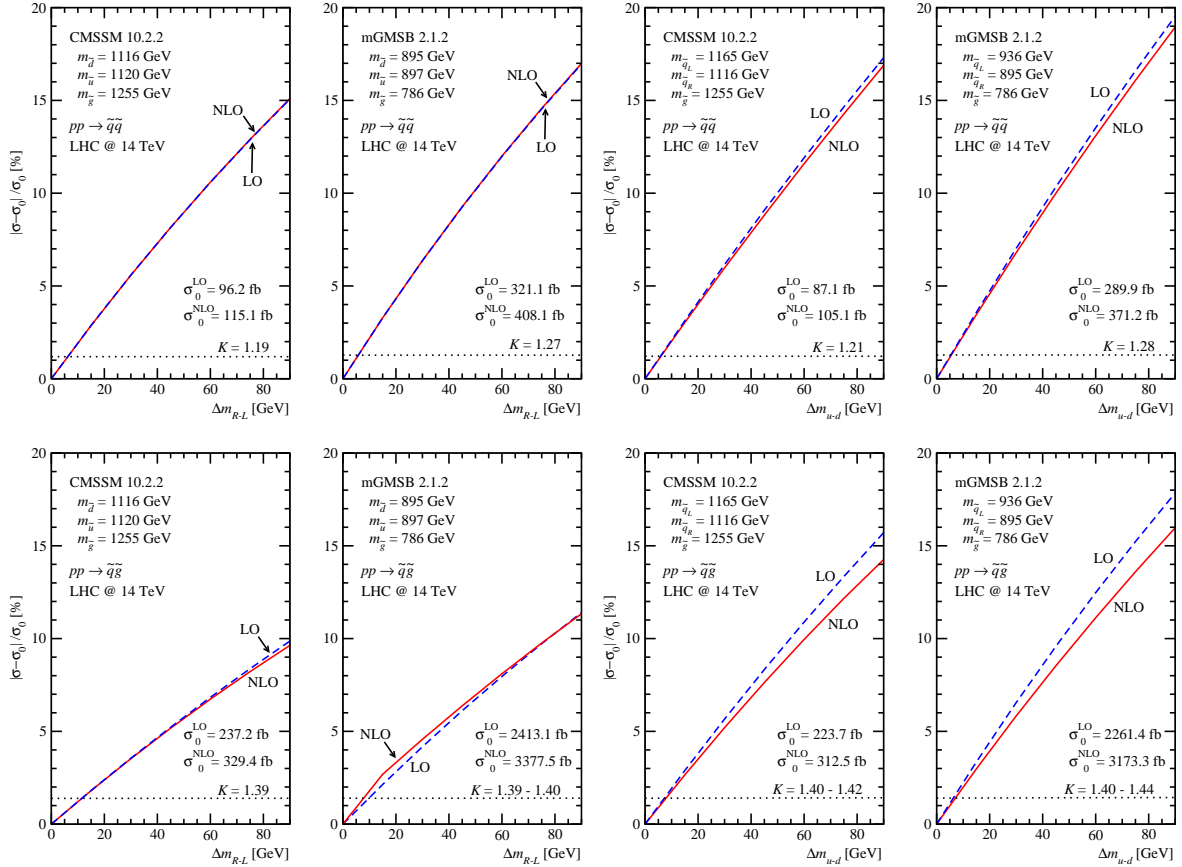


Figure 5.18: Cross sections for squark pair production  $pp \rightarrow \tilde{q}\tilde{q}$  (figures on the top) and squark–gluino production  $pp \rightarrow \tilde{q}\tilde{g}$  (figures on the bottom), with  $\tilde{q} = \tilde{u}_{L,R}, \tilde{d}_{L,R}$ , as a function of mass splittings. In the left panels we vary the right-left splitting keeping the flavor splitting constant. In the right panels we vary the  $\tilde{u}\text{--}\tilde{d}$  flavor splitting fixing the right-left splitting. We show the shift with respect to the degenerate spectrum with the masses and the total rates  $\sigma_0 \equiv \sigma(\Delta m = 0)$  given in each panel.

for the NLO  $\sigma_{\text{degenerate}}^{\text{NLO}}$  to a very good approximation correct. In fact PROSPINO uses this fact to reduce the uncertainty of their total NLO rates  $\sigma_{\text{PROSPINO}}^{\text{NLO}}$  by generating the LO rate  $\sigma_{\text{non-degenerate}}^{\text{LO}}$  separately with the full unrestricted mass spectrum and rescaling it at NLO by means of their K-factor (with mass degeneracy)

$$\sigma_{\text{PROSPINO}}^{\text{NLO}} = K_{\text{PROSPINO}} \sigma_{\text{non-degenerate}}^{\text{LO}}, \quad (5.4)$$

which, according to our results, should give an accurate estimate of the full NLO rate.

### 5.3.2 Distributions

Although in terms of total rates the impact of a general, mass unconstrained splitting induces variations not larger than a few per-cent, when looking at distributions its footprint becomes much more apparent. In Fig. 5.19 we display the squark transverse momentum and rapidity

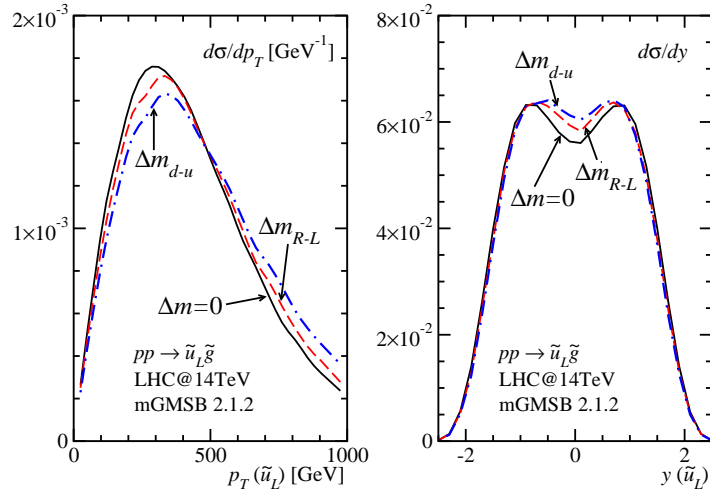


Figure 5.19: Normalized transverse momentum (left) and rapidity distributions (right) for squark–gluino production  $pp \rightarrow \tilde{u}_L \tilde{g}$ . We assume (i) mass-degenerate squarks with  $m_{\tilde{q}} = 800$  GeV; (ii) a common mass splitting,  $\Delta m_{R-L} = 200$  GeV; (iii) a common mass splitting,  $\Delta m_{d-u} = 200$  GeV. The central MSSM parameters we fix as in mGMSB 2.1.2 benchmark.

distributions for the particular case of squark–gluino production. We single out one particular production channel,  $pp \rightarrow \tilde{u}_L \tilde{g}$  and examine the following representative situations: (i) mass-degenerate squarks, with  $m_{\tilde{q}} = 800$  GeV; (ii) a right-left splitting  $\Delta m_{R-L} = 200$  GeV; and (iii) a similar down-up splitting  $\Delta m_{d-u} = 200$  GeV. The remaining MSSM parameters we set as in the mGMSB 2.1.2 benchmark point defined in Table 5.1. Most importantly, we keep the final-state mass constant, so the differences between these three scenarios decouple from the leading influence of phase space suppression and instead constitute a genuine NLO effect.

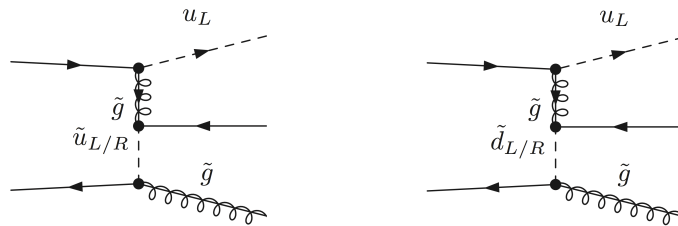


Figure 5.20: Feynman diagrams which describe the squark–gluino fusion mechanism responsible for the significant differences in the distribution profiles when changing the mass splitting.

We observe that the finite mass splitting between squarks induces a shift in the kinematic distributions in the direction of slightly harder and more central final-state squarks. This can be traced back to the real emission corrections shown in Fig. 5.20. These diagrams describe a fusion mechanism where the bulk contribution arises from internal squark and gluino propagators at very small virtuality, *i.e.* when these particles are almost on-shell. As a result, they become particularly sensitive to variations of the squark masses, even if the

final-state squarks masses remain unchanged. Quantitatively, the mass splitting between up-type and down-type squarks lead to an effect of  $\mathcal{O}(20\%)$  in the distributions, therefore this saturates the NLO uncertainty on the transverse momentum distributions, which falls into the same ballpark, as illustrated in Fig 5.16. In other words, we conclude that, at variance with the situation for total rates, the mass degeneracy approximation is not suitable to the same extent for distributions. A proper account of all kinematic effects demands complete calculation with a general (unrestricted) mass spectrum.

# Chapter 6

## Conclusions

In this thesis we have presented a comprehensive analysis at NLO QCD level for several new physics signatures: *i*) scalar color-octet (sgluon) pair production; *ii*) the SUSY associated production of squark-gaugino  $pp \rightarrow \tilde{q}\tilde{\chi}$ , as an example of a process driven by SUSY-EW interactions; and *iii*) the main discovery channels for SUSY at the LHC, these are the pair production processes of strongly interacting particles  $pp \rightarrow \tilde{q}\tilde{q} (\tilde{q}\tilde{q}^*) [\tilde{q}\tilde{g}] \{\tilde{g}\tilde{g}\}$ . These physics analyses were performed with our fully automated tool MADGOLEM, which automatizes NLO QCD calculations for  $2 \rightarrow 2$  processes in the context of new physics models. The work carried out in this thesis has led to several major contributions to the development of this tool, to wit:

- The implementation, for the first time in the literature, of an automated procedure to subtract the potential double-counting instances involved in the production and decay of on shell heavy states. The subtraction method is based on a local procedure, originally developed in the PROSPINO framework, and that presents a number of advantages as compared to the alternative approaches considered in the literature. In particular, it preserves gauge invariance and spin correlations. Our implementation takes the form of an independent add-on to MADGOLEM, dubbed MADOS, which subtracts in a process and model independent way, any possible double-counting arising from the on shell heavy particles.
- The extension of the IR divergence subtraction procedure to the genuine novel structures that appear when considering theories beyond the SM. This extension consisted in the implementation of the required Catani-Seymour dipoles in MADGOLEM as an expanded stand-alone version of MADDIPOLE, which we upgraded including the dependence on the FKS-style phase space parameter, dubbed  $\alpha$ . The analytical form of these  $\alpha$ -dependent SUSY dipoles we have derived independently and the results are thoroughly documented in the Appendix A.
- The systematic cross-check of the modules we implemented, namely the extended set of Catani-Seymour dipoles and the on shell subtraction MADOS, both as stand-alone packages and also when interfaced with the remaining routines in the whole MAD-

GOLEM architecture. These checks include the comparison of the results with other tools, when these are available, and also a set of consistency tests, *e.g.* *i)* The explicit cancellation of the IR poles, which we have confirmed numerically for a wide set of representative SM and BSM  $2 \rightarrow 2$  processes to an accuracy of  $\mathcal{O}(10^{-7})$ ; *ii)* the independence of total NLO rates and distributions on the FKS-like phase space parameter  $\alpha$ ; *iii)* the independence of the total rates and distributions on the regulator  $\Gamma$  introduced in the On Shell subtraction method in the region  $\Gamma \ll m$ .

In this thesis we have first reviewed some fundamental aspects of QCD, in special presenting the general structure of a NLO computation, and we have introduced the main elements of our calculation in Chapter 2. We have discussed the basics of the Catani-Seymour approach to deal with IR singularities and also devoted special care to introduce the On Shell Subtraction method, both aspects furnishing the theoretical basis on which the core of the development achieved in this thesis rely. Moreover, we have presented the basic structure of our MADGOLEM package and summarized the basic numerical tests carried out to assess the robustness and reliability of its performance.

Next we have turned our attention to the phenomenological analysis of several new physics processes at NLO. Chapter 3 is dedicated to the NLO analysis of the sgluon pair production at the LHC. We find large NLO production rates and sizeable quantum effects ( $K \sim 1.5 - 2$ ). In what concerns distributions, we obtain a mild shift in the sgluon distributions when compared to the multi-jet merging computation, this meaning a very good agreement in the overall. We present as well the experimental bounds from the ATLAS collaboration, in which the theoretical predictions were generated with the help of our code MADGOLEM. The results indicate that the sgluons are excluded at 95% C.L. for masses below  $\sim 300$  GeV.

In Chapter 4 we study the squark-neutralino production to NLO. We find moderate corrections ( $K \sim 1.4$ ) to the production rate with a strongly reduced theory uncertainty. The K-factors are shown to be highly independent on the specific MSSM configuration we consider, and the quantum corrections are shown to be driven primordially by pure QCD effects, *i.e.* gluonic contributions. Again we prove that the distributions at NLO level agree very well with the multi-jet merging ones.

In Chapter 5 we present an upgrade to the current NLO predictions for squark and gluino production. Even if the NLO predictions for these major SUSY discovery channels were first made available more than one decade ago, our analysis represents substantial improvements in respect to them, not only because the predictions are derived in a fully automated framework, but also because no condition on the mass spectrum nor the pattern of SUSY interactions needs to be assumed as simplifying hypothesis. We can then comprehensively survey a set of conventional MSSM benchmark points in agreement with the current constraints on SUSY searches. When comparing the results for a mass-degenerate squark spectrum to those corresponding to moderate squark mass splittings, we observe changes in the K-factors at the percent level, and within the scale uncertainty. However, the effects of non-degenerate spectra are shown to be clearly visible for squark and gluino distributions. With the later observation that, at the distribution level, this assumption does not work perform so satisfactory as it

does for the total rates.

We can identify therefore a number of trademark characteristics of heavy particle production at the LHC, which we can summarize as follows:

- The NLO correction provides a total rate with strongly suppressed dependences on the unphysical renormalization and factorization scales, when comparing them to the LO yields. This leads to a final result with moderate theoretical uncertainties, which are typically pulled down to  $\mathcal{O}(30\%)$  from the  $\mathcal{O}(100\%)$  featured by the LO predictions.
- The bulk quantum effects arise from pure QCD (gluon mediated) effects, whereas the one-loop corrections which have massive particles flowing in the corresponding one-loop diagrams are relatively milder when compared to the gluonic corrections. This leads to K-factors which are largely independent on the new heavy particle masses, e.g. on the mass spectrum of SUSY particles or on the sgluon mass.
- The distributions at NLO are in good agreement with those obtained from the multi-jet merging calculations. Moreover, we have confirmed that the K-factors remain stable and relatively constant for all the kinematically relevant regions. In this thesis we have illustrated this fact for the specific case of squark pair production. Even if it is true that this behavior should be analyzed for each particular process, set of parameters and kinematic distribution independently, our results convincingly support the standard procedure by which the whole distribution generated via multi-jet merging is rescaled by a global K-factor.

The above conclusions summarize in a nutshell the core results of our contribution to the LHC physics program, mainly in the qualitative understanding and quantitative evaluation, of the NLO QCD effects to the production of heavy BSM particles, as well as in the development of tools for the automated calculation of these theoretical predictions. The work performed in this thesis has resulted into key contributions to the implementation to the automated package MADGOLEM.

Looking further, we wish to extend this work along the following lines: *i)* Extend the new physics models supported by MADGOLEM; *ii)* Upgrade the tool to a more recent version of the software MADGRAPH; *iii)* Use our framework to novel applications to phenomenology, e.g. single top production at NLO in the presence of higher dimension operators and combined with cutting-edge signal identification and analysis techniques – top tagger based on jet substructure and boosted objects [55].



# Appendix A

## Catani-Seymour SUSY and sgluon dipoles

In this appendix we present the unintegrated and integrated dipoles required for SUSY-QCD calculations [14] and for the sgluon model including a phase-space constraint [42]. They are implemented as an independent add-on to the MADDIPOLE package [25] and are part of the automated MADGOLEM framework.

### A.1 General aspects

There exist two major approaches to remove soft and collinear singularities: *phase-space slicing* and *subtraction methods* [56]. A simple toy example captures their main features and highlights the role of an FKS-like phase-space constraint [42], “ $\alpha$  parameter”. Let us consider the dimensionally regularized integral  $\int_0^1 dx f(x)/x^{1-\epsilon}$  with  $\epsilon > 0$ . Phase space slicing based on a small parameter  $\alpha$  yields

$$\begin{aligned} \int_0^1 dx \frac{f(x)}{x^{1-\epsilon}} &= \int_\alpha^1 dx \frac{f(x)}{x^{1-\epsilon}} + \int_0^\alpha dx \frac{f(0)}{x^{1-\epsilon}} + \mathcal{O}(\alpha) \\ &= \int_\alpha^1 dx \frac{f(x)}{x} + \frac{f(0)}{\epsilon} + f(0) \log \alpha + \mathcal{O}(\alpha; \epsilon) . \end{aligned} \quad (\text{A.1})$$

Observe that the final result still depends on the actual value of the  $\alpha$  parameter. This is the reason why one should set this parameter to the smallest possible value. A numerically more stable approach is phase-space subtraction, where the same integral becomes

$$\begin{aligned} \int_0^1 dx \frac{f(x)}{x^{1-\epsilon}} &= \int_0^1 dx \frac{f(x) - f(0) \Theta(x \leq \alpha)}{x^{1-\epsilon}} + \int_0^\alpha dx \frac{f(0)}{x^{1-\epsilon}} \\ &= \int_0^1 dx \frac{f(x) - f(0) \Theta(x \leq \alpha)}{x} + \frac{f(0)}{\epsilon} + f(0) \log \alpha + \mathcal{O}(\epsilon) . \end{aligned} \quad (\text{A.2})$$

In this case the divergency is subtracted locally and the final result no longer depends on  $\alpha$ , which can then be used as a test of the implementation. The parameter  $\alpha$  can be set in the whole range  $0 < \alpha \leq 1$ . For small values of  $\alpha$  one would now have the numerical

advantage to evaluate just one part of the integrand, speeding up the calculation, if  $f(x)$  is time consuming to evaluate. It is important to notice that in the case of the subtraction method the logarithmic dependence with  $\alpha$  is exactly canceled in the total result which is not true for the phase-space slicing.

The toy model of Eq. (A.2) carries the essence of the Catani-Seymour subtraction method. CS propose an algorithm to regularize the IR divergencies arising from the real emissions ( $d\sigma^{\text{real}}$ ), where integral is performed in  $m+1$ -particle dimension, via a “plus-prescription” like distribution. This regularization is performed via a local subtraction term ( $d\sigma^{\text{A}}$ ) constructed using the universality of the soft/collinear limits. The  $\epsilon$  poles from the real emission are shuffled to the integral of the virtual part. The divergence can then cancel in the same  $m$ -particle dimension integration. On this way the integrations can be performed numerically, as it is represented schematically in the Eq. (A.3). This circumvents the main problem of IR poles arising in different phase-space dimensions.

$$\delta\sigma^{\text{NLO}} = \int_{m+1} \left( d\sigma_{\epsilon=0}^{\text{real}} - d\sigma_{\alpha, \epsilon=0}^{\text{A}} \right) + \int_m \left( d\sigma^{\text{virtual}} + d\sigma^{\text{collinear}} + \int_1 d\sigma_{\alpha}^{\text{A}} \right)_{\epsilon=0} \quad (\text{A.3})$$

Below, we present the unintegrated dipoles  $d\sigma_{\alpha}^{\text{A}}$  as well as the integrated dipoles  $\int_1 d\sigma_{\alpha}^{\text{A}}$  including their  $\alpha$  dependence. They are crucial for SUSY-QCD processes or other NLO QCD predictions beyond the Standard Model. Our extended set of massive Catani-Seymour dipoles with explicit  $\alpha$  dependence has several practical advantages:

- tuning  $\alpha$  we reduce the subtraction phase-space and hence the number of events for which the real-emission matrix element and the subtraction fall into different bins; the so-called *binning problem*.
- choosing  $\alpha < 1$  we evaluate the subtraction terms only in the phase-space region where they matter, *i.e.* close to the IR divergences.
- our final result should not depend on  $\alpha$ . This serves as a test for example of the adequate coverage of all the singularities or the relative normalization of the two-particle and three-particle phase-space.

In the MSSM gluino and squark interactions induced by the covariant derivatives  $\bar{g}\not{D}\tilde{g}$ ,  $|D_{\mu}\tilde{q}|^2$  give rise to new IR divergences which are absent in the Standard Model. The emission of a soft gluon from these particles requires new final-final dipoles  $D_{ij,k}$  and final-initial dipoles  $D_{ij}^{\alpha}$ . Initial-initial and initial-final configurations can also have a squark or gluino as spectator, but the dipole only carries information about the mass of the colored spectator, not about its spin. This means we can simply use the massive Standard Model dipoles [14] with an extra SUSY particle in the final state. Similarly, the interactions induced by the sgluon covariant derivative  $D_{\mu}G^{*}D^{\mu}G$  lead to new types of IR divergencies, since it is a color-octet with spin zero its dipoles are identical to supersymmetric scalar quarks with modified color factors  $C_F \rightarrow C_A$ . In all the expressions that follows for the squarks we will obtain the sgluon dipoles if done this replacement. To make this Appendix most useful we will firmly stick to the conventions of Ref. [14].

## A.2 Final-final dipoles

We start with a collection of formulas for final-final dipoles. The expression for the unintegrated dipole is given by

$$D_{ij,k} = -\frac{1}{2p_i \cdot p_j} \langle \dots, \tilde{i}j, \dots, \tilde{k}, \dots | \frac{\mathbf{T}_k \mathbf{T}_{ij}}{\mathbf{T}_{ij}^2} \mathbf{V}_{ij,k} | \dots, \tilde{i}j, \dots, \tilde{k}, \dots \rangle, \quad (\text{A.4})$$

where  $|\dots, \tilde{i}j, \dots, \tilde{k}, \dots\rangle$  represents the amplitude for the factorized born process, which in the special case of the SUSY dipoles is made by the removal of the gluon from the diagonal splitting  $\tilde{q}(p_{ij}) \rightarrow \tilde{q}(p_j)g(p_i)$ . The color matrix  $\mathbf{T}_k \mathbf{T}_{ij} / \mathbf{T}_{ij}^2$  acts on the born amplitude  $|\dots, \tilde{i}j, \dots, \tilde{k}, \dots\rangle$  giving the proper color factor.

To compute the integrated dipoles we integrate over the one-particle phase-space  $[dp_i(\tilde{p}_{ij}, \tilde{p}_k)]$  with the spin average matrices  $\langle \mathbf{V}_{ij,k} \rangle$ , according to Eq.(5.22) of Ref. [14]:

$$\int [dp_i(\tilde{p}_{ij}, \tilde{p}_k)] \frac{1}{(p_i + p_j)^2 - m_{ij}^2} \langle \mathbf{V}_{ij,k} \rangle \equiv \frac{\alpha_s}{2\pi} \frac{1}{\Gamma(1-\epsilon)} \left( \frac{4\pi\mu^2}{Q^2} \right)^\epsilon I_{ij,k}(\epsilon), \quad (\text{A.5})$$

where the squark dipole function,  $\langle s | \mathbf{V}_{g\tilde{q},k} | s' \rangle$ , is given by Eq.(C.1) of the same reference,

$$\frac{\langle s | \mathbf{V}_{g\tilde{q},k} | s' \rangle}{8\pi\mu^{2\epsilon}\alpha_s C_F} = \left[ \frac{2}{1 - \tilde{z}_j(1 - y_{ij,k})} - \frac{\tilde{v}_{ij,k}}{v_{ij,k}} \left( 2 + \frac{m_{\tilde{q}}^2}{p_i p_j} \right) \right] \delta_{ss'} = \frac{\langle \mathbf{V}_{g\tilde{q},k} \rangle \delta_{ss'}}{8\pi\mu^{2\epsilon}\alpha_s C_F}. \quad (\text{A.6})$$

Compared to a massive quark the squark structure is much simpler. This is because for scalars the labels  $s$  and  $s'$  are merely tagging the helicity of the associated quark partners without any effect on the squark splitting.

The integrated dipole  $I_{g\tilde{q},k}$  we decompose into an soft or eikonal part  $I^{\text{eik}}$  and a collinear integral  $I_{g\tilde{q},k}^{\text{coll}}$  evaluated in  $4 - 2\epsilon$  dimensions,

$$\begin{aligned} I_{g\tilde{q},k}(\mu_{\tilde{q}}, \mu_k; \epsilon) &= C_F \left[ 2I^{\text{eik}}(\mu_{\tilde{q}}, \mu_k; \epsilon) + I_{g\tilde{q},k}^{\text{coll}}(\mu_{\tilde{q}}, \mu_k; \epsilon) \right] \\ \tilde{v}_{g\tilde{q},k} I^{\text{eik}} &= \frac{1}{2\epsilon} \log \rho - \log \rho \log \left( 1 - (\mu_{\tilde{q}} + \mu_k)^2 \right) - \frac{1}{2} \log^2 \rho_{\tilde{q}} - \frac{1}{2} \log^2 \rho_k \\ &\quad + \zeta_2 + 2\text{Li}_2(-\rho) - 2\text{Li}_2(1-\rho) - \frac{1}{2}\text{Li}_2(1-\rho_{\tilde{q}}^2) - \frac{1}{2}\text{Li}_2(1-\rho_k^2) \\ I_{g\tilde{q},k}^{\text{coll}} &= \frac{2}{\epsilon} - \frac{1}{\epsilon\mu_{\tilde{q}}^{2\epsilon}} - \frac{2}{\mu_{\tilde{q}}^{2\epsilon}} + 6 - 2 \log \left( (1 - \mu_k)^2 - \mu_{\tilde{q}}^2 \right) + \frac{4\mu_k(\mu_k - 1)}{1 - \mu_{\tilde{q}}^2 - \mu_k^2}. \end{aligned} \quad (\text{A.7})$$

The rescaled masses  $\mu_n$  and the variables  $\rho$  and  $\rho_n$  associated with the splitting  $\tilde{i}j \rightarrow ij$  and the spectator  $k$  are defined in terms of the final state momenta  $p_i$ ,  $p_j$  and  $p_k$  as

$$\begin{aligned} \mu_n &= \frac{m_n}{\sqrt{(p_i + p_j + p_k)^2}} \\ \rho &= \sqrt{\frac{1 - \tilde{v}_{ij,k}}{1 + \tilde{v}_{ij,k}}} \quad \text{with} \quad \tilde{v}_{ij,k} = \frac{\sqrt{\lambda(1, \mu_{ij}^2, \mu_k^2)}}{1 - \mu_{ij}^2 - \mu_k^2} \\ \rho_n(\mu_j, \mu_k) &= \sqrt{\frac{1 - \tilde{v}_{ij,k} + 2\mu_n^2 / (1 - \mu_j^2 - \mu_k^2)}{1 + \tilde{v}_{ij,k} + 2\mu_n^2 / (1 - \mu_j^2 - \mu_k^2)}} \quad (n = j, k), \end{aligned} \quad (\text{A.8})$$

with  $\lambda$  denoting the Källén function

$$\lambda(x, y, z) = x^2 + y^2 + z^2 - 2xy - 2xz - 2yz. \quad (\text{A.9})$$

The splitting kinematics we describe using

$$\tilde{z}_j = 1 - \frac{p_i p_k}{p_i p_k + p_j p_k} \quad \text{and} \quad y_{ij,k} = \frac{p_i p_j}{p_i p_j + p_i p_k + p_j p_k} > y_+ = 1 - \frac{2\mu_k(1-\mu_k)}{1-\mu_i^2-\mu_j^2-\mu_k^2}. \quad (\text{A.10})$$

Just like for massive quarks there is no collinear singularity, so the most divergent term in the  $I_{g\tilde{q},k}(\epsilon)$  is a single  $1/\epsilon$  pole.

To include the phase-space parameter  $\alpha$  into the massive squark dipole we limit the dipole function to small values of  $y_{ij,k}/y_+$

$$D_{g\tilde{q},k} \rightarrow D_{g\tilde{q},k} \Theta\left(\frac{y_{ij,k}}{y_+} < \alpha\right) \quad \alpha \in (0, 1]. \quad (\text{A.11})$$

For the integrated dipole  $I_{g\tilde{q},k}(\epsilon)$  we start from Eq.(A.7) and subtract the finite term including the same kinematic condition as Eq.(A.11)

$$\begin{aligned} I_{g\tilde{q},k}(\epsilon, \alpha) &= I_{g\tilde{q},k}(\epsilon) + \Delta I_{g\tilde{q},k}(\alpha) \\ &= I_{g\tilde{q},k}(\epsilon) - \frac{2\pi}{\alpha_s} \int [dp_g(\tilde{p}_{g\tilde{q}}, \tilde{p}_k)] \frac{\langle \mathbf{V}_{g\tilde{q},k} \rangle}{2p_g p_{\tilde{q}}} \Theta\left(\frac{y_{g\tilde{q},k}}{y^+} > \alpha\right). \end{aligned} \quad (\text{A.12})$$

The finite part we can evaluate in four dimensions, because by definition there exists no divergence in the region  $y_{g\tilde{q},k}/y^+ > \alpha$ . The eikonal part  $2/[1 - \tilde{z}_{\tilde{q}}(1 - y_{g\tilde{q},k})]$  is the same for  $\langle s | \mathbf{V}_{gQ,k} | s' \rangle$  and  $\langle s | \mathbf{V}_{g\tilde{q},k} | s' \rangle$ , so in Eq.(A.12) we insert Eq.(A.7) from our appendix and Eq.(A.9) from Ref. [57],

$$\begin{aligned} \tilde{v}_{g\tilde{q},k} \Delta I^{\text{eik}}(\alpha) &= -\text{Li}_2\left(\frac{a+x}{a+x_+}\right) + \text{Li}_2\left(\frac{a}{a+x_+}\right) + \text{Li}_2\left(\frac{x_+-x}{x_+-b}\right) - \text{Li}_2\left(\frac{x_+}{x_+-b}\right) \\ &+ \text{Li}_2\left(\frac{c+x}{c+x_+}\right) - \text{Li}_2\left(\frac{c}{c+x_+}\right) + \text{Li}_2\left(\frac{x_--x}{x_++a}\right) - \text{Li}_2\left(\frac{x_-}{x_++a}\right) \\ &- \text{Li}_2\left(\frac{b-x}{b-x_-}\right) + \text{Li}_2\left(\frac{b}{b-x_-}\right) - \text{Li}_2\left(\frac{x_--x}{x_++c}\right) + \text{Li}_2\left(\frac{x_-}{x_++c}\right) \\ &+ \text{Li}_2\left(\frac{b-x}{b+a}\right) - \text{Li}_2\left(\frac{b}{b+a}\right) - \text{Li}_2\left(\frac{c+x}{c-a}\right) + \text{Li}_2\left(\frac{c}{c-a}\right) \\ &+ \log(c+x) \log\left(\frac{(a-c)(x_+-x)}{(a+x)(c+x_+)}\right) - \log(c) \log\left(\frac{(a-c)x_+}{a(c+x_+)}\right) \\ &+ \log(b-x) \log\left(\frac{(a+x)(x_--b)}{(a+x)(x_--x)}\right) - \log(b) \log\left(\frac{a(x_--b)}{(a+b)x_-}\right) \\ &- \log((a+x)(b-x_+)) \log(x_+-x) + \log(a(b-x_+)) \log(x_+) \\ &+ \log(d) \log\left(\frac{(a+x)x_+x_-}{a(x_+-x)(x_--x)}\right) + \log\left(\frac{x_--x}{x_-}\right) \log\left(\frac{c+x_-}{a+x_-}\right) \\ &+ \frac{1}{2} \log\left(\frac{a+x}{a}\right) \log\left(a(a+x)(a+x_+)^2\right), \end{aligned} \quad (\text{A.13})$$

where

$$a = \frac{2\mu_k}{1 - \mu_{\tilde{q}}^2 - \mu_k^2}, \quad b = \frac{2(1 - \mu_k)}{1 - \mu_{\tilde{q}}^2 - \mu_k^2}, \quad (\text{A.14})$$

$$c = \frac{2\mu_k(1 - \mu_k)}{1 - \mu_{\tilde{q}}^2 - \mu_k^2}, \quad d = \frac{1}{2}(1 - \mu_{\tilde{q}}^2 - \mu_k^2), \quad (\text{A.15})$$

$$(\text{A.16})$$

and

$$x_{\pm} = \frac{(1 - \mu_k)^2 - \mu_{\tilde{q}}^2 \pm \sqrt{\lambda(1, \mu_{\tilde{q}}^2, \mu_k^2)}}{1 - \mu_{\tilde{q}}^2 - \mu_k^2}. \quad (\text{A.17})$$

The collinear part is different for squarks, so we supplement its form in Eq.(A.7) by

$$\Delta I_{g\tilde{q},k}^{\text{coll}}(\alpha) = -\frac{C_F}{2\pi^2} \left[ \frac{(1 - \mu_k)^2 - \mu_{\tilde{q}}^2}{1 - \mu_{\tilde{q}}^2 - \mu_k^2} (1 - \alpha) + \log \alpha \right]. \quad (\text{A.18})$$

### A.3 Final-initial dipoles

Following the same logic we tackle the final-initial dipoles. The final-initial dipole function is given by Eq.(C.3) of Ref. [14],

$$\langle \mathbf{V}_{g\tilde{q}}^a \rangle = 8\pi\mu^{2\epsilon}\alpha_s C_F \left( \frac{2}{2 - x_{g\tilde{q},a} - \tilde{z}_{\tilde{q}}} - 2 - \frac{m_{\tilde{q}}^2}{p_g p_{\tilde{q}}} \right). \quad (\text{A.19})$$

The integrated dipole function  $I_{g\tilde{q}}^a$  becomes

$$I_{g\tilde{q}}^a(x; \epsilon) = C_F \left[ (J_{g\tilde{q}}^a(x, \mu_{\tilde{q}}))_+ + \delta(1 - x) \left( J_{g\tilde{q}}^{a;S}(\mu_{\tilde{q}}; \epsilon) + J_{g\tilde{q}}^{a;NS}(\mu_{\tilde{q}}) \right) \right] + \mathcal{O}(\epsilon), \quad (\text{A.20})$$

with the three contributions  $I_{g\tilde{q}}^a$

$$\begin{aligned} [J_{g\tilde{q}}^a(x, \mu_{\tilde{q}})]_+ &= -2 \left( \frac{1 + \log(1 - x + \mu_{\tilde{q}}^2)}{1 - x} \right)_+ + \left( \frac{2}{1 - x} \right)_+ \log(2 + \mu_{\tilde{q}}^2 - x) \\ J_{g\tilde{q}}^{a;S}(\mu_{\tilde{q}}; \epsilon) &= \frac{1}{\epsilon^2} - \frac{\pi^2}{3} - \frac{1}{\mu_{\tilde{q}}^2 \epsilon} \left( \frac{1}{\epsilon^2} + \frac{1}{\epsilon} + \frac{\pi^2}{6} + 2 \right) - \frac{\log(1 + \mu_{\tilde{q}}^2)}{\epsilon} + \frac{2}{\epsilon} + 4 - \frac{\pi^2}{6} \\ J_{g\tilde{q}}^{a;NS}(\mu_{\tilde{q}}) &= \frac{\pi^2}{3} - 2\text{Li}_2 \left( \frac{1}{1 + \mu_{\tilde{q}}^2} \right) - 2\text{Li}_2(-\mu_{\tilde{q}}^2) - \frac{1}{2} \log^2(1 + \mu_{\tilde{q}}^2). \end{aligned} \quad (\text{A.21})$$

In analogy to the final-final case of Eqs.(A.11) and (A.12) we introduce a phase-space cutoff

$$\begin{aligned} D_{g\tilde{q}}^a &\rightarrow D_{g\tilde{q}}^a \Theta(\alpha - 1 + x_{g\tilde{q},a}) \\ \Delta I_{g\tilde{q}}^a(\alpha) &= -C_F \frac{\Theta(1 - \alpha - x)}{1 - x} \left[ -2 + 2 \log \left( 1 + \frac{1}{1 + \mu_{\tilde{q}}^2 - x} \right) \right], \end{aligned} \quad (\text{A.22})$$

where the kinematic variable  $x_{ij,a}$  is given by

$$x_{ij,a} = \frac{p_a p_i + p_a p_j - p_i p_j + \frac{m_{ij}^2 - m_i^2 - m_j^2}{2}}{p_a p_i + p_a p_j}. \quad (\text{A.23})$$

# Appendix B

## Renormalization

In MADGOLEM the ultraviolet counter terms are included automatically via the leading order topologies generated from QGRAF [26]. The counter terms required for the renormalization of the massive colored particles and the strong coupling constant, as well as the wave function renormalization of the colored fields, are all expressed in terms of one-loop two-point functions, which encode the corresponding  $\mathcal{O}(\alpha_s)$  quantum effects, and that are implemented in MADGOLEM in separate libraries. The current MADGOLEM implementation fully supports renormalized QCD effects for the Standard Model, the MSSM, and several extensions of the SM featuring new strongly interacting degrees of freedom, *e.g.* scalar color-octets (sgluons). In this appendix we give all relevant expressions for the renormalization of sgluons (which is relevant for the calculations presented in chapter 3) and supersymmetric QCD sector of the MSSM (which is relevant for chapters 4 and 5).

### B.1 Sgluons

We employ the standard 't Hooft-Veltman scheme for dimensional regularization with  $d = 4 - 2\varepsilon$  dimensions. The renormalization constants we define through the additive or multiplicative relations between the bare and the renormalized quantities

$$\Psi^{(0)} \rightarrow Z_\Psi^{1/2} \Psi \quad m_\Psi^{(0)} \rightarrow m_\Psi + \delta m_\Psi \quad g_s^{(0)} \rightarrow g_s + \delta g_s. \quad (\text{B.1})$$

The field with  $\Psi = q, A, G$  denotes all the strongly interacting fields of the sgluon model. Which corresponds to the SM minimally extended to accommodate a scalar color-adjoint with no electroweak charges (cf. Chap. 3 for more details). Given a generic Lagrangian  $\mathcal{L}(\Psi, m_\Psi, g_s)$  with a QCD interaction this procedure consistently gives a counter term Lagrangian of the form  $\delta\mathcal{L}(\Psi, m_\Psi, g_s, \delta\Psi, \delta m_\Psi, \delta g_s)$ .

We notice, first of all that the new sgluon field modifies the strong coupling beta function. If we start by decoupling the quantum corrections to the quark-quark-gluon vertex in terms of the strong coupling constant  $Z_{g_s}$ , the gluon field renormalization  $Z_3$ , and the quark field renormalization  $Z_2$  this translates into a combined expression  $Z_1 = Z_{g_s} Z_2 Z_3^{1/2}$ , which renormalizes the quark-gluon interaction. Each of these renormalization constants we expand as

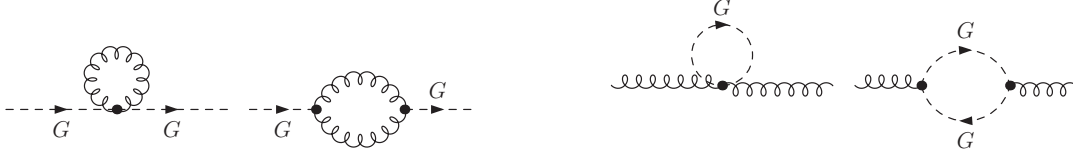


Figure B.1: Feynman diagrams for the sgluon field renormalization (left) and sgluon-mediated gluon field renormalization (right).

$Z_i = 1 + \delta_i + \mathcal{O}(\alpha_s^2)$ , with  $\overline{\text{MS}}$  counter terms  $\delta_i$ . The strong coupling constant renormalization at one loop we can thus write as

$$\begin{aligned} \delta g_s &= \delta_1 - \delta_2 - \frac{1}{2}\delta_3 \\ \text{with } \delta_1 &= \delta_1^{\text{SM}} = -\frac{\alpha_s}{4\pi} (C_A + C_F) \Delta_\epsilon \\ \delta_2 &= \delta_2^{\text{SM}} = -\frac{\alpha_s}{4\pi} C_F \Delta_\epsilon \\ \delta_3 &= \delta_3^{\text{SM}} + \delta_3^G = \frac{\alpha_s}{4\pi} \left( \frac{5}{3} C_A - n_f C_F T_R \right) - \frac{\alpha_s}{12\pi} C_A \Delta_\epsilon, \end{aligned} \quad (\text{B.2})$$

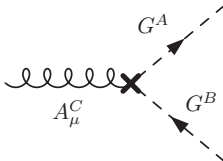
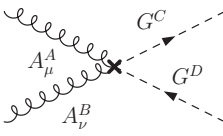
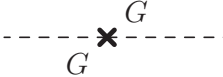
where the last term in Eq. B.2 corresponds to the genuine sgluon contribution to the gluon self-energies (cf. left diagrams in Fig. B.1). The shifted pole in the  $\overline{\text{MS}}$  prescription is  $\Delta_\epsilon \equiv (4\pi)^\epsilon / \Gamma(1 - \epsilon) = 1/\epsilon - \gamma_E + \log(4\pi) + \mathcal{O}(\epsilon)$  and the total number of fermions is  $n_f = 6$ . The  $SU(3)_C$  color factors are  $C_F = 4/3$ ,  $C_A = 3$  and  $T_R = 1/2$ . Because there are no direct couplings between sgluons and matter fields  $\delta_2$  keeps its SM value. For the same reason, sgluon-mediated corrections to the quark-quark-gluon vertex are absent at one loop, so  $\delta_1$  does not change either. Only the gluon self energy is modified by the triple and quartic gluon/sgluon interactions, as displayed in Fig. B.1.

Combining all of the above contributions and decoupling the heavy ( $H$ ) colored degrees of freedom — in our case the top and the sgluon — gives us the final expression for  $\delta g_s$  in terms of the measured  $\alpha_s$  values. We implement the subtraction of the heavy modes in the zero-momentum scheme [17, 58]. It leaves the renormalization group running of  $\alpha_s$  merely determined by the light ( $L$ ) degrees of freedom, which corresponds to the gluon and the  $n_f - 1 = 5$  active quarks. The renormalization constant finally reads

$$\begin{aligned} \delta g_s &= -\frac{\alpha_s}{4\pi} \frac{\beta_0^L + \beta_0^H}{2} \Delta_\epsilon - \frac{\alpha_s}{4\pi} \left( \frac{1}{3} \log \frac{m_t^2}{\mu_R^2} + \frac{1}{2} \log \frac{m_G^2}{\mu_R^2} \right) \\ \beta_0 &= \beta_0^L + \beta_0^H = \left( \frac{11}{3} C_A - (n_f - 1) C_F T_R \right) - \left( C_F T_R + \frac{1}{3} C_A \right). \end{aligned} \quad (\text{B.3})$$

In a second step we need to compute the QCD renormalization constants in the sgluon sector. The sgluon two-point function receives  $\mathcal{O}(\alpha_s)$  corrections due to virtual gluon interchange, as shown in Fig. B.1. The corresponding ultraviolet divergences we absorb into the sgluon mass  $m_G$  and field-strength  $Z_G$ . As renormalization condition we choose the on-shell

---

	$-i g_s f^{ABC} \left[ \delta g_s + \frac{1}{2} (\delta Z_G + \delta Z_{G^*} + \delta Z_A) \right] [G^{*A} (\partial^\mu G^B) - (\partial^\mu G^{*A}) G^B] A_\mu^C$
	$i g_s^2 (f^{ACE} f^{BDE} + f^{ADE} f^{BCE}) [2 \delta g_s + \delta Z_A + \delta Z_G] G^{*C} G^D A_\mu^A A^{B\mu}$
	$p^2 \delta Z_G - \delta m_G^2 - m_G^2 \delta Z_G$

---

Table B.1: Counter term Feynman rules for the sgluon-mediated interactions.

scheme

$$\begin{aligned}
\Re \hat{\Sigma}'(m_G^2) = 0 &\quad \Rightarrow \quad \delta Z_G = - \Re \Sigma'(m_G^2) \\
\Re \hat{\Sigma}(m_G^2) = 0 &\quad \Rightarrow \quad \delta m_G = + \Re \Sigma(m_G^2),
\end{aligned} \tag{B.4}$$

where  $\Re \hat{\Sigma}_G$  denotes the (real part of the) renormalized sgluon self-energy,

$$\hat{\Sigma}_G(q^2) = \Sigma_G(q^2) + (q^2 - m_G^2) \delta Z_G - \delta m_G^2, \tag{B.5}$$

and  $\hat{\Sigma}'(q^2) \equiv d^2/dq^2 \hat{\Sigma}(q^2)$  the corresponding derivative with respect to the momentum squared. The analytic form of all renormalization constants we reduce down to one and two-point scalar loop integrals [59]. The sgluon mass and field strength renormalization then reads

$$\begin{aligned}
\delta Z_G &= \frac{\alpha_s}{2\pi} C_A [B_0(m_G^2, m_G^2, 0) + m_G^2 B'_0(m_G^2, m_G^2, 0)] \\
\delta m_G &= -\frac{\alpha_s}{\pi} C_A \left[ m_G^2 + \frac{3}{4} A_0(m_G^2) \right].
\end{aligned} \tag{B.6}$$

As expected, these expressions are identical to the squark case, modulo a factor  $C_A/C_F$  that reflects the different  $SU(3)_C$  representations.

Finally, in Table B.2 we quote the analytical expressions for the relevant ultraviolet counter terms  $\delta \mathcal{L}$  as a function of the field, mass, and strong coupling renormalization constants derived in this Appendix.

## B.2 Supersymmetric QCD

The renormalization constants we define through the relation between the bare and the renormalized fields, masses and the coupling constant in Eq. B.1, where now the field  $\Psi =$

$q, \tilde{q}, g, \tilde{g}$  denotes all strongly interacting MSSM fields. We express the corresponding SUSY-QCD counter terms to vertices and propagators in Table B.2.

The actual counter terms, presented below, we include in a separate library. The strong coupling constant we renormalize in the  $\overline{\text{MS}}$  scheme and explicitly decouple all particles heavier than the bottom quark. In the very same way as for the sgluon case, this zero-momentum subtraction scheme [17, 58] leaves us with the renormalization group running of  $\alpha_s$  from light colored particles only. It corresponds to the measured value of the strong coupling, for example in a combined fit with the parton densities. Its renormalization constant reads

$$\delta g_s = -\frac{\alpha_s}{4\pi} \frac{\beta_0^L + \beta_0^H}{2} \Delta_\epsilon - \frac{\alpha_s}{4\pi} \left( \frac{1}{3} \log \frac{m_t^2}{\mu_R^2} + \log \frac{m_{\tilde{g}}^2}{\mu_R^2} + \frac{1}{12} \sum_{\text{squarks}} \log \frac{m_{\tilde{q}_j}^2}{\mu_R^2} \right). \quad (\text{B.7})$$

The UV divergence appears as  $\Delta_\epsilon = 1/\epsilon - \gamma_E + \log(4\pi) + \mathcal{O}(\epsilon)$ . Both light ( $L$ ) and heavy ( $H$ ) colored particles contribute to the beta function

$$\beta_0 = \beta_0^L + \beta_0^H = \left[ \frac{11}{3} C_A - \frac{2}{3} n_f \right] + \left[ -\frac{2}{3} - \frac{2}{3} C_A - \frac{1}{3} (n_f + 1) \right]. \quad (\text{B.8})$$

MADGOLEM sets the number of active flavors to  $n_f = 5$ .

The analytic form of all renormalization constants we reduce down to one-point and two-point scalar one-loop functions, which we handle by means of standard 't Hooft-Veltman dimensional regularization scheme in  $4 - 2\epsilon$  dimensions. The field and mass renormalization constants we compute from the one-loop self-energies which involve virtual gluons and gluinos. All fields are renormalized on-shell. In addition, for the gluon field we subtract the heavy modes consistently with our  $g_s$  renormalization scheme. The underlying Slavnov-Taylor identities link the corresponding finite parts of the counter terms as  $\delta Z_G = -2 \delta g_s$ .

In addition, we need to pay attention to dimensional regularization breaks supersymmetry through a mismatch of two gaugino and the  $2 - 2\epsilon$  gauge vector degrees of freedom [51]. As a result, the Yukawa coupling  $\hat{g}_s$  appearing for example in the  $q\tilde{q}\tilde{g}$  vertex departs from  $g_s$ . We restore supersymmetry by hand, forcing  $\hat{g}_s = g_s$ . The corresponding finite counter term can be computed using dimensional reduction,

$$\frac{\hat{g}_s}{g_s} = \frac{\alpha_s}{4\pi} \left( \frac{2}{3} n_f - \frac{3}{2} C_F \right) \quad \Rightarrow \quad \delta_{\text{SUSY}} = \frac{4}{3} \frac{\alpha_s}{4\pi}. \quad (\text{B.9})$$

Finally, we quote the analytical expressions for the field and mass renormalization. For the scalar one-point and two-point functions we adopt the notation of Ref. [59]. The corrections to the massless quarks including the non-chiral SUSY contributions are

$$\delta Z_{q_{L/R}} = -\frac{\alpha_s}{4\pi} C_F \left[ B_0(0, 0, 0) + B_0(0, m_{\tilde{g}}^2, m_{\tilde{q}_{L/R}}^2) + (m_{\tilde{g}}^2 - m_{\tilde{q}_{L/R}}^2) B'_0(0, m_{\tilde{g}}^2, m_{\tilde{q}_{L/R}}^2) + (m_{\tilde{g}}^2 - m_{\tilde{q}_{R/L}}^2) B'_0(0, m_{\tilde{g}}^2, m_{\tilde{q}_{R/L}}^2) \right]. \quad (\text{B.10})$$

The corresponding squark fields and mass are renormalized as

$$\begin{aligned}\delta Z_{\tilde{q}_s \tilde{q}_s} &= \frac{\alpha_s}{2\pi} C_F \left[ B_0(m_{\tilde{q}_s}^2, 0, m_{\tilde{q}_s}^2) + m_{\tilde{q}_s}^2 B'_0(m_{\tilde{q}_s}^2, 0, m_{\tilde{q}_s}^2) - B_0(m_{\tilde{q}_s}^2, m_g^2, 0) + (m_g^2 - m_{\tilde{q}_s}^2) B'_0(m_{\tilde{q}_s}^2, m_g^2, 0) \right] \\ \delta m_{\tilde{q}_s} &= -\frac{\alpha_s}{4\pi} C_F \left[ 4m_{\tilde{q}_s}^2 + 3A_0(m_{\tilde{q}_s}^2) + 2A_0(m_g^2) + 2(m_g^2 - m_{\tilde{q}_s}^2) B_0(m_{\tilde{q}_s}^2, m_g^2, 0) \right].\end{aligned}\quad (\text{B.11})$$

The gluon wave function renormalization<sup>1</sup>, linked to the counter term for the strong coupling, is

$$\delta Z_G = \frac{\alpha_s}{4\pi} (\beta_0^L + \beta_0^H) \frac{1}{\epsilon} + \frac{\alpha_s}{2\pi} \left[ \log \frac{m_g^2}{\mu^2} + \frac{1}{12} \sum_{\text{squarks}} \log \frac{m_q^2}{\mu^2} + \frac{1}{3} \log \frac{m_t^2}{\mu^2} \right].\quad (\text{B.12})$$

Finally, the gluino field and mass renormalization constants are

$$\begin{aligned}\delta Z_{\tilde{g}} &= \frac{\alpha_s}{4\pi} C_A \left[ 1 + 4m_g^2 B'_0(m_g^2, 0, m_g^2) - \frac{A_0(m_g^2)}{m_g^2} \right] \\ &+ \frac{\alpha_s}{8\pi m_g^2} \sum_{\text{light (s)quarks}} \left[ A_0(m_q^2) - (m_g^2 + m_q^2) B_0(m_g^2, 0, m_q^2) - 2m_g^2 (m_g^2 - m_q^2) B'_0(m_g^2, 0, m_q^2) \right] \\ &+ \frac{\alpha_s}{8\pi m_g^2} \sum_{\text{heavy (s)quarks}} \left[ 2m_g^2 (m_q^2 - m_q^2 - m_g^2) B'_0(m_g^2, m_q^2, m_{\tilde{q}_s}^2) + (m_q^2 - m_q^2 - m_g^2) B_0(m_g^2, m_q^2, m_{\tilde{q}_s}^2) \right. \\ &\quad \left. + A_0(m_{\tilde{q}_s}^2) - A_0(m_q^2) \right] \\ &+ \frac{\alpha_s}{\pi} \sum_{\text{heavy (s)quarks}} m_{\tilde{g}} m_q R_{s1}^q R_{s2}^q B'_0(m_g^2, m_q^2, m_{\tilde{q}_s}^2) \\ \delta m_{\tilde{g}} &= -\frac{\alpha_s}{4\pi} C_A m_{\tilde{g}} \left[ 1 + 3\frac{A_0(m_g^2)}{m_g^2} \right] + \frac{\alpha_s}{8\pi m_{\tilde{g}}} \sum_{\text{light (s)quarks}} \left[ A_0(m_q^2) + (m_g^2 - m_q^2) B_0(m_g^2, 0, m_q^2) \right] \\ &+ \frac{\alpha_s}{8\pi m_{\tilde{g}}} \sum_{\text{heavy (s)quarks}} \left[ A_0(m_q^2) - A_0(m_q^2) - (m_q^2 - m_q^2 - m_g^2) B_0(m_g^2, m_q^2, m_{\tilde{q}_s}^2) \right] \\ &- \frac{\alpha_s}{2\pi} \sum_{\text{heavy (s)quarks}} m_q R_{s1}^q R_{s2}^q B_0(m_g^2, m_q^2, m_{\tilde{q}_s}^2).\end{aligned}\quad (\text{B.13})$$

The sum over heavy squarks covers all squark flavors corresponding to heavy quarks. We usually consider the bottom quark massless, which means that only the two stop eigenstates feel top mass effects. However, the bottom/sbottom loops can be trivially moved from the light to the heavy category. The stop mass eigenstates  $\tilde{t}_{1,2}$  are related to the electroweak interaction bases through a rotation with  $\det \mathcal{R} = \pm 1$ .

---

<sup>1</sup>We remark that  $G$  in this appendix stands for the gluon field, not to be confused with the notation employed for the sgluons.

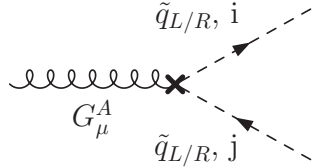
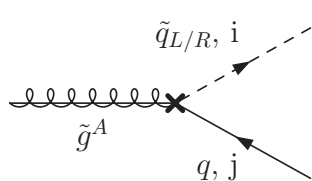
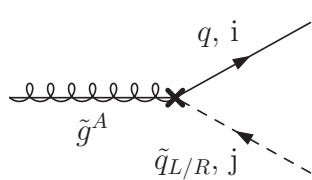
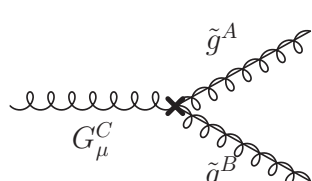
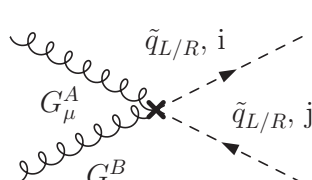
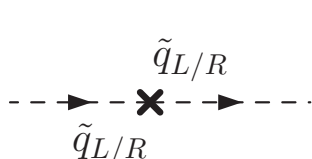
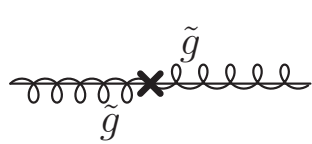
	$-i g_s T_{ij}^A \left[ \delta g_s + \frac{\delta Z_{\tilde{q}_{L/R,i}} + \delta Z_{\tilde{q}_{L/R,j}} + \delta Z_G}{2} \right] \tilde{q}_{L/R,i} (p_i + p_j)^\mu G_\mu^A \tilde{q}_{L/R,j}$
	$\mp i g_s \sqrt{2} T_{ij}^A \tilde{g}^A \left[ \delta g_s + \frac{\delta Z_{\tilde{q}_{L/R,i}} + \delta Z_{q_j} + \delta Z_{\tilde{g}}}{2} + \delta_{\text{SUSY}} \right] P_{L/R} q_j \tilde{q}_{L/R,i}$
	$\pm i g_s \sqrt{2} T_{ij}^A \tilde{q}_i \left[ \delta g_s + \frac{\delta Z_{\tilde{q}_{R/L,j}} + \delta Z_{q_i}^\dagger + \delta Z_{\tilde{g}}}{2} + \delta_{\text{SUSY}} \right] P_{L/R} \tilde{g}^A q_i \tilde{q}_{R/L,j}$
	$-g_s \left[ \delta g_s + \delta Z_{\tilde{g}} + \frac{\delta Z_G}{2} \right] \tilde{g}^A \gamma^\mu \tilde{g}^B G_\mu^C f^{ABC}$
	$i g_s \left[ \delta g_s + \delta Z_G + \frac{\delta Z_{\tilde{q}_{L/R,i}} + \delta Z_{\tilde{q}_{L/R,j}}}{2} \right] \{T^A T^B\}_{ij} \tilde{q}_{L/R,i} \tilde{q}_{L/R,j} G_\mu^A G^{B\mu}$
	$p^2 \delta Z_{\tilde{q}_{L/R}} - \delta m_{\tilde{q}_{L/R}}^2 - \delta Z_{\tilde{q}_{L/R}} m_{\tilde{q}_{L/R}}^2$
	$\not{p} \delta Z_{\tilde{g}} - m_{\tilde{g}} \delta Z_{\tilde{g}} - \delta m_{\tilde{g}}$

Table B.2: Strong interaction counter terms for the MSSM. The finite supersymmetry-restoring counter term  $\delta_{\text{SUSY}}$  is given in Eq.(B.9).

# Bibliography

- [1] R. K. Ellis, W. J. Stirling and B. R. Webber, QCD and Collider Physics, Cambridge University Press, Cambridge, 1996.
- [2] D. J. Gross and F. Wilczek, Ultraviolet behaviour of non-Abelian gauge theories, Phys. Rev. Lett. 30 (1973) 1343.
- [3] H. D. Politzer, reliable perturbative results for strong interactions?, Phys. Rev. Lett. 30 (1973) 1346.
- [4] J. C. Collins, D. E. Soper and G. F. Sterman, Adv. Ser. Direct. High Energy Phys. **5**, 1 (1988) [hep-ph/0409313].
- [5] L.N. Lipatov, Sov. J. Nucl. Phys. 20 (1975) 95; V.N. Gribov and L.N. Lipatov, Sov. J. Nucl. Phys. 15 (1972) 438; G. Altarelli and G. Parisi, Nucl. Phys. B126 (1977) 298; Yu.L. Dokshitzer, Sov. Phys. JETP 46 (1977) 641.
- [6] J. Alwall *et al.*, JHEP **0709**, 028 (2007).
- [7] T. Hahn, Comput. Phys. Commun. **140**, 418 (2001); T. Hahn and C. Schappacher, Comput. Phys. Commun. **143**, 54 (2002); T. Hahn and M. Pérez-Victoria, Comput. Phys. Commun. **118**, 153 (1999).
- [8] A. Pukhov, et al., CompHEP: A package for evaluation of Feynman diagrams and integration over multi-particle phase space. Use's manual for version 33.
- [9] T. Gleisberg, et al., SHERPA 1.alpha, a proof-of-concept version, JHEP 02 (2004) 056.
- [10] F. Bloch and A. Nordsieck, Phys. Rev. 52, 54 (1937).
- [11] T. Kinoshita, J. Math. Phys. 3, 650 (1962).
- [12] T. D. Lee and M. Nauenberg, Phys. Rev. 133, B1549 (1964).
- [13] L. Phaf and S. Weinzierl, JHEP **0104**, 006 (2001) [hep-ph/0102207].

- [14] S. Catani and M. H. Seymour, Nucl. Phys. B **485**, 291 (1997) [Erratum-ibid. B **510**, 503 (1998)]; S. Catani, S. Dittmaier, M. H. Seymour and Z. Trocsanyi, Nucl. Phys. B **627**, 189 (2002).
- [15] A. S. Belyaev, E. E. Boos and L. V. Dudko, Phys. Rev. D **59**, 075001 (1999) [hep-ph/9806332].
- [16] see e.g. S. Frixione, E. Laenen, P. Motylinski *et al.*, JHEP **0807**, 029 (2008).
- [17] W. Beenakker, R. Höpker, M. Spira and P. M. Zerwas, Phys. Rev. Lett. **74**, 2905 (1995); W. Beenakker, M. Krämer, T. Plehn, M. Spira and P. M. Zerwas, Nucl. Phys. B **515**, 3 (1998); G. Bozzi, B. Fuks and M. Klasen, Phys. Rev. D **72**, 035016 (2005).
- [18] W. Beenakker, R. Hopker, M. Spira and P. M. Zerwas, Z. Phys. C **69**, 163 (1995) [hep-ph/9505416].
- [19] W. Beenakker, R. Höpker, M. Spira and P. M. Zerwas, Nucl. Phys. B **492** (1997) 51.
- [20] available under [www.thphys.uni-heidelberg.de/~plehn](http://www.thphys.uni-heidelberg.de/~plehn)
- [21] W. Beenakker, M. Kramer, T. Plehn, M. Spira and P. M. Zerwas, Nucl. Phys. B **515**, 3 (1998) [arXiv:hep-ph/9710451];
- [22] T. Plehn, C. Weydert, PoS **CHARGED2010**, 026 (2010) [arXiv:1012.3761 [hep-ph]].
- [23] W. Beenakker, R. Höpker, M. Spira and P. M. Zerwas, Phys. Rev. Lett. **74**, 2905 (1995);
- [24] W. Beenakker, M. Klasen, M. Krämer, T. Plehn, M. Spira and P. M. Zerwas, Phys. Rev. Lett. **83**, 3780 (1999) [Erratum-ibid. **100**, 029901 (2008)].
- [25] R. Frederix, T. Gehrmann and N. Greiner, JHEP **0809**, 122 (2008); and JHEP **1006**, 086 (2010).
- [26] P. Nogueira, J. Comp. Phys. **105**, 279 (1993).
- [27] T. Binoth, J. P. Guillet, G. Heinrich, E. Pilon and C. Schubert, JHEP **0510** (2005) 015 [hep-ph/0504267]. G. Cullen, N. Greiner, A. Guffanti, J. -P. Guillet, G. Heinrich, S. Karg, N. Kauer, T. Kleinschmidt *et al.*, Nucl. Phys. Proc. Suppl. **205-206** (2010) 67-73; G. Cullen, N. Greiner, G. Heinrich, G. Luisoni, P. Mastrolia, G. Ossola, T. Reiter and F. Tramontano, arXiv:1111.2034 [hep-ph].
- [28] T. Binoth, J. P. Guillet, G. Heinrich, E. Pilon and T. Reiter, Comput. Phys. Commun. **180**, 2317 (2009); G. Cullen, J. P. Guillet, G. Heinrich, T. Kleinschmidt, E. Pilon, T. Reiter and M. Rodgers, arXiv:1101.5595 [hep-ph].
- [29] L. J. Dixon, In *Boulder 1995, QCD and beyond* 539-582 [arXiv:9601359 [hep-ph]].
- [30] C. F. Berger, Z. Bern, L. J. Dixon, F. Febres Cordero, D. Forde, H. Ita, D. A. Kosower and D. Maitre, Phys. Rev. D **78** (2008) 036003 [arXiv:0803.4180 [hep-ph]].

- [31] V. Hirschi, R. Frederix, S. Frixione, M. V. Garzelli, F. Maltoni and R. Pittau, *JHEP* **1105**, 044 (2011) [arXiv:1103.0621 [hep-ph]].
- [32] A. van Hameren, *Comput. Phys. Commun.* **182**, 2427 (2011) [arXiv:1007.4716 [hep-ph]].
- [33] W. Beenakker, R. Hopker and P. M. Zerwas, *Phys. Lett. B* **349**, 463 (1995) [hep-ph/9501292].
- [34] T. Plehn and T. M. P. Tait, *J. Phys. G* **36**, 075001 (2009).
- [35] S. Y. Choi, M. Drees, A. Freitas, and P. M. Zerwas, *Phys. Rev. D* **78**, 095007 (2008); S. Y. Choi, M. Drees, J. Kalinowski, J. M. Kim, E. Popenda, and P. M. Zerwas, *Phys. Lett. B* **672**, 246 (2009); S. Y. Choi, D. Choudhury, A. Freitas, J. Kalinowski, J. M. Kim, and P. M. Zerwas, *JHEP* **1008**, 025 (2010).
- [36] T. Binoth, D. Goncalves Netto, D. Lopez-Val, K. Mawatari, T. Plehn and I. Wigmore, *Phys. Rev. D* **84**, 075005 (2011) [arXiv:1108.1250 [hep-ph]].
- [37] D. Goncalves-Netto, D. Lopez-Val, K. Mawatari, T. Plehn and I. Wigmore, *Phys. Rev. D* **85**, 114024 (2012) [arXiv:1203.6358 [hep-ph]].
- [38] D. Goncalves-Netto, D. Lopez-Val, K. Mawatari, T. Plehn and I. Wigmore, arXiv:1211.0286 [hep-ph].
- [39] ATLAS Collaboration, [hep-ex/1210.4826]. Submitted to EPJC-Letters.
- [40] J. Pumplin, D. R. Stump, J. Huston, H. L. Lai, P. Nadolsky and W. K. Tung, *JHEP* **0207**, 012 (2002).
- [41] Prospino collaboration, private communication.
- [42] S. Frixione, Z. Kunszt and A. Signer, *Nucl. Phys. B* **467**, 399 (1996). Z. Nagy and Z. Trocsanyi, *Phys. Rev. D* **59**, 014020 (1999) [Erratum-ibid. *D* **62**, 099902 (2000)].
- [43] M. L. Mangano, M. Moretti and R. Pittau, *Nucl. Phys. B* **632** (2002) 343.
- [44] S. Catani, F. Krauss, R. Kuhn *et al.*, *JHEP* **0111** (2001) 063.
- [45] J. Alwall, S. de Visscher, F. Maltoni, *JHEP* **0902** (2009) 017.
- [46] T. Sjöstrand, S. Mrenna and P. Z. Skands, *JHEP* **0605**, 026 (2006).
- [47] E. L. Berger, M. Klasen, T. M. P. Tait, *Phys. Rev. D* **62**, 095014 (2000) [Erratum-ibid. *D* **67**, 099901 (2003)]; M. Spira, arXiv:hep-ph/0211145; T. Plehn, [arXiv:hep-ph/0410063].
- [48] B. C. Allanach, S. Grab and H. E. Haber, *JHEP* **1101**, 138 (2011) [arXiv:1010.4261 [hep-ph]].

- [49] G. Aad et al. [ATLAS Collaboration], Search for squarks and gluinos using final states with jets and missing transverse momentum with the ATLAS detector in  $\sqrt{S}$  TeV proton-proton collisions, arXiv:1109.6572 [hep-ex]; Chatrchyan et al. [CMS Collaboration], Search for Supersymmetry at the LHC in Events with Jets and Missing Transverse Energy, arXiv:1109.2352 [hep-ex].
- [50] B. C. Allanach *et al.*, in *Proc. of the APS/DPF/DPB Summer Study on the Future of Particle Physics (Snowmass 2001)* ed. N. Graf, Eur. Phys. J. C **25**, 113 (2002).
- [51] S. P. Martin and M. T. Vaughn, Phys. Lett. B **318**, 331 (1993).
- [52] S. S. AbdusSalam, B. C. Allanach, H. K. Dreiner, J. Ellis, U. Ellwanger, J. Gunion, S. Heinemeyer and M. Krämer *et al.*, Eur. Phys. J. C **71**, 1835 (2011) [arXiv:1109.3859 [hep-ph]].
- [53] A. Sommerfeld, Ann. der Phys. **403**, 257 (1931).
- [54] W. Beenakker, S. Brensing, M. Kramer, A. Kulesza, E. Laenen and I. Niessen, JHEP **0912**, 041 (2009) [arXiv:0909.4418 [hep-ph]]. J. Debove, B. Fuks and M. Klasen, Nucl. Phys. B **849**, 64 (2011) [arXiv:1102.4422 [hep-ph]]; J. Debove, B. Fuks and M. Klasen, Nucl. Phys. B **842**, 51 (2011); A. Kulesza and L. Motyka, Phys. Rev. D **80**, 095004 (2009) [arXiv:0905.4749 [hep-ph]]; A. Kulesza and L. Motyka, Phys. Rev. Lett. **102**, 111802 (2009) [arXiv:0807.2405 [hep-ph]]; M. Beneke, P. Falgari and C. Schwinn, Nucl. Phys. B **842**, 414 (2011) [arXiv:1007.5414 [hep-ph]]; M. R. Kauth, J. H. Kuhn, P. Marquard and M. Steinhauser, arXiv:1108.0361 [hep-ph]; M. R. Kauth, A. Kress and J. H. Kuhn, arXiv:1108.0542 [hep-ph].
- [55] T. Plehn, M. Spannowsky, M. Takeuchi and D. Zerwas, JHEP **1010**, 078 (2010) [arXiv:1006.2833 [hep-ph]]; T. Plehn, M. Spannowsky and M. Takeuchi, arXiv:1111.5034 [hep-ph]; F. Kling, T. Plehn and M. Takeuchi, arXiv:1207.4787 [hep-ph].
- [56] for a pedagogical introduction see *e.g.* T. Plehn, [arXiv:0910.4182 [hep-ph]].
- [57] G. Bevilacqua, M. Czakon, C. G. Papadopoulos, R. Pittau, and M. Worek, JHEP **0909**, 109 (2009)
- [58] J. C. Collins, F. Wilczek and A. Zee, Phys. Rev. D **18**, 242 (1978).
- [59] A. van Hameren, Comput. Phys. Commun. **182**, 2427 (2011) [arXiv:1007.4716 [hep-ph]].